Transport and thermodynamic studies of the superconductors $A_3T_4Sn_{13}$ and YFe_2Ge_2

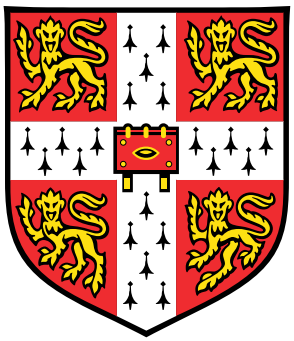

Xiaoye Chen

Department of Physics

University of Cambridge

This dissertation is submitted for the degree of

Doctor of Philosophy

Corpus Christi College

October 2017

Transport and thermodynamic studies of the superconductors $A_3T_4\mathbf{Sn}_{13}$ and $\mathbf{YFe_2Ge_2}$

Xiaoye Chen

Materials in proximity to quantum critical points (QCPs) experience strong fluctuations in the order parameter associated with the transition and often, as a result, display interesting properties. In this dissertation, we have used a variety of experimental probes such as Shubnikov-de Haas quantum oscillations, thermal conductivity and heat capacity, to better understand two such materials — $A_3T_4Sn_{13}$ and YFe_2Ge_2.

$A_3T_4Sn_{13}$ (A = Ca, Sr; T = Ir, Rh) is a family of quasi-skutterudite superconductors with moderate T_c's between 4 and 8 K. Although the superconductivity is believed to be phonon-mediated with s-wave pairing symmetry, an unusual second-order structural transition makes this material family fascinating to study. Whether this structural transition is a result of three distortions with perpendicular wavevectors resulting in a cubic-to-cubic transformation, or each wavevector acting independently giving rise to cubic-to-tetragonal transformations and formation of twinned domains is a disputed issue. We have measured quantum oscillations in the resistivity of $Sr_3Ir_4Sn_{13}$ and compared it to density functional theory (DFT) calculations for both scenarios. Our results strongly suggest that the former interpretation is correct.

The structural transition temperature T^* in $A_3T_4Sn_{13}$ can be suppressed to zero by tuning with physical or chemical pressure. In $(Ca_xSr_{1-x})_3Rh_4Sn_{13}$, the quantum critical point can be accessed purely by chemical substitution at $x \sim 0.9$. In the vicinity of the QCP, we expect large fluctuations of the order parameter at low temperatures, which for a structural transition could manifest as a structural disorder. We have measured thermal conductivity at temperatures much lower than T_c and found that it is well described by a single power law with suppressed exponents near the QCP. The heat capacity, however, remains $\sim T^3$. After excluding conventional phonon scattering mechanisms, we propose the possibility of intrinsic quasi-static spatial disorder that is related to the structural QCP.

YFe_2Ge_2 is closely linked to the "122" family of iron-based superconductors like KFe_2As_2, although it has a significantly lower $T_c \sim 1$ K. It has a rather three-dimensional Fermi surface which closely resembles that of KFe_2As_2 in the pressure-induced collapsed tetragonal

phase. YFe_2Ge_2 is in proximity to several types of magnetic order which are predicted by DFT calculations to have lower energy than the non-spin polarised case. Even though YFe_2Ge_2 is non-magnetic, its superconductivity could be strongly affected by magnetic fluctuations. Through a collaboration with researchers at the University of Waterloo, we have measured the thermal conductivity of YFe_2Ge_2 down to millikelvin temperatures and up to 2.5 T in field. Our results suggest that YFe_2Ge_2 is a nodal superconductor. This result could assist in the explanation of the unconventional superconductivity in iron-based superconductors.

Declaration

This dissertation is the result of my own work and includes nothing which is the outcome of work done in collaboration except as declared in the Acknowledgements and specified in the text. It is not substantially the same as any that I have submitted, or, is being concurrently submitted for a degree or diploma or other qualification at the University of Cambridge or any other University or similar institution except as specified in the text. It contains less than 60,000 words including abstract, tables, footnotes and appendices.

Xiaoye Chen
October 2017

Acknowledgements

I am grateful for the support from my supervisor, Dr Michael Sutherland, who has been extremely patient with me and provided invaluable direction throughout my PhD. From identification of an interesting research topic to data analysis and theoretical interpretation of the results, he is always there whenever I seek his guidance and counsel.

I am fortunate to have worked closely with Dr Jordan Baglo and Hong'En Tan in the lab and I have learnt many practical experimental skills from them. I am also thankful to Dr Malte Grosche for the weekly group meetings that provided a reassuring periodic structure to my academic life, which would otherwise be rather amorphous.

The samples for the work on $A_3T_4\mathrm{Sn}_{13}$ presented in Chapters 3 and 4 are provided by Prof. Swee Kuan Goh and Prof. Kazuyoshi Yoshimura and their team of researchers from the Chinese University of Hong Kong and Kyoto University respectively. The theoretical model that is used to interpret our data (Section 4.4.3) was developed with guidance from Prof. Gilbert Lonzarich, who tirelessly explained to me the relevant concepts in detail.

The work related to the thermal conductivity measurement of $\mathrm{YFe_2Ge_2}$ was done in collaboration with Dr Rob Hill, William Toews and Jennifer Reid from the University of Waterloo and I have really enjoyed working with them. The crystal growth and heat capacity measurements of $\mathrm{YFe_2Ge_2}$ were performed by Jiasheng Chen, and Ben Seddon helped out by making contacts to some of the samples.

I appreciate all the assistance I have received from many members of the Quantum Matter group, including Jiasheng Chen, Corentin Morice, Hui Chang Chang, Keiron Murphy, Philip Brown, Konstantin Semeniuk, Prof. John Cooper, Pascal Reiß, Matthew Coak, Dr Patricia Alireza, Dr Leszek Spalek, Cheng Liu, Dr Siân Dutton, Dr Suchitra Sebastian and Yu-Te Hsu.

This work would not have been possible without the love and encouragement from my wife Joyce Chen, and the unwavering support of my parents and my brother.

The funding for my PhD has been provided by the Agency for Science, Technology and Research (A*STAR).

Contents

Chapter 1

Introduction

1.1 Quantum criticality

The study of critical phenomena has been a central theme in condensed matter physics for the past few decades. A classical, second-order transition occurs at a finite temperature and is driven by thermal fluctuations. Suppressing the continuous phase transition to zero temperature with a tuning parameter creates a quantum critical point (QCP), assuming that the transition remains second order and no other order intervenes. The tuning parameter could be magnetic field (e.g. $YbRh_2Si_2$ [1]), pressure (e.g. $CePd_2Si_2$ and $CeIn_3$ [2]) or chemical substitution (e.g. $BaFe_2(As_{1-x}P_x)_2$ [3]). This is illustrated in Figure 1.1(a). Even at zero temperature, one can induce a quantum phase transition driven purely by quantum fluctuations by adjusting the tuning parameter.

The interest in quantum criticality stems from the tendency of critical fluctuations, which are found in the vicinity of the critical point, to give rise to unexpected and exotic orders. A prominent example of such orders is unconventional superconductivity. In unconventional superconductors, pairing is not primarily or solely driven by vibrations of the lattice—critical fluctuations are believed to play an important role. Examples include heavy-fermion [4, 5], cuprate [6–8] and iron-based superconductors [9]. For these materials, the suppression of the continuous phase transition is interrupted by the formation of superconductivity. This is depicted in Figure 1.1(b). For heavy-fermion and iron-based superconductors, Order 1 represents antiferromagnetism and Order 2 represents superconductivity [2, 10]. The phase diagram for cuprates is much more complicated, with possibly multiple QCPs due to charge

and spin-density waves inside overlapping superconducting domes [8]. In the examples mentioned, long-range magnetic or density-wave order, which is detrimental to superconductivity, is broken up at the critical point. The fluctuations associated with those orders, however, are thought to act as pairing glue that enables unconventional superconductivity [2]. This conclusion is usually inferred from the coexistence and correlation between critical fluctuations and superconductivity. In the heavy-fermion superconductors $CePd_2Si_2$ and $CeIn_3$, non–Fermi-liquid electrical resistivities of $T^{1.2\pm0.1}$ and $T^{1.6\pm0.2}$ are observed where antiferromagnetic order has been suppressed and superconductivity has emerged. This is consistent with the scattering of quasiparticles via magnetic interactions in a quasi-two-dimensional ($CePd_2Si_2$) or three-dimensional ($CeIn_3$) material [2]. In the iron-based superconductor $Ba(Fe_{1-x}Co_x)_2As_2$, the enhancement of antiferromagnetic spin fluctuations, measured by nuclear magnetic resonance spectroscopy, coincides with the enhancement of superconductivity [11].

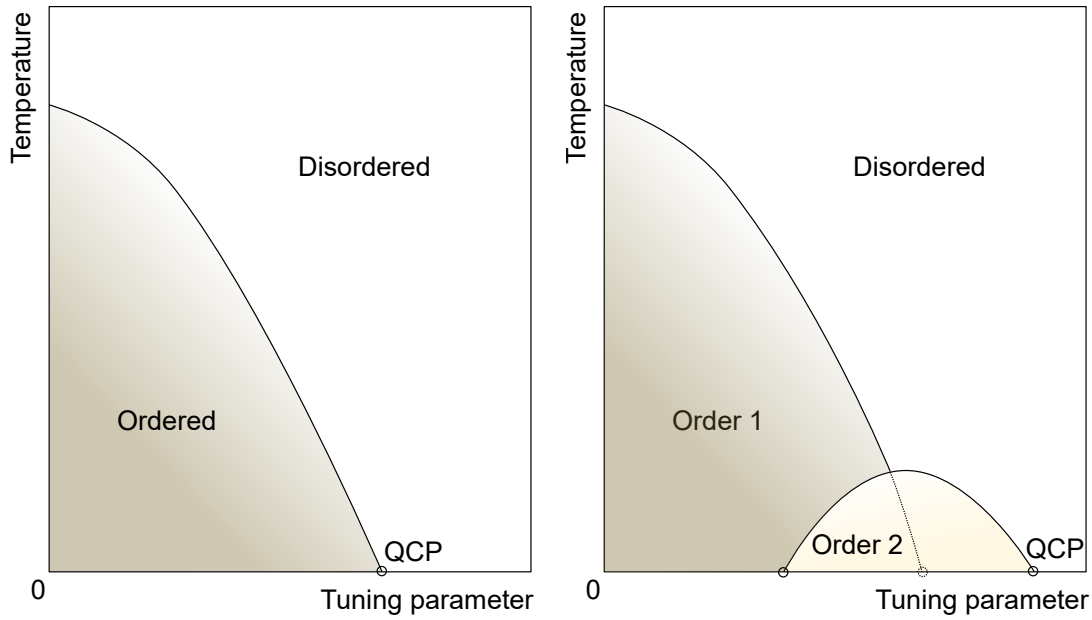

Fig. 1.1 Two simple cartoons showing the main features of phase diagrams with QCPs, which are indicated by small circles. (a) A continuous phase transition suppressed to zero temperature. (b) The QCP of Order 1 is masked by the formation of Order 2. These two orders may or may not coexist.

Quantum criticality is also associated with collective phenomena other than superconductivity. For instance, it can be observed in systems with structural transitions, which is a common feature seen in many perovskites and other related crystal structures. Perovskite

materials like $SrTiO_3$, oxygen-18 substituted $SrTiO_3$ and $KTaO_3$ near the ferroelectric (a type of structural transition, cf. Section 2.2) QCP display non-conventional T^2 temperature dependence in the dielectric function due to the QCP [12]. The phase diagram for these materials can also be represented schematically by Figure 1.1(a).

Structural quantum criticality can have unexpected effects on the material. A good example of this is the simple cubic perovskite material, ScF_3, where an unusual negative thermal expansion has been observed [13]. This material is close to a cubic-to-rhombohedral structural quantum phase transition [14]. A dramatic soft optical phonon branch is observed by inelastic x-ray scattering [14] which is related to the tilting of the ScF_6 octahedra. The collective fluctuations of these soft optical modes have been suggested to be the reason behind the negative thermal expansion [14, 15].

1.2 $A_3T_4Sn_{13}$ and YFe_2Ge_2

The work presented in this dissertation is centred on the experimental study of two materials: $A_3T_4Sn_{13}$ (A = Ca, Sr; T = Ir, Rh) and YFe_2Ge_2. Both materials have unconventional properties that are likely to be associated with critical fluctuations.

The two defining features of $A_3T_4Sn_{13}$ are its structural transition and superconductivity. The structural transition can be represented by the softening of three perpendicular, zone boundary phonon modes, which results in a doubling of the unit cell in each of the three directions [16]. This transition does not produce an electric polarisation, unlike ferroelectric or antiferroelectric transitions, and is known as an antiferroic transition [17]. The antiferroic transition can be easily tuned with physical pressure or chemical substitution [16, 18]. In addition, the transition is second-order and is well described by mean-field theory [18]. The superconductivity in $A_3T_4Sn_{13}$ has been shown to be nodeless [19] and the pairing mechanism is very likely to be conventional (phonon-mediated). The softening of part of the phonon spectrum enhances the electron-phonon coupling [20] and could explain the increase in superconducting T_c near the critical point.

An interesting connection can be made between the structure of the perovskites and the quasi-skutterudites $A_3T_4Sn_{13}$, as pointed out by Oswald et al. [21]. The tilting of the octahedra in the cubic perovskites results in the "triple-perovskite" structure. This is in turn very

similar to $A_3T_4Sn_{13}$ if the octahedra are replaced by TSn_6 trigonal prisms [21]. It is perhaps unsurprising that the quasi-skutterudites also has a structural transition.

In Chapter 3, we will present the fermiology of $Sr_3Ir_4Sn_{13}$. The main motivation behind this work is the surprising inconsistency between the conclusions of different x-ray diffraction (XRD) experiments. Klintberg et al. proposed that the structural transition is driven by the softening of three perpendicular, zone boundary phonon modes, resulting in a body-centred cubic (bcc) low-temperature structure [16]. Mazzone et al. argued that the refinement of the low-temperature phase to the bcc structure is poor. Instead, they proposed a picture of three twinned tetragonal domains, each driven by one of the three soft phonon modes, and they "mimic a higher symmetry" [22]. It is worth noting that Klintberg et al. studied the XRD of $Sr_3Ir_4Sn_{13}$ which is quite far from the critical point with a structural transition temperature $T^* = 147$ K, while Mazzone et al. investigated $Ca_3Ir_4Sn_{13}$, which is much closer to the critical point with $T^* = 38.5$ K.

By comparing the measured quantum oscillations of $Sr_3Ir_4Sn_{13}$ in the low-temperature phase to the DFT predictions for both the bcc and tetragonal domains scenarios, we hope to pin down the exact nature of the structural transition. This comparison is shown in Figure 3.8. While neither prediction is perfect, we think that the bcc scenario is a significantly better match to the experiment.

Following this, in Chapter 4, we will discuss effects of the structural QCP on the low-temperature lattice thermal transport properties of the $(Ca_xSr_{1-x})_3Rh_4Sn_{13}$ substitution series. Much like the case of ScF_3, the structural quantum criticality resulted in interesting and unconventional behaviours. Close to the structural critical point, the soft phonon mode should have a linear dispersion and a vanishing energy gap. Naively, one might expect the soft phonon mode to behave like an acoustic mode and contribute to lattice thermal conductivity. We exploit the nodeless superconductivity in this material to isolate the contribution of lattice from that of the electrons. By measuring thermal conductivity and heat capacity at temperatures much lower than T_c, we can freeze out the electronic contribution.

The result of our heat capacity measurement shows that at low temperatures ($T/T_c < 0.3$), $(Ca_xSr_{1-x})_3Rh_4Sn_{13}$ follows the expected T^3 behaviour due to lattice. The magnitude of the heat capacity is enhanced near the critical point. The thermal conductivity, on the other hand, shows a change in power law exponent from approximately 3 to 1.7 near the critical point (Figure 4.17). Moreover, the phonon mean free path at around 1 K is roughly between 2 to 10 μm, which is surprisingly small for crystalline samples. These observations are

inconsistent with specular reflections, umklapp scattering and scattering from point or line defects and suggest the existence of an unconventional phonon scattering mechanism.

We attempted to build a phenomenological model to explain our experimental results. We considered the fluctuations associated with the structural QCP and assumed that the acoustic phonons, which are primarily responsible for thermal conduction, are predominately scattered by these fluctuations. This model gives approximately the observed thermal conductivity power law but also predicts a very significant heat capacity contribution that contradicts the experimental data. A plausible, alternative explanation is that near the critical point, the material is *intrinsically disordered*. This could be due to a spatial distribution of the order parameter. In essence, this will destroy the crystallinity of the material and strongly scatter the acoustic phonons. If this picture is correct, it will also explain the unsatisfactory refinement of the low-temperature phase of $Ca_3Ir_4Sn_{13}$ to the bcc structure, since it is quite close to the critical point.

In Chapter 5, we will discuss the superconductivity in YFe_2Ge_2 using experimental data from thermal conductivity and heat capacity. This is motivated by the similarities between YFe_2Ge_2 at ambient pressure and KFe_2As_2 under high pressure in the collapsed tetragonal (cT) phase. Theoretically, it has been predicted that the pairing symmetry in iron-based superconductors is $s_\pm$ [23] and this is consistent with thermal conductivity experiments that suggest $Ba_{1-x}K_xFe_2As_2$ near optimum doping has nodeless superconductivity [24]. KFe_2As_2, however, has been shown to be nodal [25, 26] but the nodes are likely to be accidental rather than symmetry-imposed [27, 28]. This suggests that the fundamental pairing mechanism is unchanged across the phase diagram. It is natural to ask whether the superconductivity in KFe_2As_2 changes with applied pressure. This can be partially resolved by measuring YFe_2Ge_2, which has a very similar Fermi surface from DFT calculations [29].

In zero field, our thermal conductivity measurements shows a large κ_0/T (the zero temperature extrapolation of κ/T). This is more than 60% of the value κ_0/T when superconductivity is suppressed with magnetic field (Figure 5.9). This suggests that a significant fraction of quasiparticles remain in the normal state even at zero field and low temperatures (~ 50 mK) which is a strong evidence for nodal superconductivity. We can exclude the more trivial possibility that 60% of the sample is non-superconducting. By fitting to the heat capacity anomaly at T_c, we found that the upper bound on the non-superconducting fraction of the sample is about 20%. The zero-field measurement is corroborated by the magnetic field dependence of κ/T. There is a clear $\sqrt{H}$ dependence which is a result of the Volovik

effect in nodal superconductors. Fully-gapped superconductors should have an exponential field dependence. Our results strongly suggest that YFe_2Ge_2 has nodal superconductivity.

To conclude this introductory chapter, we will review the links of $A_3T_4Sn_{13}$ and YFe_2Ge_2 with our central theme of quantum criticality. In the case of $A_3T_4Sn_{13}$, there is a second-order structural transition which could be suppressed with physical or chemical pressure. The suppression of this transition enhanced the electron-phonon coupling and boosted the phonon-based superconductivity moderately. However, a much more dramatic effect of the structural criticality is, possibly, the creation of intrinsic disorder, which strongly suppresses lattice thermal transport. YFe_2Ge_2, on the other hand, is on the border of magnetic order. This is deduced both from theoretical calculations and from spectroscopic measurements. Similar to the iron-based superconductors, it is likely that magnetic fluctuations play a role in pairing in YFe_2Ge_2.

Chapter 2

Theoretical background and experimental methods

In this chapter, we will lay down the theoretical and experimental foundations upon which the later chapters will be built. We will first look at the framework of quantum criticality which underpins much of the modern research in condensed matter physics. Then, we will move on to the description of different types of structural transitions. The basics of density functional theory, with a focus on lattice dynamics, will then be reviewed. Following that, we will treat the phenomena of quantum oscillations and thermal conductivity and discuss the experimental methods used to measure them. Finally, this chapter will conclude with an introduction to a newly developed, extensible control software package called Flint.

2.1 Quantum criticality

Many interesting materials that we study, including $A_3T_4\mathrm{Sn}_{13}$ and $\mathrm{YFe}_2\mathrm{Ge}_2$, are found near quantum critical regimes. In this section, we will briefly outline the concepts of quantum criticality and the phenomenological method used by Lonzarich [30]. The starting point is a system of fermions interacting via a bosonic field. For example, in an itinerant ferromagnet, the fermions are electronic quasiparticles and the bosonic field is the effective magnetic field due to the exchange interaction. We could integrate out the fermions and just look at a fluctuating exchange field. This is similar to the Landau-Ginzburg treatment of fluctuations of the order parameter field [30].

For a system nearing a continuous, second-order phase transition at a finite temperature T_c, there is a distribution of coherent fluctuations in the order parameter field $\phi(\mathbf{r})$ in space and time with characteristic wavevector k_ϕ and frequency ω_ϕ. Both k_ϕ and ω_ϕ vanish at the transition. The time scale of the fluctuations in $\phi(\mathbf{r})$ defines an energy scale $\hbar\omega_\phi$ and the system can be treated classically if $\hbar\omega_\phi \ll k_B T_c$. However, for a system where the transition temperature can be driven to zero, fluctuations in $\phi(\mathbf{r})$ must be treated quantum mechanically [31] since T_c can be tuned to an arbitrarily small value. The earliest extension of the theory of critical phenomena to quantum phase transitions is due to Hertz [32] and Millis [33]. They suggested that for quantum phase transitions ($T_c = 0$), temporal and spatial fluctuations are intertwined [31] and that a d-dimensional quantum system is closely related to a classical system with $d+z$ dimensions [32], where z is the dynamical exponent defined by $\omega_\phi \sim k_\phi^z$, and the imaginary time variables lies in the finite interval of $[0, -i/k_B T]$ [32].

An alternative to the Hertz-Millis approach looks at the expansion of the bosonic field in terms of the order parameter field [30]. The functional form of this expansion is governed by empirical evidence and symmetry constraints [30], and the coefficients are ideally estimated from experimental data. Next, one calculates the susceptibility (which is the response function) of the order parameter to the bosonic field and finds the imaginary component which is the dissipation due to damping. Finally, we can make use of the fluctuation-dissipation theorem to link the imaginary part of the susceptibility to the fluctuations in the bosonic field [30]. We will see an example of such an approach in Section 4.4.3.

2.2 Structural transitions

There are three common types of structural transitions—ferroelectric, antiferroic and ferroelastic [17]. All three involve a lowering of symmetry compared to the high-temperature phase. A ferroelectric phase transition usually involves the displacement of cations relative to anions that induces a dielectric polarisation in the crystal. Prominent examples include the perovskites $BaTiO_3$ [34], $PbTiO_3$ [35] and ^{18}O-substituted $SrTiO_3$ [12]. In an antiferroic transition, also known as a "unit-cell combining" or "antiferroelastic" phase transition, the displacement of atoms in one unit cell is mirrored by displacement in the neighbouring unit cells in the opposite direction. The displacement of oxygen in $SrTiO_3$ at 105 K [36, 37], which can be visualised as rotation of the oxygen octahedra, is a good example. The $A_3T_4Sn_{13}$ material family, which we will discuss in detail in Chapters 3 and 4, also falls

under this category. Lastly, a ferroelastic transition is marked by the formation of spontaneous strain which is hysteretic and can reverse sign under the right stress [38]. This has been observed in $Pb_3(P_xV_{1-x}O_4)_2$ [39] and As_2O_5 [40]. Although a ferroelectric transition can result in spontaneous strain as well, such as the cubic to tetragonal transition in $PbTiO_3$, this is typically not considered to be ferroelasticity since the strain is proportional to the square of the polarisation and does not change sign [17]. These three types of structural transitions are illustrated in Figure 2.1.

2.2.1 Soft mode theory

Structural transitions can be described phenomenologically with the soft mode theory. The order parameter is the average static displacement of the atoms associated with the structural transition [41], and it is equal to zero in the high-temperature phase and finite below the transition temperature. For antiferroic transitions, the zone boundary becomes a new Bragg position at the transition temperature [42, 43] and the unit cell dimension(s) doubles.

The theory of soft mode at the Brillouin zone centre was first put forth by Anderson [44] and Cochran [45] to explain ferroelectric phase transitions. A zone boundary soft mode was then used by Unoki et al. [36] and Fleury et al. [42] to explain the 105 K antiferroic transitions in $SrTiO_3$. A crystal is stable against small deformation if all the harmonic frequencies are real [46]. However, a material with a ferroelectric or antiferroic transition will have one or more phonon modes with imaginary harmonic frequencies, and these modes will go "soft" at the structural transition temperature. This means that the frequency ω of the mode vanishes at T_c and the temperature dependence of the soft mode is given by [17]

$$\omega^2 = |\omega_0^2| \frac{T - T_c}{T_c}. \tag{2.1}$$

This is shown schematically in Figure 2.2. The harmonic frequency, ω_0^2, is the frequency that is calculated by DFT in the harmonic approximation (cf. Section 2.3.1) and it is negative. The physical reason for the temperature dependence of the soft mode is the failure of the harmonic approximation in describing the complex energy landscape that the nuclei are in. Corrections to the harmonic approximation will include quartic terms in the Hamiltonian, which under the mean-field approximation give temperature dependence to the modes [17]. Soft mode theory has worked very well in describing the 105 K antiferroic transition (also

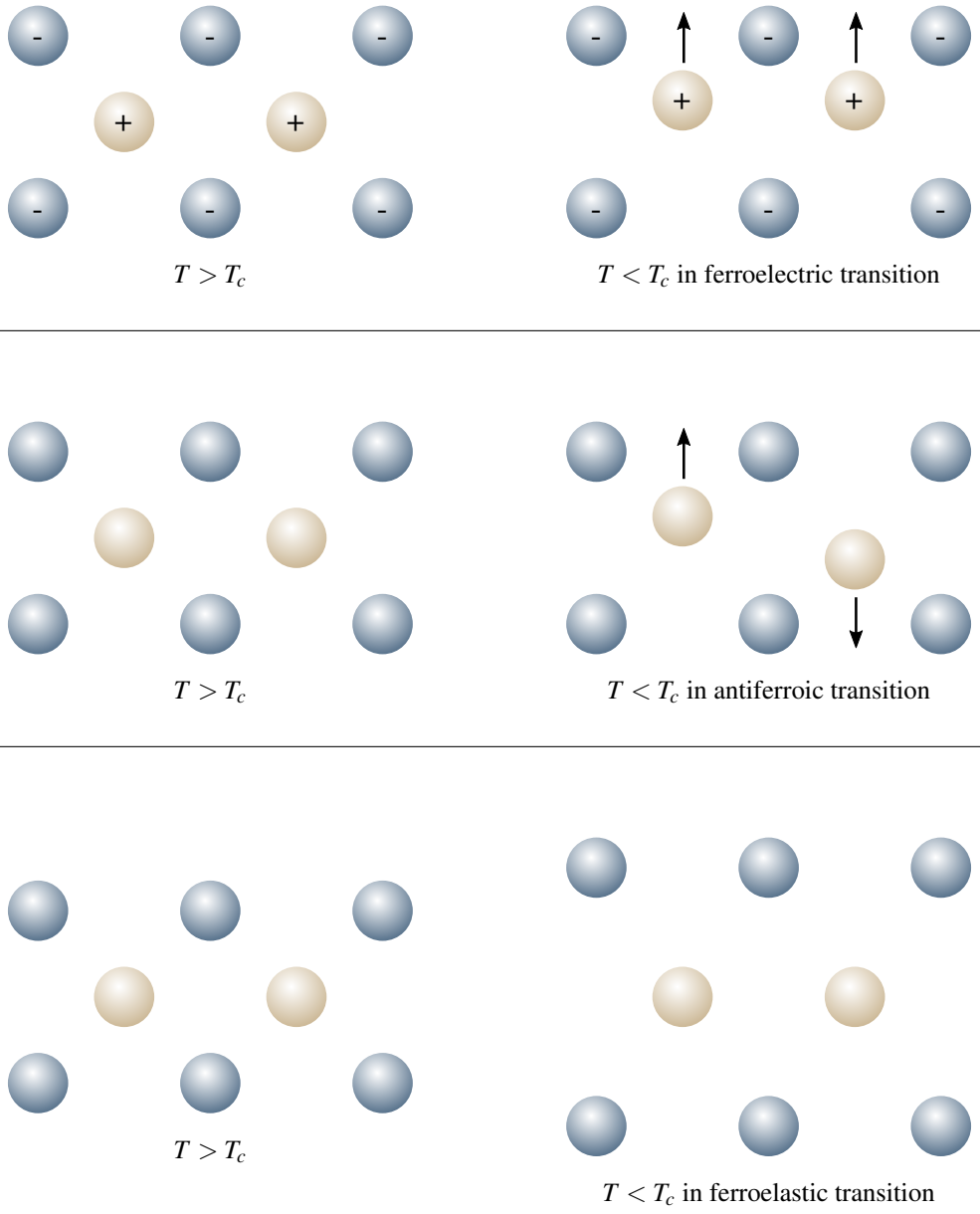

Fig. 2.1 A simple cartoon showing the different types of structural transitions. This is modified from similar illustrations in [17, 41]. Atoms with + and - labels are charged, and unlabelled atoms are neutral. There are several other kinds of displacive transitions which are not represented here. For example, if an antiferroic-like distortion occurs in a polarised crystal, it is known as an antiferroelectric transition. For a complete review of different kinds of displacive transitions, refer to Fig. 1.1 of [41].

known as the octahedral rotation phase transition in the literature) in $SrTiO_3$. The linear temperature dependence of the soft mode has been measured experimentally by inelastic neutron scattering [47].

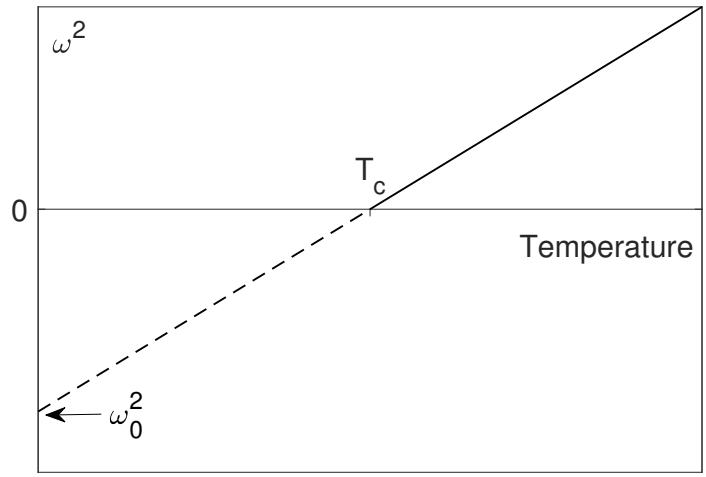

Fig. 2.2 The temperature dependence of the soft mode frequency shown schematically, modified from [17].

2.3 DFT

We will be using density functional theory (DFT) extensively in comparison to experimental results in the later chapters, so we shall briefly review the principles behind DFT, and in particular, outline how lattice vibrations can be calculated. DFT in its modern form is based on two pieces of seminal work by Hohenberg and Kohn [48] and Kohn and Sham [49]. Before DFT, attempts at solving the many-body quantum system focused on solving for the wavefunction $\mathbf{\Psi}(\mathbf{r}_1, \mathbf{r}_2, \cdots, \mathbf{r}_N)$ which is possible for small N but very quickly runs into an "exponential wall" for larger systems. This is because the size of the function space of a many-body wavefunction grows exponentially with the number of particles and for a wavefunction where $N \sim 10^3$, it is impossible to even find enough data storage to record the wavefunction, let alone solve for it [50]. DFT overcomes this problem by focusing on the ground state electron density

$$n(\mathbf{r}_1) = N \int d\mathbf{r}_2, \cdots, d\mathbf{r}_N \ |\mathbf{\Psi}(\mathbf{r}_1, \mathbf{r}_2, \cdots, \mathbf{r}_N)|^2 \tag{2.2}$$

instead of the wavefunction itself [51]. This is meaningful because Hohenberg and Kohn have shown that there is a one-to-one and invertible mapping between the external potential of the system $V_{\text{ext}}(\mathbf{r})$, the many-body wavefunction $\mathbf{\Psi}$, and the ground state density $n(\mathbf{r})$ [51]. $V_{\text{ext}}(\mathbf{r})$ represents the interaction of the electron with the nuclei and is specific to each system. Consequently, the ground state expectation value of any observable is a unique functional of $n(\mathbf{r})$. The ground state density $n(\mathbf{r})$ can be found by minimisation of the energy functional [48, 49],

$$E[n(\mathbf{r})] = \int d\mathbf{r}\, V_{\text{ext}}(\mathbf{r}) n(\mathbf{r}) + F_{\text{HK}}[n]. \tag{2.3}$$

The second term F_{HK} is a universal functional of the density but is not known. The practical calculation of density in DFT is carried out using the Kohn-Sham scheme. Instead of solving for the interacting system, Kohn and Sham [49] proposed solving for an auxiliary system of non-interacting particles (labelled here with subscript s) with the *same density* as the interacting system, assuming that such a system exists. This auxiliary system is defined by the Kohn-Sham Schrödinger-like equations [52]

$$\left(-\frac{1}{2}\nabla^2 + V_{\text{ext}}(\mathbf{r}) + V_{\text{Hartree}} + V_{\text{xc}}\right)\psi_{s,i}(\mathbf{r}) = \varepsilon_{s,i}\psi_{s,i}(\mathbf{r}), \tag{2.4}$$

where the potentials $V_{\text{Hartree}} = \frac{\delta E_{\text{Hartree}}[n]}{\delta n}$ and $V_{\text{xc}} = \frac{\delta E_{\text{xc}}[n]}{\delta n}$ are defined in terms of functional derivatives. The density of this auxiliary system, which is equals to the density of the interacting system, is

$$n(\mathbf{r}) = \sum_i |\psi_{s,i}(\mathbf{r})|^2 . \tag{2.5}$$

The Hartree energy, E_{Hartree}, is

$$E_{\text{Hartree}}[n] = \frac{1}{2}\iint d\mathbf{r} d\mathbf{r}'\, \frac{n(\mathbf{r})n(\mathbf{r}')}{|\mathbf{r}-\mathbf{r}'|}. \tag{2.6}$$

The exchange-correlation functional $E_{\text{xc}}[n]$ is defined in terms of the universal functional

$F_{\mathrm{HK}}[n]$ as [49, 52]

$$F_{\mathrm{HK}}[n] = T_s[n] + E_{\mathrm{Hartree}}[n] + E_{\mathrm{xc}}[n], \tag{2.7}$$

where $T_s[n]$ is the kinetic energy of the auxiliary system. All the complexity of the interacting system is contained in $E_{\mathrm{xc}}[n]$ which has to be approximated using various methods. The Kohn-Sham scheme works because T_s accounts for a large part of the energy and E_{xc} is more easily approximated locally [53].

The simplest approximation of the exchange-correlation functional E_{xc} is the local density approximation (LDA). In this approximation [52], the exchange-correlation functional is an integral over all space of the density and the exchange-correlation energy density, $\mathcal{E}_{\mathrm{xc}}$,

$$E_{\mathrm{xc}}[n] \simeq E_{\mathrm{xc}}^{\mathrm{LDA}}[n] = \int d\mathbf{r}\, n(\mathbf{r})\mathcal{E}_{\mathrm{xc}}(n). \tag{2.8}$$

The exchange-correlation energy density, $\mathcal{E}_{\mathrm{xc}}$, is approximated by that of a homogeneous electron gas which can be calculated using Monte Carlo methods [52]. More advanced methods of approximating the exchange-correlation functional, such as the generalised-gradient approximation (GGA), include more terms such as the density gradient ∇n term in $\mathcal{E}_{\mathrm{xc}}$.

The Kohn-Sham equations can be solved self-consistently using the following scheme [52].

1. Start with an initial guess of the electron density, $n(\mathbf{r})$.

2. Use Equations 2.6 and 2.8 to calculate the effective potentials.

3. Solve Equation 2.4 by energy minimisation.

4. Calculate the new density using Equation 2.5.

5. If the change in the density is sufficiently small, the calculation has concluded. Otherwise, return to step 2 with the new density.

2.3.1 Phonon spectrum

Under the Born–Oppenheimer approximation [54], the electronic and lattice degrees of freedom can be treated separately as the nuclei move much more slowly than the electrons. Hence, the electron density and ground state energy can be calculated assuming fixed nuclear positions. To obtain the phonon spectrum, we need to calculate the electronic ground state energy E as a function of the set of all nuclei positions, $\mathbf{R}$. Once this quantity is obtained, the nuclei can be treated classically, and for the i^{th} nucleus with mass M_i,

$$M_i \frac{\partial^2 \mathbf{R}_i}{\partial t^2} = -\frac{\partial E(\mathbf{R})}{\partial \mathbf{R}_i}. \tag{2.9}$$

In a molecule, under the harmonic approximation, the displacement from the equilibrium position can be written as $\mathbf{u}_i(t) = \mathbf{R}_i(t) - \mathbf{R}_i^0 = \mathbf{u}_i e^{i\omega t}$. The vibrational frequencies ω and normal modes $\mathbf{u}$ can be found by solving the eigenvalue equation [52]

$$\sum_j \frac{1}{\sqrt{M_i M_j}} \frac{\partial^2 E(\mathbf{R})}{\partial \mathbf{R}_i \partial \mathbf{R}_j} \mathbf{u}_j = \omega^2 \mathbf{u}_i. \tag{2.10}$$

In a crystal, Bloch's theorem is used to find the phonon frequency $\omega_{\mathbf{k}}$ and normal mode displacements $\mathbf{u}_i(\mathbf{k})$ at every wavevector $\mathbf{k}$ [52]. The index i runs through every nucleus in the unit cell.

The simplest and most direct way to calculate $E(\mathbf{R})$ is to repeatedly calculate the electronic ground state energy for different nuclear positions. This is known as the "frozen phonon" method [55]. Calculations of the dispersion are possible only at certain wavevectors $\mathbf{G}/N$, where $\mathbf{G}$ is a reciprocal lattice vector. However, this requires the construction of supercells N times the original unit cell in the direction of $\mathbf{G}$ [56], which is computationally expensive. In this work, the phonon spectrum calculations are done with Quantum ESPRESSO, which implements the density functional perturbation theory (DFPT) method [57]. In DFPT, phonons, which are essentially small changes in the external potential ΔV_{ext}, are treated as perturbations to the Kohn-Sham Hamiltonian in Equation 2.4. The corresponding changes to the Kohn-Sham orbitals $\Delta\psi_{s,i}$ and changes in density Δn are computed using first-order perturbation theory [58]. These quantities can be calculated using a self-consistent procedure, which is the approach used in Quantum ESPRESSO [57]. The main advantage of

the DFPT approach is that it allows for calculations of phonon modes at arbitrary wavevectors without the use of supercells [58], which is very important for large systems like the $A_3T_4\mathrm{Sn}_{13}$ materials (cf. Section 4.2).

2.4 Quantum oscillations

In Chapter 3, we will be presenting our quantum oscillations data, so it is important to first sketch out the theoretical basis for this phenomenon. We will use the same semi-classical approach as Shoenberg [59]. First, we will consider a classical system of a charged particle performing cyclotron motion under a magnetic field. Then, we will quantise said system to arrive at the Onsager relation. We will show that the density of states will be modulated periodically in inverse field, which will ultimately result in oscillations of many physical properties of the material such as electrical resistivity and magnetic susceptibility. Finally, we will conclude by stating some of the effects of finite temperature, sample impurities and spin splitting, thus arriving at the Lifshitz–Kosevich (LK) formula.

In the classical picture, the rate of change of momentum ($\mathbf{k}$) of an electron moving at velocity $\mathbf{v}$ due to the Lorentz force in a magnetic field $\mathbf{B}$ is $\hbar\dot{\mathbf{k}} = -e\mathbf{v}\times\mathbf{B}$. Integrating with respect to time, we get

$$\hbar(\mathbf{k}-\mathbf{k}_0) = -e(\mathbf{R}-\mathbf{R}_0)\times\mathbf{B}. \tag{2.11}$$

Moving on to the quantum picture, we can use the Bohr-Sommerfeld quantisation rule for periodic motion

$$\oint \mathbf{p}\cdot d\mathbf{q} = 2\pi\hbar\left(l+\frac{1}{2}\right), \tag{2.12}$$

where $\mathbf{p}$ and $\mathbf{q}$ are canonically conjugate momentum and position variables, l is an integer, and the integration is performed around the closed path of the particle [59]. In a magnetic field, the conjugate variables should be $\mathbf{p} = \hbar\mathbf{k} - e\mathbf{A}$ and $\mathbf{q} = \mathbf{R}'$, where $\mathbf{A}$ is the vector

potential ($\mathbf{B} = \nabla \times \mathbf{A}$). Substituting this into Equation 2.12 and using Equation 2.11 to express $\mathbf{k}$ in terms of $\mathbf{R}$ and $\mathbf{B}$, we obtain

$$\oint (-e\mathbf{R} \times \mathbf{B} - e\mathbf{A})\, d\mathbf{R}' = 2\pi\hbar \left(l + \frac{1}{2}\right). \tag{2.13}$$

We can re-express the first term using the circular-shift property of scalar triple products and the second using Stokes' theorem, $\oint \mathbf{A}\, d\mathbf{R}' = \int_{\mathbf{S}} \nabla \times \mathbf{A}\, d\mathbf{S}$, where $\mathbf{S}$ represents the area of the orbit in real space [59]:

$$\mathbf{B} \cdot \oint \mathbf{R} \times d\mathbf{R}' - \int_{\mathbf{S}} \mathbf{B} \cdot d\mathbf{S} = \frac{2\pi\hbar}{e} \left(l + \frac{1}{2}\right). \tag{2.14}$$

The left-hand side gives $B\mathcal{A}_{l,R}$, where $\mathcal{A}_{l,R}$ is the area of the l^{th} orbit in real space. This is related to the momentum space area, $\mathcal{A}_l$, by a scaling factor such that $\mathcal{A}_l = \left(\frac{eB}{\hbar}\right)^2 \mathcal{A}_{l,R}$ [59]. Combining this with Equation 2.14 will also give us the Onsager relation [60]

$$\mathcal{A}_l = \frac{2\pi eB}{\hbar} \left(l + \frac{1}{2}\right). \tag{2.15}$$

Equation 2.15 heavily restricts the locations of the electron in momentum space onto Landau tubes, shown in Figure 2.3. This modifies the density of states (DOS) such that it becomes a function of field. For a material with a uniform Fermi surface (cross-sectional area $\mathcal{A}_F$) along the direction of the field (for example, a cylindrical Fermi surface), the DOS is at its maximum when one of the many Landau tubes matches up with the Fermi surface such that $\mathcal{A}_l = \mathcal{A}_F$. The period between the l^{th} Landau tube satisfying that criterion and the next one is $\Delta(1/B) = 2\pi eB/\hbar\mathcal{A}_F$, and the quantum oscillation frequency (in units of magnetic field) is [61]

$$F \equiv \frac{1}{\Delta(1/B)} = \frac{\hbar}{2\pi e}\mathcal{A}_F. \tag{2.16}$$

For more complicated Fermi surfaces, the quantum oscillation frequency reflects only the extremal cross-sectional area of the Fermi surface perpendicular to the field. This is because the DOS only changes weakly as Landau tubes slide across other parts of the Fermi surface,

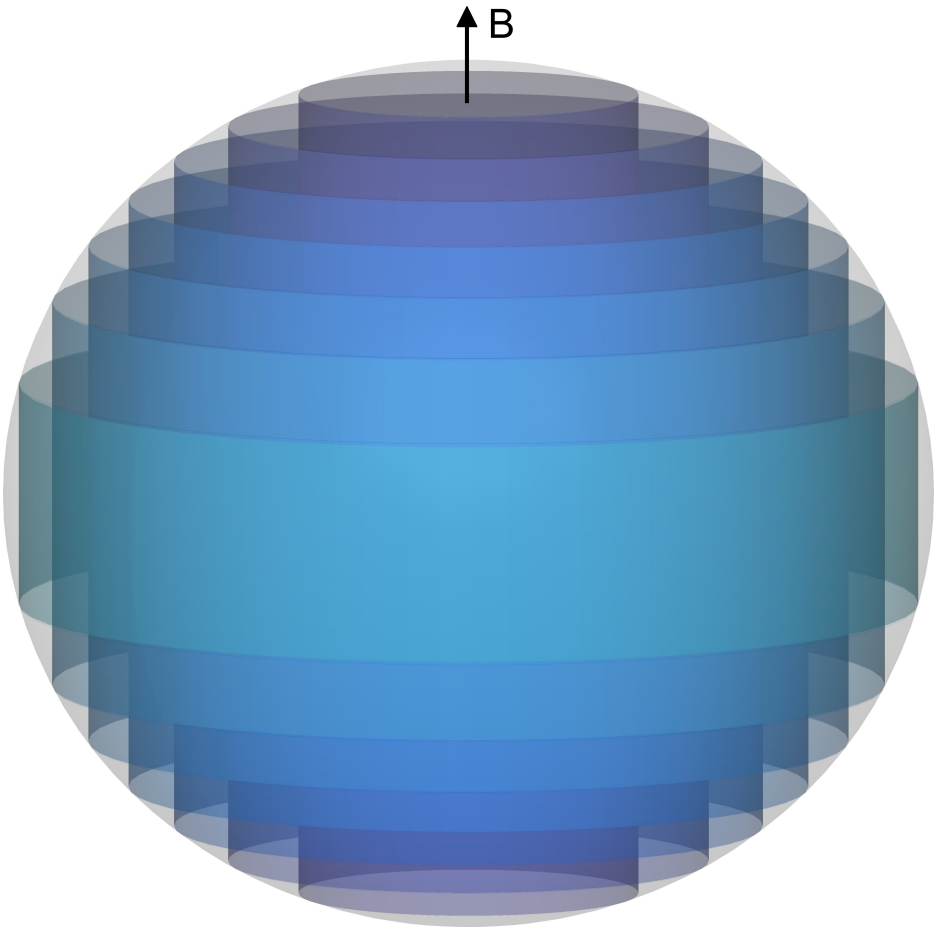

Fig. 2.3 Modified from [59]. Schematic diagram in momentum space showing Landau quantisation in the presence of a magnetic field indicated by the black arrow, in a material with a spherical Fermi surface.

and only at the extremal cross section does a tube periodically separate from the Fermi surface and give a sudden change to the DOS [62].

The Lifshitz–Kosevich (LK) formula for the oscillatory part of the DOS per unit volume at the Fermi level ($\tilde{\mathcal{D}}$), is given by [59]

$$\tilde{\mathcal{D}} = \sqrt{\frac{2eB}{\hbar}} \frac{m^* R_D R_S}{\pi^{3/2}\hbar^2 \left|\frac{\partial^2 \mathcal{A}_F}{\partial k_\parallel^2}\right|^{1/2}} \sum_{p=1}^{\infty} \frac{1}{\sqrt{p}} \cos\left(2\pi p \left(\frac{F}{B} - \frac{1}{2}\right) \pm \frac{\pi}{4}\right). \tag{2.17}$$

The wavevector $k_\parallel$ is parallel to the direction of the magnetic field, R_D and R_S are amplitude reduction factors that we will discuss later, and p is the order of the harmonic ($p = 1$ for the fundamental frequency). The electronic DOS at the Fermi surface determines many physical properties of the metal, and they will in turn display quantum oscillations. One commonly measured physical quantity where quantum oscillations could be detected is electrical resistivity (Shubnikov-de Haas effect). An order of magnitude estimate of the oscillatory part of electrical conductivity ($\tilde{\sigma}$) as a fraction of the constant part (σ) for the fundamental frequency, is given by [59, 63]

$$\begin{aligned} \frac{|\tilde{\sigma}|}{\sigma} &\sim R_T \frac{|\tilde{\mathcal{D}}|}{\mathcal{D}} \\ &\sim R_T R_D R_S \sqrt{\frac{B}{2F}} \end{aligned} \tag{2.18}$$

The non-oscillatory part of the DOS at the Fermi level is $\mathcal{D}$ and R_T is yet another reduction factor.

The amplitude of quantum oscillations is affected by several factors such as temperature T, electron relaxation time τ and spin splitting. These effects can all be understood under the intuitive concept of phase smearing. An ideal measurement is one that is on a completely homogeneous, defect-free ($\tau = \infty$) sample at $T = 0$. The effect of phase smearing can be represented as a distribution of ideal samples, each oscillating with a slightly different phase, which will reduce the amplitude of the total oscillations.

At finite temperatures, the Fermi surface is smeared out by the Fermi-Dirac distribution function $f(\varepsilon)$ and is not sharply defined. The associated reduction factor is

$$R_T = \frac{x}{\sinh x}, \tag{2.19}$$

where $x = 2\pi^2 p k_B T m^*/e\hbar B$ [59]. The quasiparticle mass, m^*, has been renormalised to account for electron-electron and electron-phonon interactions [64] and is given by Equation 2.22. This is discussed in greater detail later.

Electrons in cyclotron orbits scatter with a relaxation time of τ. By the uncertainty principle, the Landau energy levels must have finite widths $\sim \hbar/\tau$. This reduces the oscillation amplitude by the Dingle factor [64, 65]

$$R_D = \exp\left(-\frac{\pi p}{\omega_c \tau}\right) = \exp\left(-\frac{\pi p m_b}{eB\tau}\right), \tag{2.20}$$

where m_b is the band mass. We can obtain τ by fitting the exponential change of amplitude with magnetic field. If we then assume a circular extremal cyclotron orbit such that $\mathcal{A}_F = \pi k_F^2$, the Fermi velocity will be given by $v_F = \sqrt{2\hbar e F}/m_b$. The mean free path is then obtained by the expression $l_{\text{mfp}} = v_F \tau$ [59]. The relaxation rate also defines a temperature scale $T_{\text{Din}} = h/k_B\tau$ called the Dingle temperature.

The effect of the Zeeman splitting in a magnetic field introduces a phase difference between oscillations from electrons with opposite spins. For free electrons, this phase difference is exactly 2π since the size of the spin-split equals the energy difference between Landau levels. In real materials, the spin-splitting reduction factor is [59, 64]

$$R_S = \cos\left(\frac{\pi p g \Sigma m_b}{2m_e}\right), \tag{2.21}$$

where the electron g-factor is $g = 2.0023 \simeq 2$, Σ is the Stoner enhancement factor and m_e is the bare electron mass.

So far, we have only considered the non-interacting system. Given that a real metallic sample has strong electron-electron and electron-phonon interactions, it is amazing that the effects of these many-body interactions in many cases can simply be treated as a shift in the

particle's energy $\Delta(\xi)$ and a broadening of the particle's linewidth $\Gamma(\xi)$ [59], where ξ is the energy difference from the chemical potential. Furthermore, if $\Delta(\xi) \sim -\lambda\xi$ and $\Gamma(\xi)$ is small, then the effect of the interaction is to modify the mass in the temperature smearing term R_T such that

$$m^* = (1+\lambda)m_b. \tag{2.22}$$

For electron-phonon interactions, λ is the electron-phonon coupling constant. It is given by $\lambda = 2\int_0^\infty \frac{d\nu}{\nu}\alpha^2(\nu)F(\nu)$, where $F(\nu)$ is the phonon DOS and $\alpha(\nu)$ is the electron-phonon coupling strength [59]. In metals, the electronic heat capacity is enhanced by a factor of $(1+\lambda)$ over the band value [66]. This coupling constant is also used in the Migdal-Eliashberg theory [67] to calculate T_c for a phonon-mediated superconductor.

We can now estimate the order of magnitude of Shubnikov-de Haas (SdH) quantum oscillations from Equation 2.18. We will consider a material with light mass ($m^*/m_b \sim 1$), moderate level of disorder ($T_{\mathrm{Din}} \sim 100$ K), frequency of $F \sim 1$ kT that is measured at $T \sim 100$ mK and $B \sim 18$ T. In this example, R_T and $|R_S|$ are close to unity, $R_D \sim 2\%$ and $\frac{|\tilde{\sigma}|}{\sigma} \sim 0.2\%$.

2.4.1 Low noise electrical resistivity measurement

From the previous section, we know that the magnitude of SdH quantum oscillations is typically tiny. Therefore, we always use the 4-point geometry when measuring the resistance of a sample. In this way, we can exclude the resistances of the contacts and leads which could potentially be much larger than that of the sample. In addition, quantum oscillations can easily be obscured by the electrical noise of the measurement device. Hence, we need instruments with very good signal-to-noise ratios and they need to be matched carefully so that the signal is not drowned out by the input noise of any instrument. Here, we will discuss some common sources of noise, and ways to minimise them.

There are three main types of noise—thermal noise, shot noise and $1/f$ noise [68]. Thermal noise, also known as Johnson-Nyquist noise, was first observed by Johnson in 1926 and explained by Nyquist soon after [69, 70]. It is due to the kinetic motion of electrons in a conductor at finite temperatures. Although the average current is zero, there are spontaneous currents which create voltages across the ends of the conductor. Under the framework of the

fluctuation-dissipation theorem, thermal noise consists of the equilibrium fluctuations associated with the resistance of a conductor, when a voltage is applied in the non-equilibrium state. The root mean square of the noise voltage V_{thermal} is given by

$$V_{\text{thermal}} = \sqrt{4k_B T R\,\Delta f}, \tag{2.23}$$

where R is the resistance of the conductor and Δf is the noise bandwidth of the measuring system.

Shot noise arises from the fact that charge is not continuous, but is carried by discrete electrons and is an important consideration when very small currents are used. The root-mean-square noise voltage V_{shot} is given by

$$V_{\text{shot}} = \sqrt{2qI\,\Delta f}\,R, \tag{2.24}$$

where q is the elementary charge and I is the direct current.

Lastly, $1/f$ noise has a $1/f^{\alpha}$ frequency dependence, where α is observed to be between 0.8 and 1.3 [68]. This is in contrast to the previous two sources of noise, which are mainly white noise or frequency-independent noise. In semiconductor devices, it is associated with the surface impurities of the material. It is very common, and no electronic amplifiers are free from it.

We will now estimate the noise level at every stage of a typical measurement circuit optimised for SdH (cf. Chapter 3), and we will show that our noise level is close to being Johnson noise limited. This circuitry is illustrated in Figure 2.4. The voltage leads of the sample, in a 4-point resistivity geometry, are connected to a CMR LTT-m low-temperature transformer with a turns ratio of 1:300 via Nb_3Sn twisted superconducting wire pairs. Output from the transformer is fed to a Brookdeal 5004 Ultra-Low Noise Preamplifier with $\times 100$ gain, then to a Stanford Research Systems SR830 Lock-In Amplifier (LIA). The current is supplied by a current source built by the Cavendish Electronic Workshop which is modulated by the sinusoidal voltage output of the LIA.

The typical metallic samples that we measure have low-temperature resistances of order 100 $\mu\Omega$. Compared to typical contacts made with conductive silver epoxy, which have

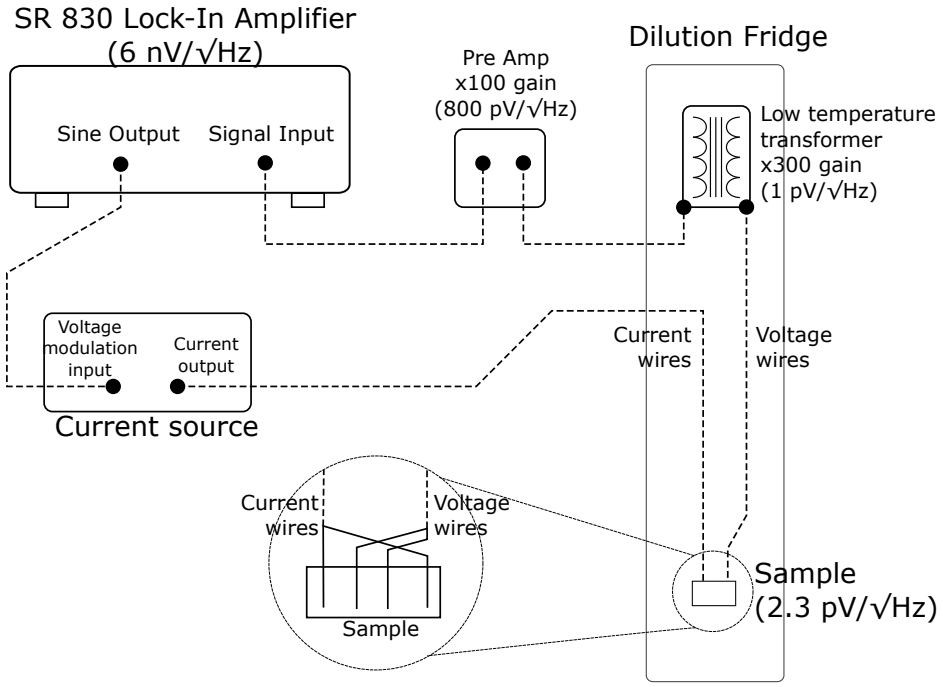

Fig. 2.4 Schematic diagram of the measurement circuit. The dashed lines represent twisted wire pairs, and the sample blow-up shows the 4-point geometry. The estimated typical input noise of the electrical components at normal operating frequencies of 100–200 Hz are stated in parentheses. The gain of the low-temperature transformer is reduced at higher frequencies and $1/f$ noise is significant at lower frequencies.

contact resistances of the order of 1 Ω, it is clear that the Johnson noise will be dominated by contact resistance. Substituting this value and a temperature of 100 mK into Equation 2.23, we obtain a noise of 2.3 pV/$\sqrt{\text{Hz}}$. For the calculation of shot noise, we need to use the resistance of the sample instead of contact resistance. Due to the 4-point geometry shown in Figure 2.4, shot noise due to current contact resistance is not picked up by the voltage leads. Shot noise of the voltage contacts is negligible because there is almost no current flow due to the high input impedance of the preamplifier. For an average metallic sample with resistance of about 100 $\mu\Omega$, the current we use is about 100 μA to avoid excessive heating. Substituting these values into Equation 2.24, we obtain a negligible noise level of 0.6 fV/$\sqrt{\text{Hz}}$. The exact $1/f$ noise level is difficult to calculate. However, we operate at as high a frequency as possible, typically at 100–200 Hz. Hence, the total noise level at this stage is mainly due to Johnson noise, which is about 2.3 pV/$\sqrt{\text{Hz}}$. This is higher than the input noise of the low-temperature transformer, which is approximately 1 pV/$\sqrt{\text{Hz}}$ [71]. The output noise from the transformer is of order 1 nV/$\sqrt{\text{Hz}}$, which is again higher than the input noise of preamplifier, which is 0.8 nV/$\sqrt{\text{Hz}}$ [72]. Finally, with a $\times$100 gain, the preamplifier ensures that its output noise is much larger than the input noise of the SR830 LIA, which is 6 nV/$\sqrt{\text{Hz}}$ [73]. At every stage, we know that the noise performance is limited by the source, instead of the equipment. We expect to see a final noise level of about 200 nV/$\sqrt{\text{Hz}}$, and that is indeed similar to what we observed experimentally, which is in the range of 100–500 nV/$\sqrt{\text{Hz}}$.

2.5 Thermal conductivity

A rigorous, microscopic treatment of any transport phenomenon is usually riddled with difficulties. Here, we will briefly outline the simplest, empirically accurate description of thermal conductivity in real materials, which is the kinetic model. In this model, electrons and phonons are treated as particles that carry heat and are scattered by defects and other particles. Let us consider an isotropic material with particle density n, velocity $\mathbf{v}$ and heat capacity per particle of c. A particle moving in a temperature gradient ∇T experiences a rate of change of energy [62]

$$\frac{dE}{dt} = c\mathbf{v} \cdot \nabla T, \tag{2.25}$$

assuming it is always in thermal equilibrium with its surroundings. If the average time between scattering is τ, the average heat transfer per particle is $c\tau\mathbf{v}\cdot\nabla T$. Multiplying this by the particle flux $n\mathbf{v}$ and averaging the velocity over all direction gives the heat flux [62]

$$\begin{aligned}\mathbf{U} &= -nc\tau\left\langle\mathbf{vv}\right\rangle\nabla T \\ &= -\frac{1}{3}nc\tau\left\langle v\right\rangle^2\nabla T,\end{aligned} \tag{2.26}$$

where $\left\langle v\right\rangle^2 = 3\left\langle\mathbf{vv}\right\rangle$ is the mean-square particle velocity, assuming $\mathbf{v}$ is isotropic. The thermal conductivity κ is then given by [62]

$$\kappa = \frac{1}{3}C\left\langle v\right\rangle l, \tag{2.27}$$

where $C = nc$ is the total volumetric heat capacity and $l = \left\langle v\right\rangle\tau$ is the mean free path of the particle. In a metal, there are two types of heat carriers—electrons (κ_e) and phonons (κ_{ph}), and the total conductivity is simply the sum of the two [74]. For an electron gas at low temperatures, only the electrons near the Fermi level contribute to the electronic heat capacity, which can be written as [62]

$$C_e = \frac{1}{3}\pi^2 k_B^2 T N_f = \frac{\pi^2 k_B^2 nT}{m_e\left\langle v\right\rangle^2}, \tag{2.28}$$

where N_f is the electronic density of states at the Fermi level. The electrical conductivity under the Drude model is

$$\sigma = \frac{ne^2 l}{m_e\left\langle v\right\rangle}, \tag{2.29}$$

where m_e is the electron mass. Using Equations 2.27, 2.28 and 2.29, we find that the ratio of the electronic thermal conductivity to the electrical conductivity is

$$\frac{\kappa_e}{\sigma} = \frac{1}{3}\left(\frac{\pi k_B}{e}\right)^2 T = \mathcal{L}_0 T. \tag{2.30}$$

This is the Wiedemann-Franz Law (WFL), and $\mathcal{L}_0 = 2.44 \times 10^{-8}$ WΩ/K^2 is the Lorenz number.

A more rigorous treatment of thermal conductivity, still within the confines of the kinetic model, is the Boltzmann transport theory. We assume that the system is close to equilibrium, and the number of particles in state k follows a statistical distribution f_k, which is a function of position $\mathbf{r}$ [62]. The type of distribution depends on the type of particles (fermions, bosons or classical particles) in the system. There are various mechanisms—diffusion, external field and scattering, which result in changes in $f_k(\mathbf{r})$. If we assume that, overall, $f_k(\mathbf{r})$ does not change with time, this implies that the various mechanisms balance.

In the absence of electric or magnetic fields, the rate of change of the distribution due to diffusion driven by a thermal gradient is cancelled out by that of scattering. This can be written as [62]

$$\begin{aligned} -f_k'\Big|_{\text{diffusion}} &= \mathbf{v}_k \cdot \nabla f_k \\ &\simeq \mathbf{v}_k \cdot \frac{\partial f_k^0}{\partial T} \nabla T \\ &= f_k'\Big|_{\text{scattering}}, \end{aligned} \tag{2.31}$$

where $\mathbf{v}_k$ are the velocities of the particles and f_k^0 is the equilibrium distribution without a thermal gradient. The scattering term $\left(f_k'\Big|_{\text{scattering}} \right)$ describes the coupling of states of different momentum k, subject to constraints from energy and momentum conservation. Equation 2.31 can be solved approximately for small deviations from the equilibrium distribution. Once the distribution function, f_k, has been obtained, the heat flux ($\mathbf{U}$) is given by [62]

$$\mathbf{U} = \int E_k \mathbf{v}_k f_k \, dk, \tag{2.32}$$

where E_k is the energy of the particle. Then, the thermal conductivity can easily be found. In Section 4.4.2, we will use the results of the Boltzmann transport theory, applied to phonons, to estimate lattice thermal conductivity in $A_3T_4\text{Sn}_{13}$.

2.5.1 Thermal conductivity of superconductors

Thermal conductivity is a reliable, powerful and bulk-sensitive experimental technique for studying superconductivity and other collective phenomena. For example, it has provided strong constraints on the superconducting gap symmetries of unconventional superconductors [75, 76]. We will be relying on this experimental probe to find the gap structure of YFe_2Ge_2 in Chapter 5, and hence we will briefly review the key ideas here. There are three main types of gap structures which can be differentiated with thermal conductivity. These are the nodeless s-wave gap, the s-wave gap with accidental nodes and the gap with symmetry-imposed nodes (e.g. p and d-wave). They are shown schematically for a quasi-two-dimensional tetragonal superconductor in Figure 2.5 [77]. There is an important difference between the two types of nodal gaps. The gap with accidental nodes, like the nodeless gap, has the full symmetry of the lattice (in this example, tetragonal) while the gap with symmetry-imposed nodes has a lower symmetry.

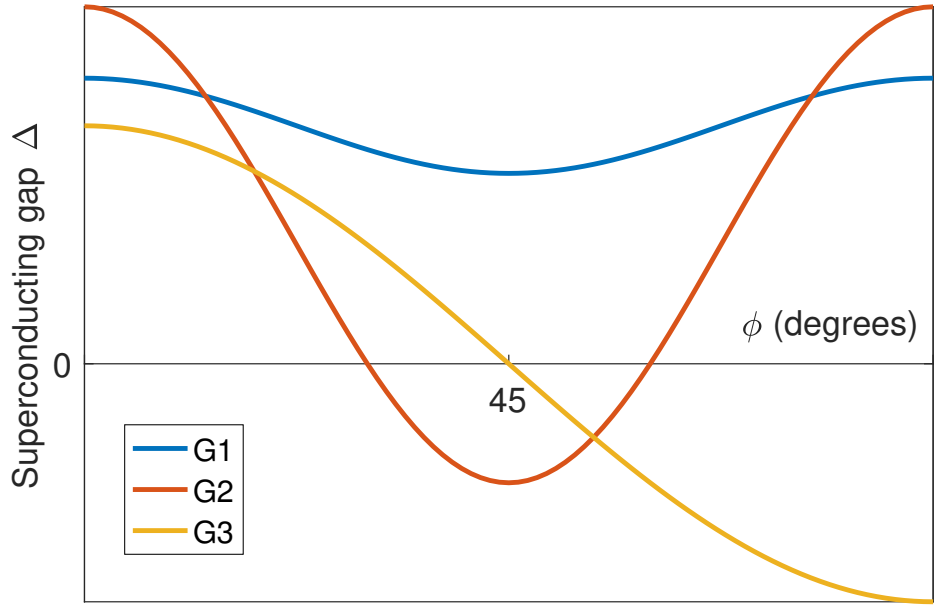

Fig. 2.5 Three types of superconducting gap structures, $|\Delta(\phi)|$ in a quasi-two-dimensional superconductor, where ϕ is the angle in the basal plane. The different types of gap structures are: (G1) nodeless gap, (G2) gap with accidental nodes and (G3) gap with symmetry-imposed nodes.

The T-linear thermal conductivity at zero temperature, denoted by κ_0/T in the literature, is usually estimated by extrapolating κ/T from low temperatures ($\sim$50 mK) to zero temperature. For a fully-gapped superconductor, the electronic thermal conductivity (κ_e) is

exponentially suppressed below T_c, and κ_0/T is zero. A classic example is the *s*-wave superconductor $NbSe_2$ in zero magnetic field which has zero κ_0/T within experimental errors [78]. Another example is the elemental superconductor, tantalum, which was studied by Connolly and Mendelssohn [79]. By fitting the theoretical thermal conductivity of electrons in the superconducting phase [80] to the total thermal conductivity data, Connolly and Mendelssohn separated contributions from the electronic and phonon channels (see Figure 2.6). They showed that above $T/T_c \sim 0.6$, thermal conductivity is almost entirely electronic; but by about $T/T_c \sim 0.3$, it is almost completely due to the lattice. This also explains the peak in thermal conductivity in the superconducting phase, which is due to the rapid increase of phonon mean free path from the reduction of electron-phonon scattering [79]. At the peak, another phonon scattering mechanism—in this case, boundary scattering—begin to dominate and thermal conductivity decreases with decreasing temperature. We will also see similar behaviours in the $(Ca_xSr_{1-x})_3Rh_4Sn_{13}$ system in Section 4.3.4, although they are complicated by unconventional phonon-scattering effects.

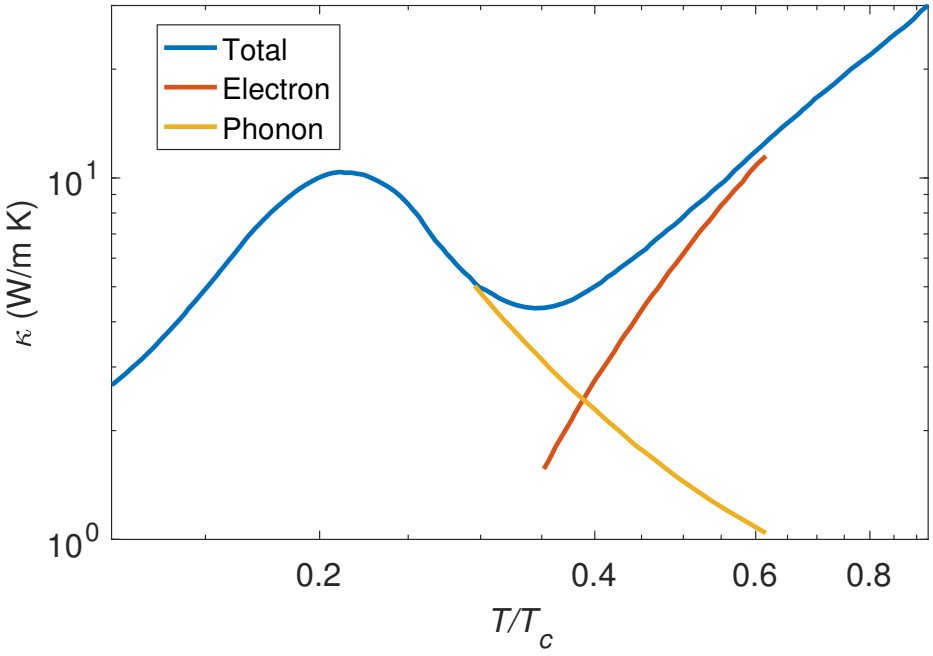

Fig. 2.6 Data from [79]. Thermal conductivity of single crystal tantalum below T_c, separated into electronic and phonon channels. As the normal state electrons are frozen out below T_c, their contribution to thermal conductivity is rapidly suppressed. At the same time, the phonon contribution is significantly enhanced as electron-phonon scattering is reduced and phonon mean free path is lengthened.

For a nodal superconductor, κ_0/T is finite whether the nodes are accidental or symmetry-imposed. There is, however, a major distinction between the two. In a clean, nodal super-

conductor, the nodes are broadened by Andreev scattering by impurities producing a finite quasiparticle density of states at the Fermi level [81]. If the nodes are imposed by symmetry, it has been shown that electrical conductivity and κ_e/T can be described by a temperature independent universal expression from $T = 0$ to an energy scale associated with the impurity scattering. The temperature independence is due to the cancellation of two opposing effects as temperature increases—the increase in quasiparticle density of states and the reduction in mean free path [81, 82]. For example, in the case of the $d_{x^2-y^2}$ pairing symmetry with four line nodes, κ_0/T is given by

$$\frac{\kappa_0}{T} = \lim_{T\to 0} \frac{\kappa_e}{T} = \frac{\pi\hbar k_B^2}{3}\frac{N_f v_f^2}{\mu\Delta_0}, \tag{2.33}$$

where N_f is the density of states for both spins per unit volume at the Fermi level, v_f is the Fermi velocity at the nodes and $\mu\Delta_0$ is the slope of the gap at the nodes [76, 81]. This is known as "universal heat conduction" because it is independent of the impurity scattering rate, Γ, in the clean limit ($\hbar\Gamma \ll k_B T_c$) [82, 83]. Universal heat conduction has been observed in $YBa_2Cu_3O_{6.9}$ [75], which is widely considered as a d-wave superconductor supported by evidence from phase-sensitive experiments [84]. On the other hand, κ_0/T is strongly dependent on the impurity scattering rate for superconductors with accidental nodes. If the scattering is strong enough, the nodes could be lifted and κ_0/T goes to zero [85]. This dependence of κ_0/T on impurity scattering rate has been calculated theoretically for the scenario of the s-wave symmetry with accidental nodes in the iron-pnictide superconductors, shown in Figure 2.7 [85]. This is contrasted with the relative insensitivity of κ_0/T to Γ in $YBa_2Cu_3O_{6.9}$ and KFe_2As_2.

At low temperatures, the behaviour of κ/T as a function of temperature is very different for superconductors with different gap structures. The thermal conductivity for a fully-gapped superconductor at temperatures much lower than T_c should be almost entirely due to the lattice [79]. If the mean free path of the phonons is boundary-limited, then $\kappa/T \sim T^2$. Calculations for superconductors with symmetry-imposed nodes show that the leading-order correction to κ_e/T is also T^2 [81]. This electronic contribution could potentially be separated from the lattice contribution by their difference in magnitude. For example, in KFe_2As_2 the electronic term is approximately two orders of magnitude larger [77]. This has also been observed in $YBa_2Cu_3O_7$ [86]. Due to the lack of universality, the temperature dependence of κ_e/T in an s-wave superconductor with accidental nodes depends on details like the size

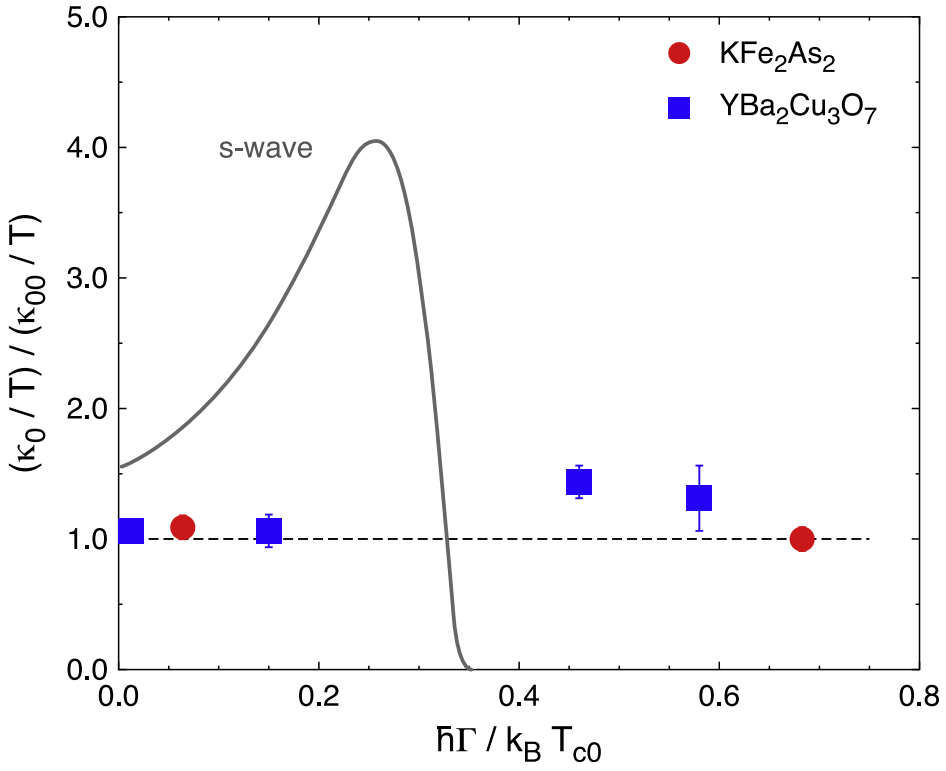

Fig. 2.7 Reproduced from [77]. The vertical axis is normalised by the calculated universal heat conduction value for a d-wave superconductor (labelled in this figure as κ_{00}/T). The horizontal axis is normalised by the superconducting transition temperature in the clean limit (T_{c0}). The black solid line is a theoretical calculation for an s-wave superconductor with accidental nodes [85] and the data points are experimental measurements. This shows that κ_0/T in materials with symmetry-imposed nodes is insensitive to the rate of impurity scattering, in contrast to the strong impurity dependence in superconductors with accidental nodes. In theory, κ_0/T measurements can be used to differentiate symmetry-imposed and accidental nodes.

of the interband and intraband scattering [85]. As a reference, a T-linear temperature dependence of κ_e/T has been observed in LaFePO [87] which is suggested to have accidental nodes.

The application of magnetic field yields an increase in quasiparticle density of states at the Fermi level and results in an increase of electronic thermal conductivity. In a fully-gapped superconductor, these states are confined within vortex cores and have to tunnel between vortices to contribute to thermal conductivity perpendicular to the field. This results in a superlinear field dependence of enhancement, as seen in the case of Nb [88]. In the case of nodal superconductors, the energy of the quasiparticles near the nodal region is Doppler shifted by the local superfluid velocity. This is the Volovik effect [89] and it results in a $\sqrt{H}$ dependence of κ_e/T which dominates at low fields. The quasiparticle energy is also shifted by the Zeeman effect and the nodal regions are broadened into spin-polarised pockets. This effect contributes a linear dependence on the magnetic field of κ_e/T if coupling of the field to orbital motion is ignored [90].

The measurable differences in thermal conductivity (value of κ_0/T, κ/T as a function of T, κ_0/T as a function of H) resulting from different superconducting gap structures are summarised in Table 2.1.

2.5.2 Thermal conductivity measurement

We use the standard one-heater–two-thermometer setup [86, 91, 92] to measure thermal conductivity, and a photograph of the measurement stage is shown in Figure 2.8. This setup was used to measure the $(Ca_xSr_{1-x})_3Rh_4Sn_{13}$ (Chapter 4), YFe_2Ge_2 (Chapter 5) and SmB_6 (Appendix A) samples. The heater and thermometers are electrically connected via resistive $Pt_{0.92}W_{0.08}$ wires which are coiled up to increase their lengths. $Pt_{0.92}W_{0.08}$ wires are used because their thermal and electrical resistances are in suitable ranges where they provide sufficient thermal isolation without overwhelming electrical resistance. The thermometers are measured with the standard 4-point geometry and the heater is connected to two wires. The heater and thermometers are also mechanically supported by thin Kapton tape. The wires and Kapton tape are mechanically anchored to plastic scaffolds which are in turn mounted on a brass stage.

The heater is controlled by a Keithley 2410 SourceMeter, set to voltage source mode, which measures the supplied voltage and current. The resistance of the heater is about 5400 Ω at

	Nodeless gap	Accidental nodes	Symmetry-imposed nodes
κ_0/T	0	Depends on impurities	Universal (in clean limit)
κ/T as a function of T	bT^2 (phonon)	Depends on system	$a+bT^2$ (electronic)
κ_0/T as a function of H	Superlinear	$\sqrt{H}$ followed by H-linear	$\sqrt{H}$ followed by H-linear
Examples	Nb [88], $NbSe_2$ [78], Ta [79]	LaFePO [87] KFe_2As_2 [26, 27]	$YBa_2Cu_3O_{6.9}$ [75]

Table 2.1 A summary of the gap structures that could be differentiated by thermal conductivity [77]. Symbols a and b are constants. In certain materials like LaFePO and KFe_2As_2, strong anisotropic modulation of an s-wave gap structure can result in a sign change of the gap at certain angles (c.f. G2 in Figure 2.5). This creates accidental nodes. In contrast, symmetry-imposed nodes exist by virtue of the symmetry of the gap structure. For example, a gap structure with the symmetry $d_{x^2-y^2}$ will have nodes along the lines $y = \pm x$. For a nodeless gap, the temperature dependence of κ/T at very low temperatures is due to phonons. In the boundary scattering regime, $\kappa/T \sim T^2$. For symmetry-imposed nodes with the leading order correction, $\kappa/T \sim a+bT^2$. The temperature dependence of κ/T of accidental nodes depends on the details of the system. The field dependence of κ_0/T applies for fields larger than H_{c1} when the system is in the vortex state.

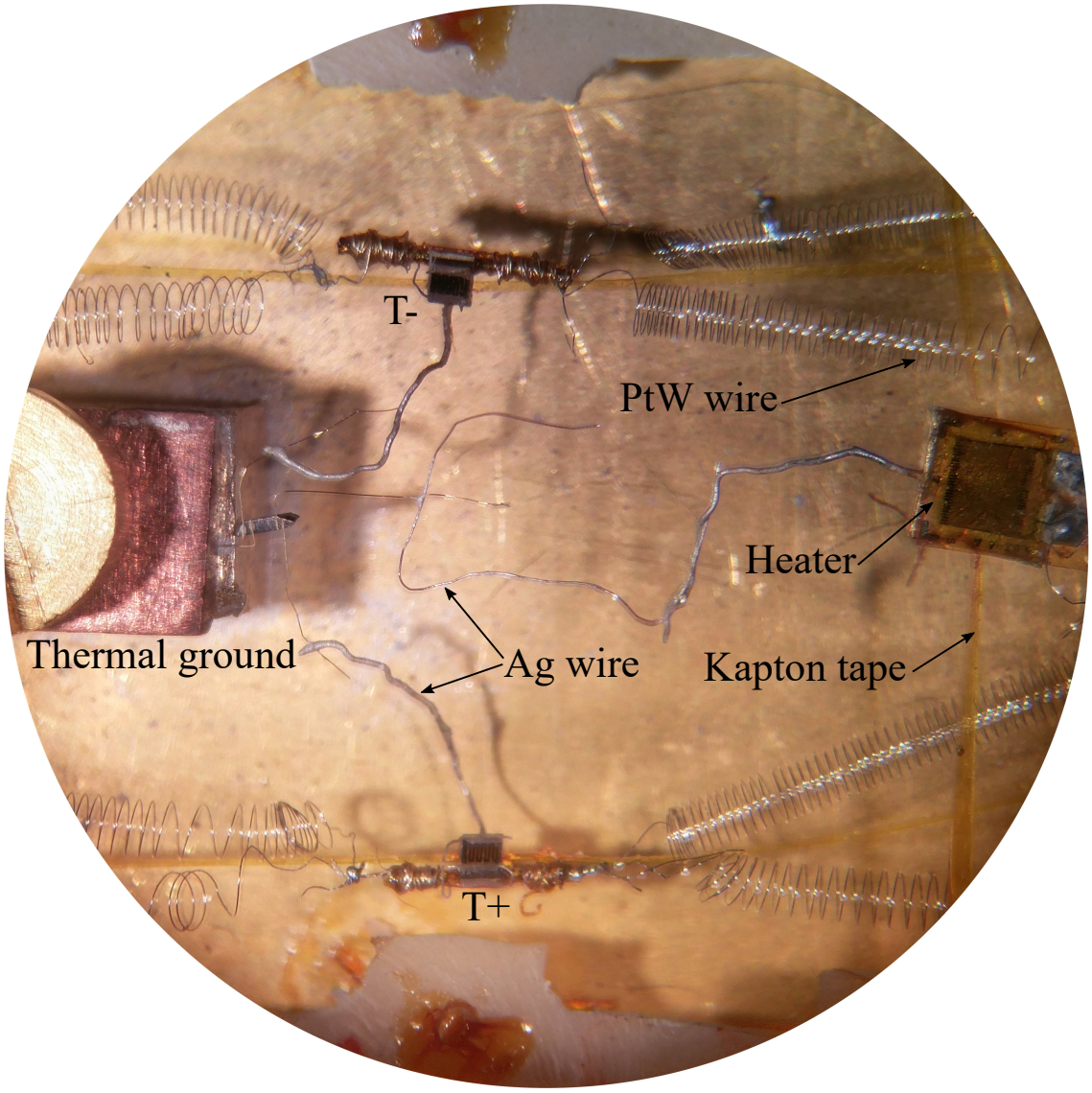

Fig. 2.8 A photograph showing the thermal conductivity measurement stage with a conventional one-heater–two-thermometer measurement setup.

low temperatures and the resistance of the probe wiring is about 40 Ω. The thermometer T_+ (T_-) is attached to the hotter (colder) end of the sample. These are Cernox CX-1030 thermometers from Lake Shore and they are measured with LIAs with the excitation currents provided by current sources modulated with the voltage output of the LIAs, much like the technique for measuring resistivity described in Section 2.4.1. Since the resistances of the thermometers are high (of order kΩ at low temperatures), no pre-amplification is necessary. Care has been taken to ensure that self-heating of the thermometers is minimised: the excitation current is chosen such that the maximum power dissipated in the thermometers is about 10 pW. This is three orders of magnitude smaller than the minimum heater power for a typical sample, which is about 10 nW.

Thermal conductivity in an isotropic sample with uniform cross-sectional area A is given by

$$\begin{aligned} \kappa &= -\frac{\dot{Q}}{A\nabla T} \\ &\simeq \frac{\dot{Q}}{A(T_+ - T_-)/L} \\ &= \frac{\dot{Q}}{g(T_+ - T_-)}, \end{aligned} \tag{2.34}$$

where L is the distance between its T_+ and T_- contacts, $g = A/L$ is the geometric factor of the sample and $\dot{Q}$ is the heater current. This approximation assumes that the temperature gradient is small. The typical temperature gradient is about 5–15% of the average temperature of the sample, which is taken to be the average of T_+ and T_-. Since we are measuring small temperature differences and the reproducibility of a Cernox thermometer is about ±3 mK at 4.2 K [93], these thermometers are calibrated in situ against a third thermometer (also a Cernox CX-1030) located on the same measurement stage. Calibration is done with the heater switched off and the temperatures of the T_+ and T_- thermometers are allowed to equilibrate with the thermal ground through the sample. This calibration procedure does not change the uncertainty in absolute temperature but greatly improves the measurement of the temperature gradient in the sample.

Two different methods of measuring thermal conductivity are used in our work. The first is the steady-state method, where the temperature of the stage and heater power are set to a fixed setpoint and the temperatures of the T_+ and T_- thermometers are given time to

reach a stable value. After that, the temperatures and heater power values are averaged for about 5 mins to account for small drifts. This technique is very simple and reliable but is quite slow. Each data point takes about 10 to 30 mins, depending on the temperature. The second is the continuous sweep method. In this mode, the heater power and temperature of the sample are swept between two setpoints very slowly (about 10 to 20 mK/min) and the temperature and heater power values are recorded once a second. The temperature of the sample is varied by either changing the heater power and keeping the stage temperature constant or by changing both the heater power and the stage temperature. The advantage of the continuous sweep method is its much higher data acquisition rate which allows the measurement of fine features in thermal conductivity. The results of this method are always checked against the steady-state method to ensure their reliability.

Equation 2.34 assumes that all the heat current from the heater passes through the sample. In practice, while the design of the setup aims to minimise this, there will be some heat leak through the frame (via the PtW wires and the Kapton tape), residual gas and radiation. We will now estimate the magnitude of these heat loss channels when the sample is at 1 K, and compare that with the typical heater power used.

First, we will examine the alternative heat conductive path through the frame via the 10 PtW wire segments and 6 Kapton tape segments (see Figure 2.8). The length of PtW wires used is estimated from the circumference of coils multiplied by the average number of turns. The approximate, combined geometric factor of the PtW wire segments in μm is

$$\begin{aligned} g_{\mathrm{PtW}} &\simeq \underbrace{10}_{\text{no. of segments}} \times \underbrace{\pi \times 12.5^2}_{\text{cross-sectional area of wire}} / (\pi \times \underbrace{1100}_{\text{diameter of coil}} \times \underbrace{44}_{\text{no. of turns in coil}}) \\ &= 0.032\ \mu\mathrm{m}. \end{aligned} \tag{2.35}$$

A similar calculation for the geometric factor of the Kapton tape yields

$$\begin{aligned} g_{\mathrm{Kapton}} &\simeq \underbrace{6}_{\text{no. of segments}} \times \underbrace{210}_{\text{width}} \times \underbrace{25}_{\text{thickness}} / \underbrace{14500}_{\text{length}} \\ &= 2.2\ \mu\mathrm{m}. \end{aligned} \tag{2.36}$$

The thermal conductivities of $Pt_{0.92}W_{0.08}$ and Kapton at 1 K are about 0.33 W/m K (from our measurements) and 5.24×10^{-3} W/m K [94] respectively, so the combined thermal conductance of the PtW wires and Kapton tape is approximately 2.2×10^{-8} W/K. For a maximum temperature difference of 0.7 K when the sample is at 1 K and the stage is at 0.3 K, the heat leak is about $\dot{Q}_{\text{frame}} = -1.5\times10^{-8}$ W. The sign is chosen to show that the heat transfer will reduce the magnitude of the temperature gradient in the sample.

Another source of heat leak is due to the residual helium exchange gas. However, in this case, only the heat leak to the heater will affect the thermal conductivity results as heat leak to the sample and thermometers should not change the temperature gradient (the same is true for radiative heat leak discussed below). Under usual operation, we use a turbomolecular pump to remove all helium exchange gas introduced during the cooldown process. The vacuum gauge attached to the pump reads its pressure floor of 0.1 mTorr, but the typical pressure in the inner vacuum chamber (IVC) should be of the order 10^{-6} mbar [95]. The heat leak due to helium in the regime where the mean free path is comparable to the physical dimensions of the IVC is given by [95]

$$\dot{Q}_{\text{gas}} \simeq 0.02aAP\Delta T, \tag{2.37}$$

where a is the dimensionless "accommodation coefficient" which ranges from 0.02 to 1, A is the area of surface exposed to helium gas in cm^2, P is the gas pressure in mbar and ΔT is the temperature difference in K. Assuming the sample (and heater and thermometers) is at 1 K and the IVC walls are at 4.2 K, the heat leak due to residual helium gas for $a = 1$, A =0.06 cm^2 (area of the heater), $P = 10^{-6}$ mbar and ΔT =3.2 K, is $\dot{Q}_{\text{gas}} = 3.8\times10^{-9}$ W.

The heat leak due to radiation, for emissivities of unity, is given by the Stefan-Boltzmann equation [95]

$$\dot{Q}_{\text{radiation}} = 5.67\times10^{-12}A(T_{\text{IVC}}^4 - T_{\text{sample}}^4). \tag{2.38}$$

Hence, the heat leak for the same exposed area A =0.06 cm^2, T_{IVC} =4.2 K and T_{sample} =1 K is $\dot{Q}_{\text{radiation}} = 1.1\times10^{-10}$ W.

The typical heater power used when the sample is at 1 K is about $\sim 10^{-5}$–10^{-6} W, depending on the thermal conductance of the sample. Compared to the heat leak channels $\dot{Q}_{\text{frame}}$,

$\dot{Q}_{\text{gas}}$ and $\dot{Q}_{\text{radiation}}$, this is about 2–3 orders of magnitude greater. Also, note that the directions of heat leak for $\dot{Q}_{\text{frame}}$ and $\dot{Q}_{\text{gas}}$ are opposite, so the total heat leak could potentially be even smaller. This justifies our decision to ignore the effects of heat leaks.

The reliability of our experimental setup can be verified by several sources. Firstly, we have measured a piece of silver wire and checked that its thermal conductivity agrees well with WFL. Next, our measurement of a sample of YFe_2Ge_2 matches closely with an independent thermal conductivity measurement on the same sample performed by our collaborators at the University of Waterloo (see Figure 5.9). Finally, our measurement of a sample of SmB_6 also agrees well with a measurement done by Sera et al. [96] (see Appendix A).

2.6 Fridge LabVIEW Interface (Flint)

In a typical experiment, the computer needs to interface with several instruments simultaneously to control the experimental settings and to acquire data. The traditional approach of writing specialised software for a single type of experiment has worked well in the past but is unnecessarily rigid. For example, the Big Fridge in the Quantum Matter group was controlled by a custom written C program called GOWI, which was designed for and excelled at controlling quantum oscillations experiments. However, it would be impossible to use GOWI to run a thermal conductivity experiment, which uses a very similar set of instruments, without tedious and time-consuming modifications to the source code.

We have recently written a new set of control software using LabVIEW, called Fridge LabVIEW Interface (Flint). The main purpose of Flint is to have one software package handle a variety of different types of experiments. Flint is designed to interface with a dynamically set number of instruments. It is also highly modular such that it can be easily extended to run other types of experiments. This is largely achieved by making use of the LabVIEW Object-Oriented Programming (LVOOP) paradigm [97]. Many parts of Flint are structured as objects so as to be as general as possible. Currently, it is a collection of more than 300 VIs that is broadly divided into four layers.

1. *User interface layer.* This is the top layer that the operator directly accesses. The functionalities of this layer include defining instruments involved and their purpose (`Setup experiment.vi`), scheduling and execution of jobs (`Job Control.vi`) and live display and basic analysis of acquired data (`Plotter.vi`).

2. *Server layer.* Similar to GOWI, Flint has a layer of server VIs. A server VI is meant to run continuously in the background and it is typically associated with a control parameter (temperature, magnetic field, rotation angle) or a type of experiment (thermal conductivity, ad hoc). All changes in control parameters are applied through server VIs. So far, there are five server VIs in Flint: Field, Temperature, Rotation, Thermal conductivity and Ad hoc, although more can be easily written for and integrated into Flint.

3. *Sample layer.* A "sample" in Flint is a LabVIEW object that measures and/or controls a physical quantity. For example, a Standard sample can be assigned to measure resistance, and a Temperature sample can control and measure temperature. The purpose of this layer will be elaborated below.

4. *Instrument layer.* Each instrument is also represented by a LabVIEW object and it uses protected methods in its class to communicate with the instrument. Here, we can see the advantage of using LVOOP. By creating VIs with dynamic dispatch input and output terminals and giving them the same name, say, `Instrument Query Data.vi`, we can request data from an instrument in a general way, and only define which exact instrument to be used at runtime (with `Setup experiment.vi`). In this way, it is possible to call `Instrument Query Data.vi` with a LIA object or resistance bridge object and receive the logical, relevant response from each instrument.

The main challenge to an implementation of a dynamic control software like Flint is the many-to-many relationship between instruments and physical quantities. For example, let us consider the control and measurement of magnetic field when running the Big Fridge. The control of the field is handled by a DC power supply but the read-back of the field value is done by reading the voltage across a shunt resistor with a digital multimeter (DMM). While these are two individual instruments, they can be more easily manipulated if they were bundled into one object. This is the purpose of the sample layer in Flint. A field sample object, which interfaces with both the power supply and the DMM, can be used to control and read back the field value. Similarly, a thermal conductivity sample object communicates with four instruments—a temperature controller, two LIAs and a heater supply—in order to produce a meaningful measurement.

In the previous examples, two or more instruments are operated coherently by one sample object to control and/or measure one physical quantity. The converse is also true. An

instrument like the Lake Shore LS340 temperature controller can measure up to 4 channels simultaneously. In the Flint framework, this will correspond to 4 different sample objects because each of them is a physical quantity. The many-to-many relationship is illustrated in Figure 2.9 for a typical thermal conductivity experiment.

Flint permits a high level of extensibility and reusability. Suppose we want to use a new instrument to run the same experiment. We just have to create a new instrument class to communicate with said instrument. No modifications to the other layers above are needed. Similarly, if we want to run a new type of experiment (say, heat capacity) using existing instruments, we only need to write a new server and a new sample class specific to the new experiment. The layer above (User interface layer) and below (Instrument layer) remain unchanged.

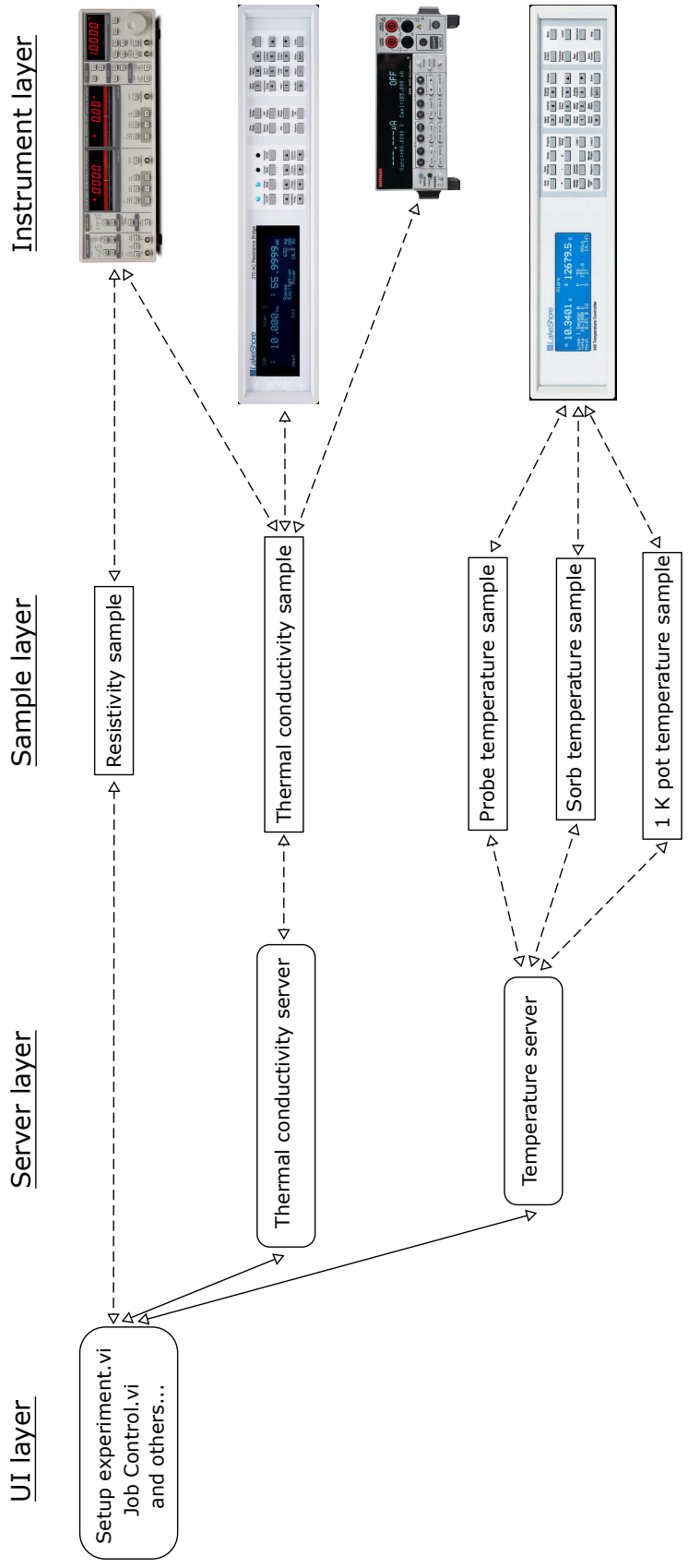

Fig. 2.9 Illustration of the interactions between VIs and objects from the four layers in Flint for a typical experiment. The many-to-many relationship between instrument and data is reflected by the relationship between sample and instrument objects. The dashed lines refer to dynamic relationships defined at runtime using the `Setup experiment.vi`. Pictures of the front panels of the instruments are taken from their respective manufacturers.

Chapter 3

$Sr_3Ir_4Sn_{13}$ quantum oscillations

3.1 Introduction

$A_3T_4Sn_{13}$ is a family of cubic superconductors with moderate T_c's between 4 and 8 K that has recently regained the attention and interest of the quantum materials research community. First discovered and characterised in the 1980s [98–101], it became an active topic of research after Yang et al. found anomalous, peak-like features in $Ca_3Ir_4Sn_{13}$ in the magnetic susceptibility and electrical resistivity at around 45 K. On the basis that no anomaly is observed in heat capacity, this feature was erroneously attributed to ferromagnetic spin fluctuations [102]. However, direct X-ray diffraction experiments done on $Sr_3Ir_4Sn_{13}$ by Klintberg et al. [16] proved conclusively that the feature is due to an antiferroic structural phase transition, brought about by freezing in distortions in the Sn icosahedra. As mentioned in Section 2.2, this type of structural transition is also known as a unit-cell combining phase transition as the distortions in one unit cell are mirrored by opposite distortions in neighbouring cells. By applying physical pressure and chemical pressure through substitution of Sr by Ca, Klintberg et al. showed that the structural phase transition temperature T^* could be tuned to zero. At the structural transition, the Fermi surface reconstructs and this results in a loss of itinerant charge carriers which is reflected as a spike in resistivity and a dip in Pauli susceptibility [16].

The details of this structural transition are contentious. The interpretation by Klintberg et al. is that the transition is described by three perpendicular phonon modes at the M point (see Figure 3.1). These symmetry equivalent modes have wavevectors $\mathbf{q} = (0.5, 0.5, 0)$, (0.5,

0, 0.5) and (0, 0.5, 0.5) [16, 103], and the modes go soft at the transition temperature, T^* (cf. Section 2.2.1). Wavevectors $\mathbf{q}$ are in units of the reciprocal lattice vector $(2\pi/a)$ of the high-temperature I phase, where a =9.7968 Å [16] is the I phase lattice constant. Below T^*, the average static atomic displacements associated with the soft modes become finite and new Bragg reflection positions appear. This leads to doubling of the unit cell in all three dimensions which results in a body-centred cubic lattice ($I\bar{4}3d$) with lattice constants that are twice that of the I phase [16]. We will show, using our quantum oscillations results, that this interpretation is correct.

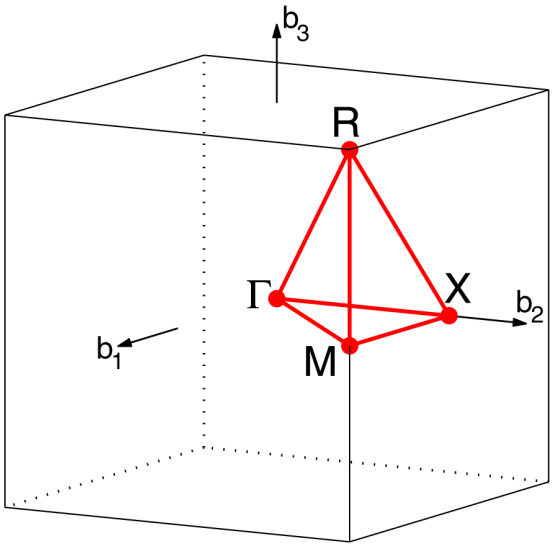

Fig. 3.1 Reproduced from [104]. The Brillouin zone of a simple cubic crystal like the I phase of the $A_3T_4Sn_{13}$ family. The high symmetry points are labelled.

While most recent studies agree that the high-temperature (I phase) crystal structure, shown in Figure 3.2, belongs to the space group $Pm\bar{3}n$, there is disagreement among several diffraction experiments on the exact crystal structure of the low-temperature I' phase. Hodeau et al., based on evidence from electron and X-ray diffraction data, concluded that the I' phase belongs to either the bcc space group $I2_13$ or the tetragonal $P4_222$ with three individual twinned domains, and this result was agreed by Miraglia et al. [98, 105]. Bordet et al. performed powder X-ray experiments and concluded that the I' phase belongs to the space group $I4_132$ [106]. Mazzone et al., on the other hand, proposed two possibilities after measuring single crystal X-ray diffraction (XRD) of $Ca_3Ir_4Sn_{13}$: either an I-centred cubic unit cell or a scenario of merohedral twinning consisting of three tetragonal domains [22], similar to the conclusions of Hodeau et al..

So far, most works on the $A_3T_4Sn_{13}$ system agree that the structural transition is second order

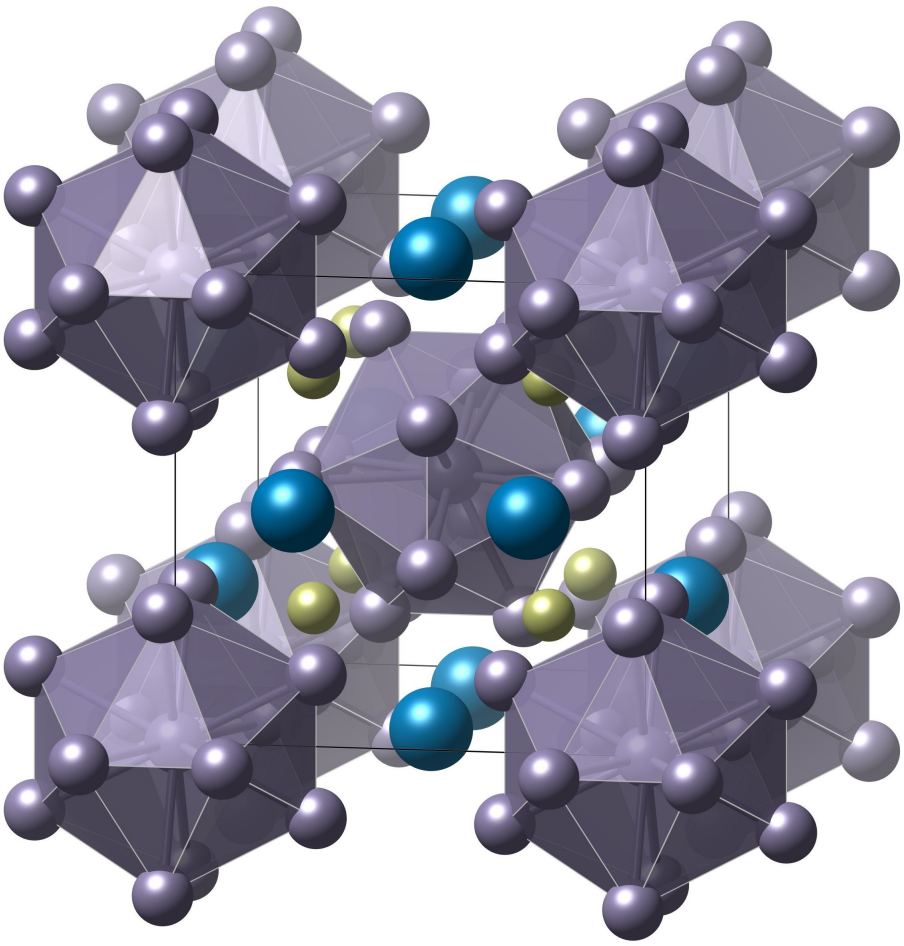

Fig. 3.2 The high-temperature crystal structure (I phase) of $Sr_3Ir_4Sn_{13}$ which is representative of the $A_3T_4Sn_{13}$ family. The Sr, Ir and Sn are represented by cyan, olive and lavender coloured spheres respectively. As mentioned in Chapter 1, the crystal structure of $A_3T_4Sn_{13}$ is closely related to that of the perovskites. We can rewrite $A_3T_4Sn_{13}$ as $(Sn1)A_3T_4(Sn2)_{12}$, where Sn1 and Sn2 are tin atoms at the centre and corners of the tin icosahedra respectively. This is very similar to the triple perovskite structure with the general formula of $A'A''_3B_4X_{12}$. The triple perovskite structure can be derived from the perovskite structure, with the general formula ABX_3, via tilting of the BX_6 octahedra [21].

in nature. Evidence for this could be seen from measurements of Klintberg et al. where the difference of the Sn1-Sn2 bond distances splits continuously from zero as a function of temperature from T^* [16]. This was confirmed by Mazzone et al. when they found that the XRD peak intensity associated with the I' phase superstructure increases linearly with $T^* - T$, which indicates a second order phase transition with mean-field critical exponents [22]. This is also consistent with their own inelastic neutron scattering data which probes the temperature dependence of the frequency of the soft mode and found that it approximately follows $\sqrt{T - T^*}$. Additional evidence for a second order transition was provided by Goh et al., who found that the heat capacity of $Sr_3Rh_4Sn_{13}$ shows a lambda-like, hysteresis-free temperature dependence at T^* [18].

There is also strong evidence that the superconductivity in the $A_3T_4Sn_{13}$ material family is fully-gapped and has an *s*-wave pairing symmetry. This can be seen from the thermal conductivity (κ) data of Zhou et al. who measured the temperature and field dependence of κ/T of $Ca_3Ir_4Sn_{13}$. In zero field, they showed that κ/T is virtually zero, suggesting the absence of nodes in the superconducting gap. In field, κ/T increases slowly with field, resembling the dirty limit *s*-wave alloy InBi [19]. Further hints of an isotropic, nodeless gap come from the measurement of the field enhancement of the Sommerfeld coefficient, by Wang et al., which is essentially linear in field [107]. In addition, the electronic heat capacity of $(Ca_xSr_{1-x})_3Rh_4Sn_{13}$ in the superconducting state measured by Yu et al. [20] can be fitted to a single isotropic gap. Similarly, C/T in $Ca_3Rh_4Sn_{13}$ measured by Ślebarski et al. [108] is negligible at zero field at 0.4 K, and increases linearly with field. Finally, this is all consistent with our own thermal conductivity measurements which will be discussed in Chapter 4.

Given the *s*-wave pairing symmetry, it is likely that the superconductivity is driven by electron-phonon interactions. Having mistakenly identified the feature at T^* to be ferromagnetic fluctuations, Yang et al. understandably suggested that the superconductivity in these materials are related to these fluctuations [102]. However, there is little evidence from other groups to support this idea. Sarkar et al. has performed ^{119}Sn nuclear magnetic resonance (NMR) experiments on $Ca_3Ir_4Sn_{13}$ and found that the Knight shift drops significantly below T_c. Since the Knight shift correlates with local static magnetic susceptibility and a spin singlet superconductor will have a decrease in Knight shift below T_c, this provides strong evidence for spin-singlet superconductivity in $Ca_3Ir_4Sn_{13}$ [109]. This contradicts the pairing via ferromagnetic fluctuations picture which should have spin-triplet superconductivity.

From the evidence that we have seen so far, the $A_3T_4Sn_{13}$ is a family of electron-phonon driven superconductors with a second order structural transition. This structural transition can be easily tuned with physical pressure and chemical substitution, as we can see from the phase diagrams of $(Ca_xSr_{1-x})_3Ir_4Sn_{13}$ and $(Ca_xSr_{1-x})_3Rh_4Sn_{13}$ reproduced in Figure 3.3 from [16, 18]. Furthermore, powder x-ray diffraction studies of $(Ca_xSr_{1-x})_3Rh_4Sn_{13}$ (Supplemental Material of [18], reproduced in Figure 4.6) have demonstrated that the substitution of Sr by Ca results in a reduction of the lattice constant which is linearly proportional to the substitution fraction. This suggests that in the $A_3T_4Sn_{13}$ system, the empirical Vegard's law [110] is obeyed and chemical substitution is equivalent to applying physical pressure. Hence, this is also referred to as chemical pressure. From the linear extrapolation of T^* to zero in the phase diagram of $(Ca_xSr_{1-x})_3Rh_4Sn_{13}$, critical substitution fraction $x_c \sim 0.9$ [18].

With application of chemical and hydrostatic pressure, T^* can be suppressed to zero. Interestingly, T_c is enhanced at the same time, and peaks near the quantum critical point. Further increase in pressure proves to be detrimental to superconductivity, and T_c decreases. In the Eliashberg-McMillan framework, the softening of part of the phonon spectrum increases the electron-phonon coupling constant λ [111] (cf. Section 2.4). This is consistent with experimental findings from [20, 102, 112, 113] where the values of $2\Delta/k_BT_c$ and $\Delta C/\gamma T_c$ measured were much larger than the expected BCS values (Δ, ΔC and γ are the superconducting gap, jump in specific heat at T_c and Sommerfeld coefficient respectively). Yu et al. in particular tracked the changes in $2\Delta/k_BT_c$ and $\Delta C/\gamma T_c$ across the phase diagram and found that these values increase from BCS limits to strong coupling values as the tuning parameter x goes from 0 to 0.95 [20].

The structural transition in the $A_3T_4Sn_{13}$ material system is often discussed in the literature as a charge density wave (CDW) transition [114–116], which is based on Peierls instability in one-dimensional materials. A material with a CDW transition should have significant nesting of the Fermi surface resulting in a peak in the real part of the bare electronic susceptibility at the transition wavevector [117]. However, as it was discussed by Johannes and Mazin [117], the predictive power of looking only at electronic instability through Fermi surface nesting is poor. In fact, for $Sr_3Ir_4Sn_{13}$, there is a peak in the electronic susceptibility but at the wrong wavevector of $\mathbf{q} = (0.5, 0.5, 0.5)$ [16]. Hence, while the electronic instability may contribute to this phase transition, it is far from the dominant mechanism. Therefore, we believe that the phase transition in the $A_3T_4Sn_{13}$ system is better described as a lattice instability.

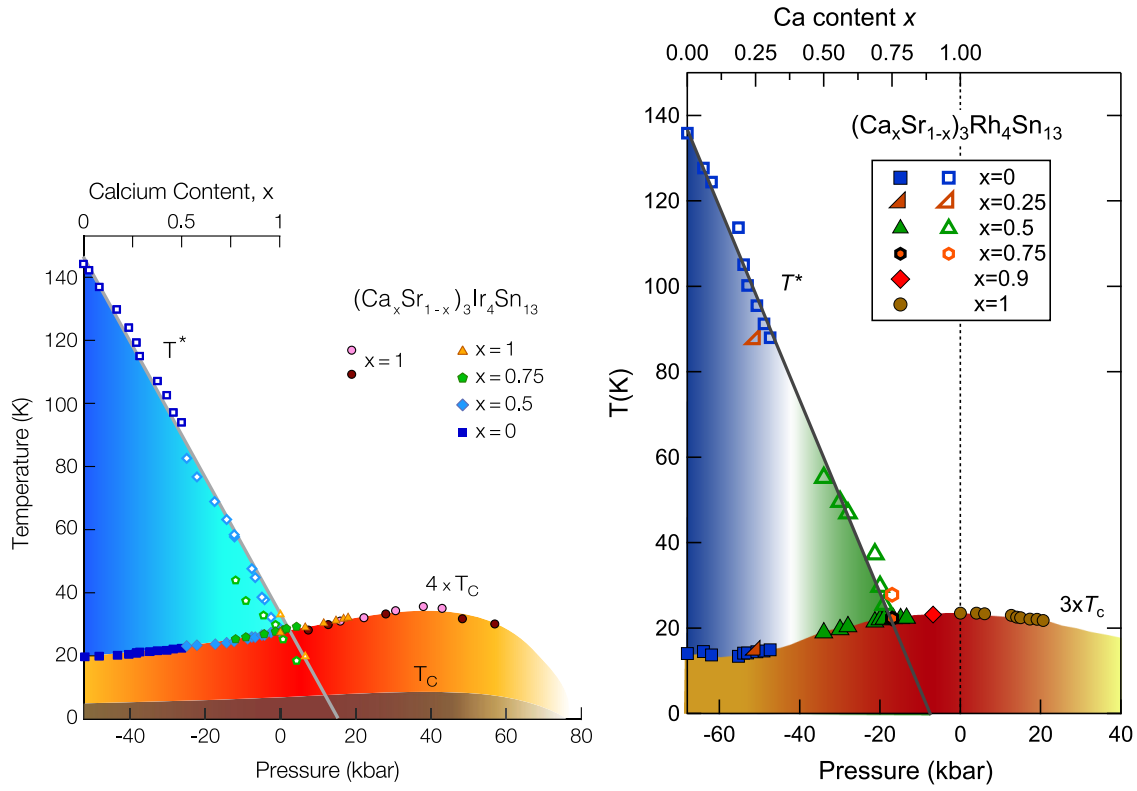

Fig. 3.3 Phase diagrams of $(Ca_xSr_{1-x})_3Ir_4Sn_{13}$ and $(Ca_xSr_{1-x})_3Rh_4Sn_{13}$ by tuning physical and chemical pressure, reproduced from [16, 18] respectively.

3.1.1 Motivation

As alluded to earlier, there is some ambiguity from diffraction experiments as to the structure of the I' phase. In particular, it is difficult for XRD to differentiate between the bcc lattice and three orthogonal merohedrally twinned tetragonal domains. Measuring quantum oscillations is one effective way of resolving these two structures. In Section 2.4, we have discussed how scattering could drastically reduce the oscillation amplitude by the Dingle factor. Hence, the fact that quantum oscillations could be at all observed is a strong argument against the merohedral twinning argument. Moreover, the Fermi surfaces and quantum oscillation frequencies are very different for the different structures. By matching experimentally observed frequencies to DFT calculations for different possible structures, we could pin down the crystal structure of the I' phase. Another insight we could gain from this measurement is the nature of the superconductivity. The $A_3T_4Sn_{13}$ family is unique because of the coexistence of the structural transition and superconductivity, and we are interested in finding out whether the associated soft phonon mode enhances electron-phonon coupling which will, in turn, increase the effective mass of the quasiparticles.

3.2 Quantum oscillation measurement

We have measured the Shubnikov-de Haas (SdH) quantum oscillations of a $Sr_3Ir_4Sn_{13}$ sample as a function of angle and temperature. While the experimental data has been presented in my MPhil dissertation titled "Experimental determination of Fermi surface of superconductors $Sr_3Ir_4Sn_{13}$ and $TlNi_2Se_2$", the data analysis and interpretation have been significantly modified in light of new DFT calculations which have been conducted as part of my PhD. Also, I will be referring extensively to the recent publication [118] which contains much of the results presented in this chapter.

The sample is a small single crystal grown by a self-flux method [102]. The contacts were made in a 4-point geometry with DuPont 6838 silver epoxy by Lina Klintberg. In order to determine the orientation of the crystal, single crystal X-ray diffraction was performed by Monika Gamza at Royal Holloway, using an Xcalibur E Single Crystal Diffractometer from Oxford Diffraction. Due to the lack of natural faces of the sample and the cubic structure, the alignment error is estimated to be about 5°. The dimensions of the sample are approximately $0.8 \times 0.32 \times 0.1$ mm.

The voltage contacts of the sample were connected to the 1:300 turn ratio low-temperature transformer which was kept at around 1 K during the measurement. At room temperature, the signal is further amplified by a low noise pre-amplifier before being fed into a lock-in amplifier (LIA). This setup, described in Section 2.4.1, allows the resistance of the sample to be measured with very high precision. This enables us to measure the SdH effect—the tiny oscillation of the resistivity of the sample as a function of magnetic field.

We rotate the sample about one axis to change the relative angle ϕ between one of the three crystallographic axes of the crystal and the magnetic field, shown in Figure 3.4. Since the quantum oscillation frequency is proportional to the extremal Fermi surface cross-sectional area perpendicular to the magnetic field, by varying ϕ, we can obtain strict constraints on the geometry of the Fermi surface. The temperature is maintained at around 170 mK.

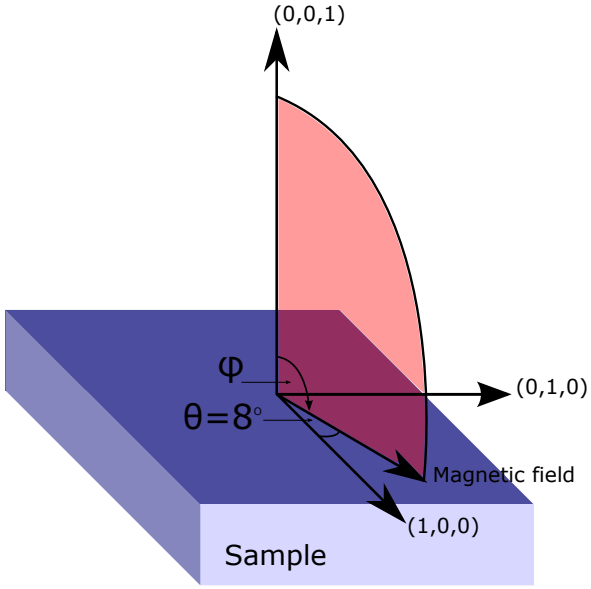

Fig. 3.4 Orientation of the $Sr_3Ir_4Sn_{13}$ sample relative to the magnetic field.

We have also varied the temperature of the sample to measure the effective quasiparticle mass. With a heater and appropriate PID settings, temperature fluctuations can be controlled to about 1 mK. As seen in the Lifshitz–Kosevich (LK) formula, increasing temperature has the effect of suppressing quantum oscillations (cf. Section 2.4). From Equation 2.19, the reduction factor due to temperature is $R_T = x/\sinh x$, where $x \propto Tm^*/B$. By measuring the relative amplitudes of quantum oscillations at different temperatures, we can find the effective mass m^*. An angle ϕ of 42° is used for the mass study.

We will outline the measurement procedures. Once the LIA signal has stabilised, the mag-

netic field is swept between 8 T to 18 T, at an approximate rate of 0.06 T/min. This field sweep is repeated for a range of angles and temperatures. The analysis of the data is carried out as such:

1. A 3rd order polynomial background is subtracted from the raw data.
2. A Fourier transform is performed to obtain frequency peaks. Our definition of a peak in the Fourier transform is a local maximum that is more than 2 standard deviations from the mean.
3. For the rotation study, the frequency positions of the peaks are plotted against rotation angle ϕ.
4. For the mass study, the amplitude of each frequency is fitted to R_T, and the effective masses extracted.

We can obtain the mean free path of the electrons by fitting the LK formula to the data after background subtraction. The frequency positions of peaks from the Fourier transform are fed into a built-in MATLAB nonlinear least-square minimisation function (which uses the Trust-Region-Reflective algorithm) as the starting parameter. From this, we obtain the Dingle factor R_D as given in Equation 2.20, and hence the mean free path. The results will be discussed in the following section.

3.2.1 Results

The trace from a single run without averaging, after polynomial background subtraction, is shown in Figure 3.5. This was measured at 170 mK and at $\phi = 42°$. The figure also shows the result of the LK formula fit and the residual. The residual mainly contains some leftover spectral weight from the 1.35 kT frequency that the LK fit could not fully capture. This could be ascribed to slight shifts in phase in the high field region and the imperfect description of the magnetoresistance by the 3rd order polynomial in the low field region.

The Fourier transform of the same data is shown as the 170 mK plot in Figure 3.6, labelled with a few main frequencies and the associated mean free paths (from the LK fit). The same figure also shows two other selected temperatures from a mass study that consists of 11 runs

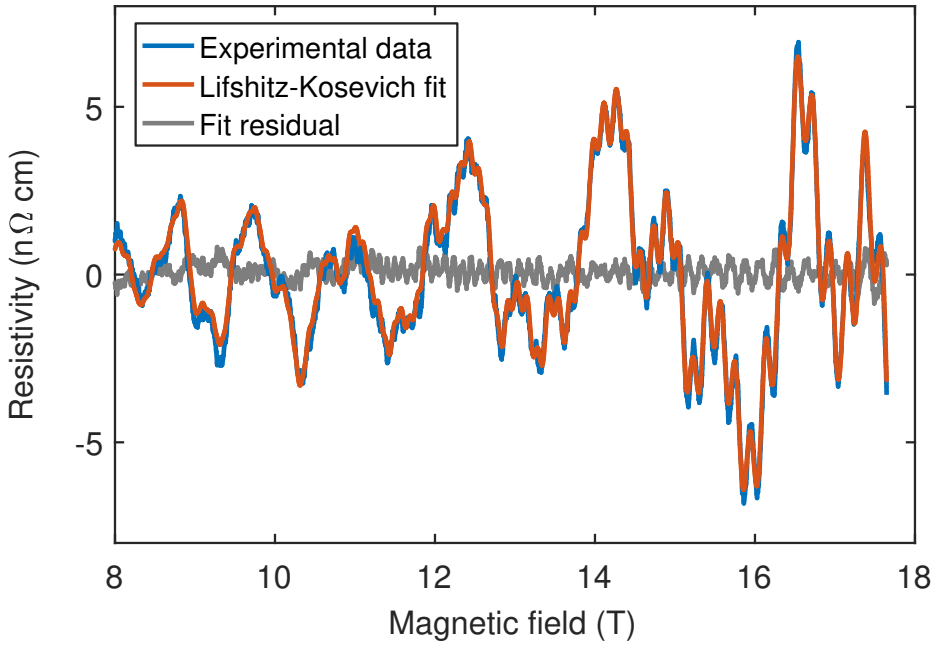

Fig. 3.5 Typical quantum oscillations data of $Sr_3Ir_4Sn_{13}$ with 3rd order polynomial background subtraction. The result of the LK fit and the residual are also shown. The frequencies included in the fit are 91 T, 209 T, 265 T, 313 T, 418 T, 644 T and 1350 T. Frequencies lower than 91 T are not included because they do not have the expected temperature dependence and are likely due to magnetoresistance background.

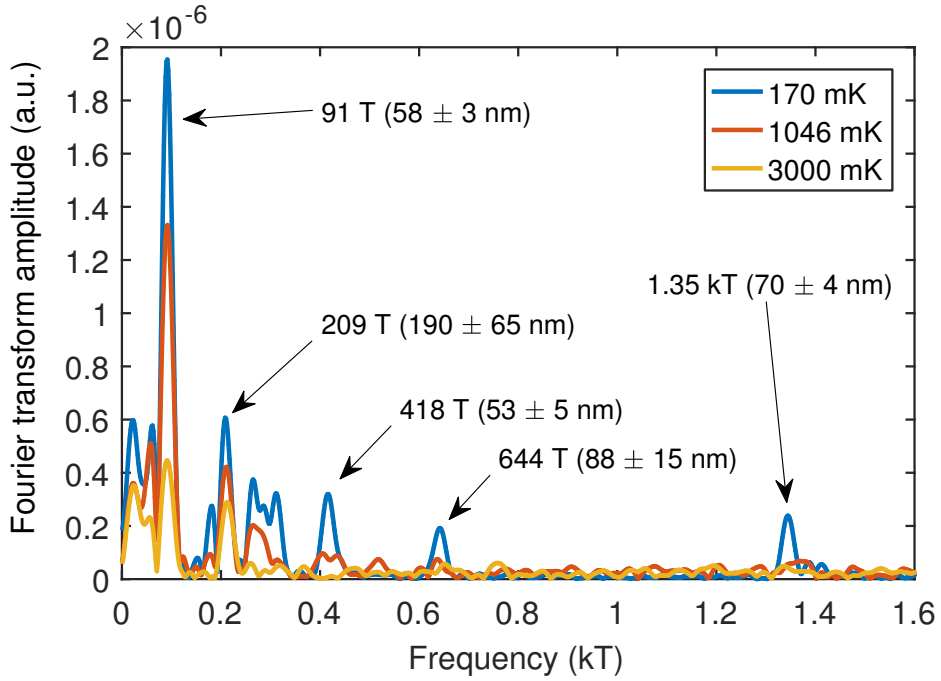

Fig. 3.6 The Fourier transform of the quantum oscillation trace of $Sr_3Ir_4Sn_{13}$ shown in Figure 3.5. A few main frequencies are labelled. Calculated mean free paths are in parentheses.

at different temperatures. The gain settings are kept the same between these runs, and the suppression of quantum oscillation amplitude is purely due to the thermal factor R_T.

The effective masses for the main frequencies extracted from the fit to Equation 2.19 are given in Table 3.1. One such fit for the 91 T frequency is presented in Figure 3.7.

The angular dependence of all the quantum oscillation frequencies, compared with predictions from density functional theory (DFT) calculations for three different crystal structures is shown in Figure 3.8. DFT calculations with the local density approximation (LDA) on the I and I' phase of $Sr_3Ir_4Sn_{13}$ have been done by David Tompsett at Imperial College using WIEN2K [119], with $Rk_{\max} = 7$ and 8000 k-points. The lattice parameters used were experimental values with optimised internal forces on atoms. For the I' phase, the energy of Band 4 has been rigidly shifted down by 13 meV. The Fermi surfaces of the four bands are shown in Figure 3.9. For the tetragonal phase, the DFT calculation was done by Wing Chi Yu at The Chinese University of Hong Kong. Since there are no experimentally measured lattice constants, this calculation was done by building a superlattice from the I phase and then allowing for structural relaxation, with 1600 k-points in the first Brillouin zone. The quantum oscillation frequencies were extracted using SKEAF [120]. There are signifi-

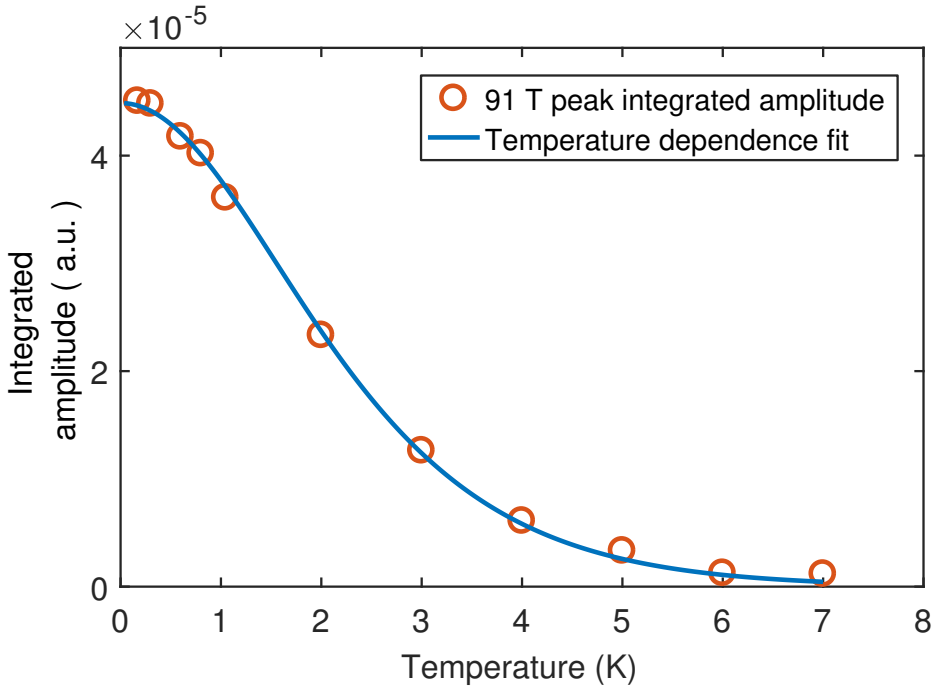

Fig. 3.7 The fit of the R_T formula to the thermal suppression of quantum oscillation amplitude of $Sr_3Ir_4Sn_{13}$ to extract the quasiparticle effective mass.

cantly more frequencies for the tetragonal phase because frequencies from three orthogonal domains are superimposed.

3.3 Discussion

We will first compare the experimental frequencies with DFT calculations of the I' phase. In Figure 3.8(b), all four bands show almost isotropic low-frequency oscillations that could explain the strong and broad signal at around 100 T. Due to the limited low-frequency resolution, we could not uniquely assign that frequency peak to any one of the bands. The maximum of Band $A_{I'}$ matches up well with the appearance of 400 T peaks around 45°. At around the same angle, Band $B_{I'}$ exhibits a plateau, which coincides with the 700 T peaks. Band $C_{I'}$ has the same curvature as the highest peaks between 1.3—1.5 kT, though the frequency is about 20% lower. There are also complex features in Band $C_{I'}$ that are not observed in the experiment.

While the agreement of the experimental frequencies with DFT calculation of the I' phase is not perfect, it is clearly a much better fit than that of the tetragonal phase. Due to the su-

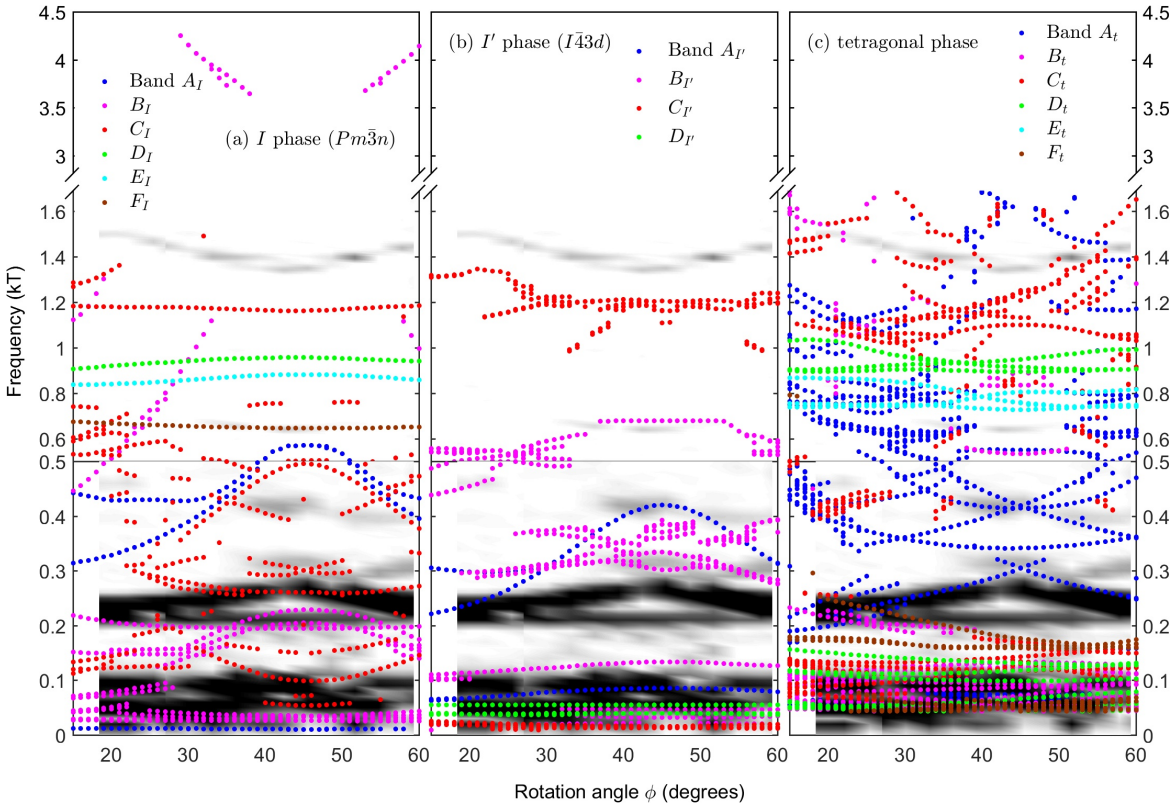

Fig. 3.8 The angular dependence of quantum oscillation frequencies of $Sr_3Ir_4Sn_{13}$ compared with DFT calculations of the (a) I phase ($Pm\bar{3}n$), (b) I' phase ($I\bar{4}3d$) and (c) tetragonal phase with merohedral twinning proposed by [22]. The experimental data is represented in grey scale. The Fourier transforms amplitudes are normalised between 0 and 1, and then the dynamic range is reduced to 0.01 to 0.3 to increase the visibility of smaller peaks. There is a break in the vertical axis between 1.6 to 3.0 kT where there are no measured or predicted frequencies. The purpose of the quantum oscillation experiment is to differentiate between the competing low-temperature phase structures in panels (b) and (c). The calculations for the high-temperature I phase in panel (a) is shown for completeness. We think that the I' phase calculation in panel (b) is the better match to the experiment because every observed frequency can be matched to frequencies from one or more bands.

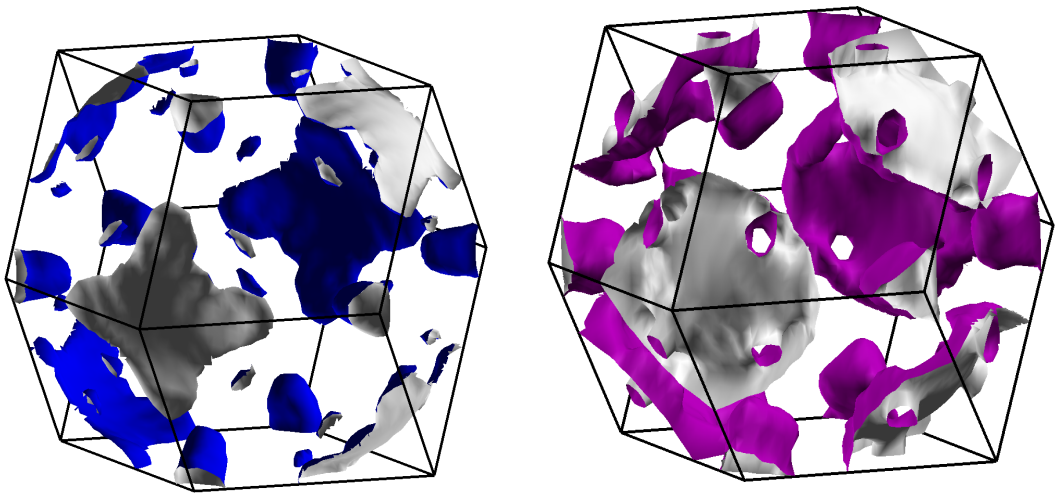

(a) Band $A_{I'}$ (b) Band $B_{I'}$

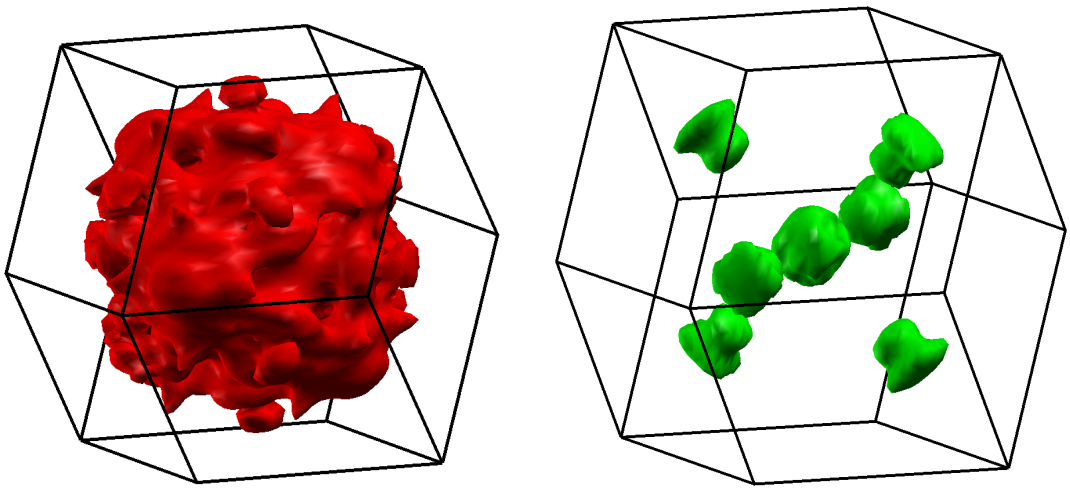

(c) Band $C_{I'}$ (d) Band $D_{I'}$

Fig. 3.9 Fermi surfaces sheets of $Sr_3Ir_4Sn_{13}$ in the low-temperature I' phase ($I\bar{4}3d$), corresponding to panel (b) of Figure 3.8.

perposition of three domains, there are many predicted frequencies between 0.8 and 1.6 kT which are not observed. Moreover, the highest observed frequency of 1.35 kT with an upward curvature is not predicted by the calculation. We can conclude from this comparison that the merohedral twinning scenario does not apply to $Sr_3Ir_4Sn_{13}$.

It is interesting to compare our quantum oscillations results to Hall resistivity measurements. In their work, Kuo et al. [121] measured a Hall signal that changed sign abruptly at the structural transition from electron-type carriers at high temperatures to hole-type at low temperatures. The low-temperature Hall resistivity is about 3.1 $\times 10^{-4}$ cm^3/C. In a naive single band picture, this will give a carrier concentration of about 2.0 $\times 10^{22}$ cm^{-3}. However, a single spherical Fermi sheet with the volume of the Brillouin zone can only support a carrier concentration of about 8.4 $\times 10^{20}$ cm^{-3}, which is a factor of 20 smaller than that suggested by the Hall signal. This problem is resolved if we consider the multiband nature of this material. Of the four bands, $A_{I'}$ and $B_{I'}$ have hole character whereas $C_{I'}$ and $D_{I'}$ have electron character. For each band, we can calculate the resistivity tensor. For example, for band $A_{I'}$ [122],

$$\boldsymbol{\rho}_A = \begin{pmatrix} \rho & -RB \\ RB & \rho \end{pmatrix}, \tag{3.1}$$

where

$$\begin{aligned} \rho &= \frac{3\pi^2\hbar}{e^2 l_0 \, k_F^2}, \\ R &= \frac{1}{ne}. \end{aligned} \tag{3.2}$$

The charge of the carrier is e and k_F is the Fermi wavevector. We estimated the average Fermi wavevectors of $A_{I'}$ and $B_{I'}$ by assuming that they fill up the entire Brillouin zone which, as we can see from Figure 3.9, is a reasonable assumption. The wavevectors of $C_{I'}$ and $D_{I'}$ are estimated using their quantum oscillation frequencies. The mean free paths are also obtained from the quantum oscillation experiment. We invert the resistivity tensor for each band to get the conductivity tensor, sum them up and invert to find the total resistivity

tensor

$$\boldsymbol{\rho} = \left(\boldsymbol{\rho}_A^{-1} + \boldsymbol{\rho}_B^{-1} + \boldsymbol{\rho}_C^{-1} + \boldsymbol{\rho}_D^{-1}\right)^{-1}. \tag{3.3}$$

The total Hall resistivity is equals to $\boldsymbol{\rho}_{2,1}/B$. For small fields, the Hall resistivity can be approximated to be independent of field. We obtained a value of 6.1 $\times 10^{-4}$ cm^3/C, which agrees within an order of magnitude with the experiment.

As shown in Table 3.1, the mass enhancements on bands $B_{I'}$ and $C_{I'}$ are modest, with the larger enhancement in band $C_{I'}$ of about 30%. If we use this band alone to estimate the electron-phonon coupling constant, we get $\lambda = m^*/m_b - 1 = 0.3$ [59, 123] (cf. Section 2.4). Compared to the electron-phonon coupling estimate of 0.983 [124] calculated from thermodynamic values and T_c, the value of λ that we have obtained from a single band is much smaller. This hints at the significant contribution from the other bands for which we do not have a one-to-one correspondence between quantum oscillation frequencies and DFT orbits. For example, assuming the 91 T frequency is mainly due to band $A_{I'}$, it will give a λ of about 0.45. This suggests that the superconductivity of $Sr_3Ir_4Sn_{13}$ might involve multiple gaps of different sizes, which is reminiscent of the phonon-mediated superconductor MgB_2 [125].

In conclusion, we have successfully observed SdH quantum oscillations in $Sr_3Ir_4Sn_{13}$ and shown that the I' phase has a body-centred cubic lattice instead of three tetragonal domains. Due to the similarities between the materials in the $A_3T_4Sn_{13}$ family, this result is likely applicable to all the $A_3T_4Sn_{13}$ materials with structural transitions. A simple multiband Hall effect calculation shows qualitative agreement with the experiment. We have also shown that the electron-phonon coupling predicted by considering only a single band is probably insufficient to explain the superconductivity in this material, which possibly involves multiple gaps.

Frequency (T)	Band (m_b/m_e)	m^*/m_e	ℓ_0 (nm)
91	$A_{I'}$ (0.553) $B_{I'}$ (1.390)	0.802 ± 0.015	58 ± 3
209	$A_{I'}$ (0.553) $B_{I'}$ (1.390)	0.469 ± 0.026	190 ± 65
418	$B_{I'}$ (1.390)	1.37 ± 0.01	53 ± 5
644	$B_{I'}$ (1.390)	1.64 ± 0.2	88 ± 15
1350	$C_{I'}$ (1.381)	1.82 ± 0.09	70 ± 4

Table 3.1 Summary of the experimentally measured orbits, the likely bands from which they originate and the mean free paths for $\phi = 42^\circ$ of $Sr_3Ir_4Sn_{13}$. The electron mass is m_e, m_b is the calculated band mass and m^* is the measured effective mass. Note that the mean free paths extracted from fitting the Dingle damping formula should be treated only as an order of magnitude estimate because there might be additional damping factors. The effective masses, in comparison, are much more reliable.

Chapter 4

$A_3T_4\mathbf{Sn}_{13}$ thermal conductivity

4.1 Introduction

In Chapter 3, we have introduced the $A_3T_4Sn_{13}$ material family and gave a detailed account of the fermiology of one particular member—$Sr_3Ir_4Sn_{13}$. The focus of that chapter was on the effects of the structural transition on the electronic structure. In this chapter, we will focus on the effects of the transition on thermal transport properties of the lattice. To this end, we have measured the thermal conductivity and heat capacity of several samples of $(Ca_xSr_{1-x})_3Rh_4Sn_{13}$ across the phase diagram shown in Figure 3.3. The substitution of Ir by Rh has the effect of applying chemical pressure and unlike $(Ca_xSr_{1-x})_3Ir_4Sn_{13}$, the critical point of $T^* = 0$ can be accessed purely by chemical substitution which allows ambient pressure measurements to be performed. However, the cost of doing so is that it is difficult to keep sample quality consistent between samples of different stoichiometry, and direct comparisons of absolute values of resistivity and thermal conductivity are in general difficult to interpret. Nonetheless, as we will see in the latter part of this chapter, we have observed significant changes in the temperature dependence of the thermal conductivity, which could be a result of tuning of T^*. More specifically, the low-temperature thermal conductivity can be well approximated by a power law, and the exponent of the power law changes from a conventional value of about 3 to about 1.7 near the critical point. We will attempt to explain this in terms of increased scattering of the acoustic phonon modes, which are primarily responsible for heat conduction, by the optical modes that go soft at the structural transition. The power law is a natural consequence of the temperature dependence of the

population of the soft optical modes, which depends on the phonon spectrum, linewidth and the Bose-Einstein distribution.

Although this work was initially motivated by superconductivity, we believe it could potentially provide guidelines for the search of new thermoelectric materials. High-performance thermoelectric material is at the heart of solid-state cooling, which has no moving components and offers localised cooling. This has a wide range of current and future applications including temperature stabilisation of photodetectors and sensitive electronics, capture of waste heat from exhaust in automobiles and the future 'cryoelectronic' devices that utilise high-T_c superconductors [126]. The thermoelectric figure of merit, ZT, is given by

$$ZT = \frac{\sigma S^2 T}{\kappa}, \tag{4.1}$$

where σ, κ and S are the electrical conductivity, thermal conductivity and the Seebeck coefficient respectively. Currently, the best thermoelectric materials have $ZT \sim 1$ at their operating temperature. One way of improving ZT is to reduce the lattice conduction as much as possible by maximising phonon scattering while maintaining electrical conduction. This is the phonon-glass–electron-crystal idea first introduced by Slack [126, 127]. The filled skutterudite structures, which are closely related to the crystal structure of the $A_3T_4Sn_{13}$ system, are considered promising thermoelectric materials. Much like $A_3T_4Sn_{13}$, the filled skutterudites have a polyhedral cage with 12 atoms encasing a central atom. This crystal structure has a tendency to produce rattling modes which strongly scatter the acoustic phonon modes [126], reminiscent of the soft optical phonon modes responsible for driving the structural transition in $A_3T_4Sn_{13}$. Interestingly, $Y_3Ir_4Ge_{13}$, a 3-4-13 material, has been investigated for potential thermoelectric applications due to its caged structure, even though this particular material has a rather low ZT [128]. In materials with a tunable structural transition like the $A_3T_4Sn_{13}$ family, we could make use of the soft optical modes as a powerful scattering mechanism to reduce phonon thermal transport. Although $A_3T_4Sn_{13}$ would probably have low ZT because it is a metal, the search for better thermoelectric materials can be directed towards semiconducting materials with structural transitions at the required temperature for the specific application.

4.1.1 Structural transition in $A_3T_4Sn_{13}$ and comparison to $SrTiO_3$

As we have mentioned in Section 2.2.1, the order parameter of the structural transition in $A_3T_4Sn_{13}$ is the amplitude of the set of average atomic displacements associated with the transition. Using the ISODISTORT software package [129, 130], we compared the structure of the I phase with the I' phase of $Sr_3Rh_4Sn_{13}$ [18] at 100 K and isolated the distortions due to the order parameter. The amplitude of the distortions is amplified by a factor of 5 over the experimentally measured values and this is shown in Figure 4.1. Compared to Figure 3.2, we can see that the effect of the distortion is mainly to pinch and stretch the Sn icosahedra.

The temperature dependence of the soft optical modes of $Ca_3Ir_4Sn_{13}$ has been studied by Mazzone et al. [22] using inelastic neutron scattering, and the results are reproduced in Figure 4.2. The soft mode energy $\Delta \sim \sqrt{T - T^*}$, which is consistent with predictions of mean-field theory [131].

$SrTiO_3$ at around 105 K undergoes a similar structural transition. At room temperature, $SrTiO_3$ has a simple cubic structure and the structural transition at 105 K is also of the antiferroic variety [132]. Instead of a vanishing phonon frequency at the M point like the $A_3T_4Sn_{13}$ family, the transition in $SrTiO_3$ is driven by softening at the R point corresponding to $\mathbf{q} = (0.5, 0.5, 0.5)$ which is associated with rotation of the oxygen octahedra. Wavevectors $\mathbf{q}$ are in units of the reciprocal lattice vector $(2\pi/a)$ of the high-temperature phase. Definitions of the high-symmetry points in the Brillouin zone are given in Figure 3.1. The low-temperature structure has a tetragonal unit cell twice the volume of that of the high-temperature structure. Comparison to $SrTiO_3$ can be beneficial because it is a very well-studied system. In Figure 4.3 we can find the dispersion of the soft optical branch (labelled Γ_{25} following the notation of [133]) of $SrTiO_3$ [43]. Figure 4.4 shows the temperature dependence of the soft mode frequency before and after the transition, which is qualitatively similar to inelastic neutron scattering data of $Ca_3Ir_4Sn_{13}$ shown in Figure 4.2. This information will be complementary to the limited neutron scattering data on $A_3T_4Sn_{13}$.

4.1.2 Motivation

The typical description of a structural transition is the softening of one or more phonon modes (cf. Section 2.2.1). Similar to $SrTiO_3$ these modes should have zero frequency and linear dispersion at the critical point, which will closely resemble extra acoustic modes.

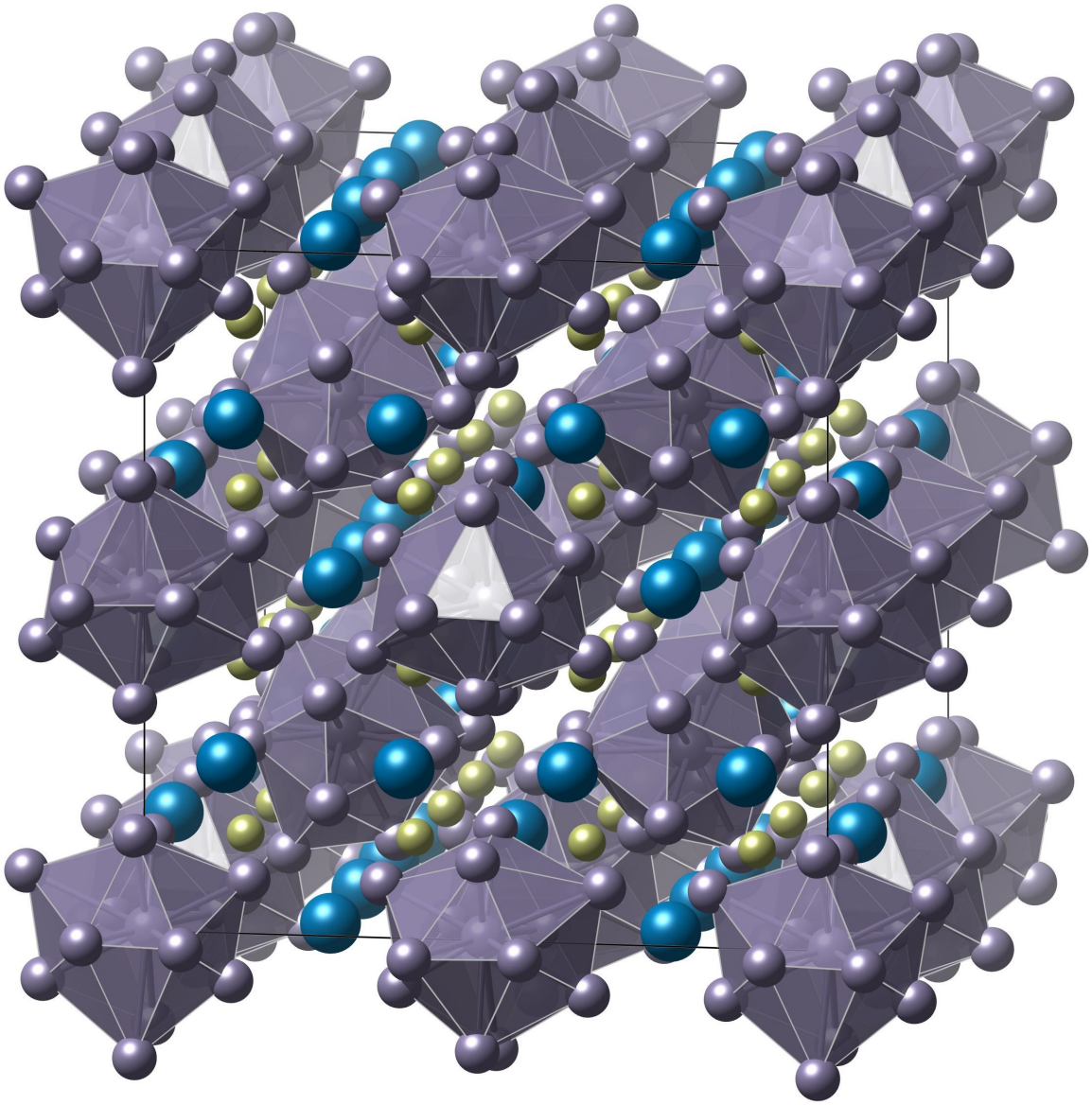

Fig. 4.1 The low-temperature crystal structure (I' phase) of $Sr_3Rh_4Sn_{13}$ which is representative of the $A_3T_4Sn_{13}$ family, showing only the distortions due to the order parameter at the M point. The amplitude of the distortion is exaggerated by a factor of 5 compared to the distortion measured experimentally at 100 K in [18]. The Sr, Rh and Sn are represented by cyan, olive and lavender-coloured spheres respectively.

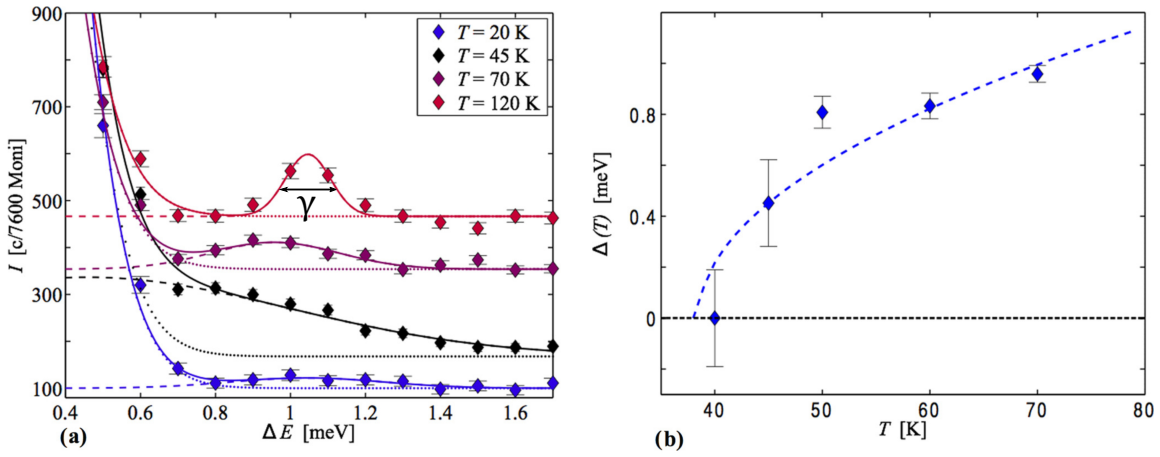

Fig. 4.2 Inelastic neutron scattering data of $Ca_3Ir_4Sn_{13}$ reproduced from [22]. (a) Energy scans at constant Q vector of (7/2, 7/2, 1). The parameter γ can be estimated from the FWHM of the peaks. (b) The temperature dependence of the peak position.

Naively, one might expect such modes to contribute extra thermal conductivity channels and increase the magnitude of thermal conductivity. However, it is important to note that in the $A_3T_4Sn_{13}$ material system, the q-vector of the soft modes is not at the Γ point, but at the M (and other symmetry equivalent) points. Being high-q modes, they are strongly affected by point defects through Rayleigh scattering since the scattering rate $\tau^{-1} \propto q^4$ [62]. Moreover, there is also potential for strong anharmonic coupling to other phonon modes close to the critical point. Hence, it is unclear from a fundamental point of view what the thermal properties of these soft phonon modes will be.

While materials with structural transitions are quite common, the $A_3T_4Sn_{13}$ material family has several unique properties which when combined offers an ideal system to study phonon interactions near structural transitions. Firstly, the transition temperature can be easily tuned by chemical substitution and can be suppressed to zero so we can study the system at low temperatures, far away from complications that usually arise at higher temperatures. In addition, due to its isotropic s-wave superconductivity [19, 107] with moderate $T_c \sim 5-8$ K, we can freeze out any electronic contribution to thermal conductivity by going well below T_c because the electrons bound in Cooper pairs do not carry heat [80]. The exact temperature cutoff is material-dependent but we can assume that the lattice contribution to thermal conductivity is dominant below about $0.2-0.3\ T_c$ [135]. For example, in Figure 2.6, we can see that for tantalum, the phonon thermal conductivity dominates at about $T/T_c < 0.3$. These properties together mean that the $A_3T_4Sn_{13}$ system is highly tunable, and in it we can study the physics of structural transitions without other complications.

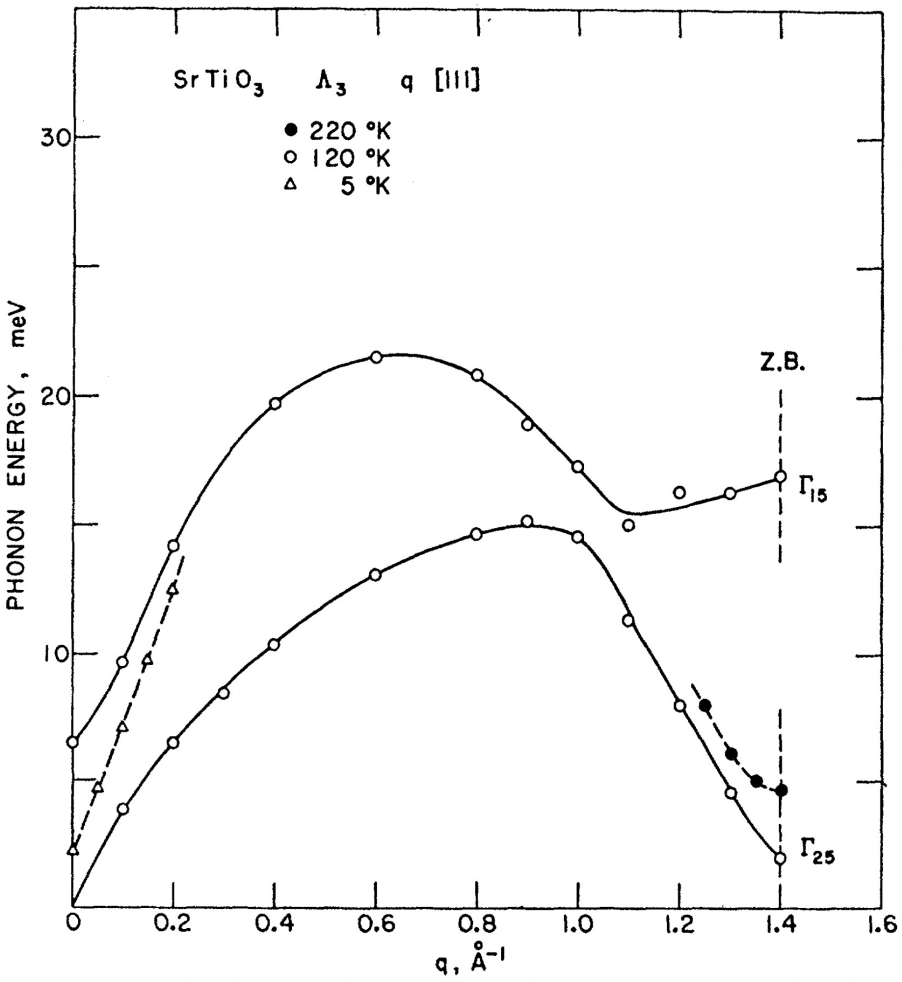

Fig. 4.3 Reproduced from [43]. Phonon dispersion of $SrTiO_3$, which has an antiferroic transition at around 105 K, measured by inelastic neutron scattering. The zone boundary marked by the dashed lines is at the *R* point (see Figure 3.1). The solid and empty circular data points are from the high-temperature phase. The triangular data points represent the dispersion of the soft mode in the low-temperature phase, where it has been folded back to the Brillouin zone centre.

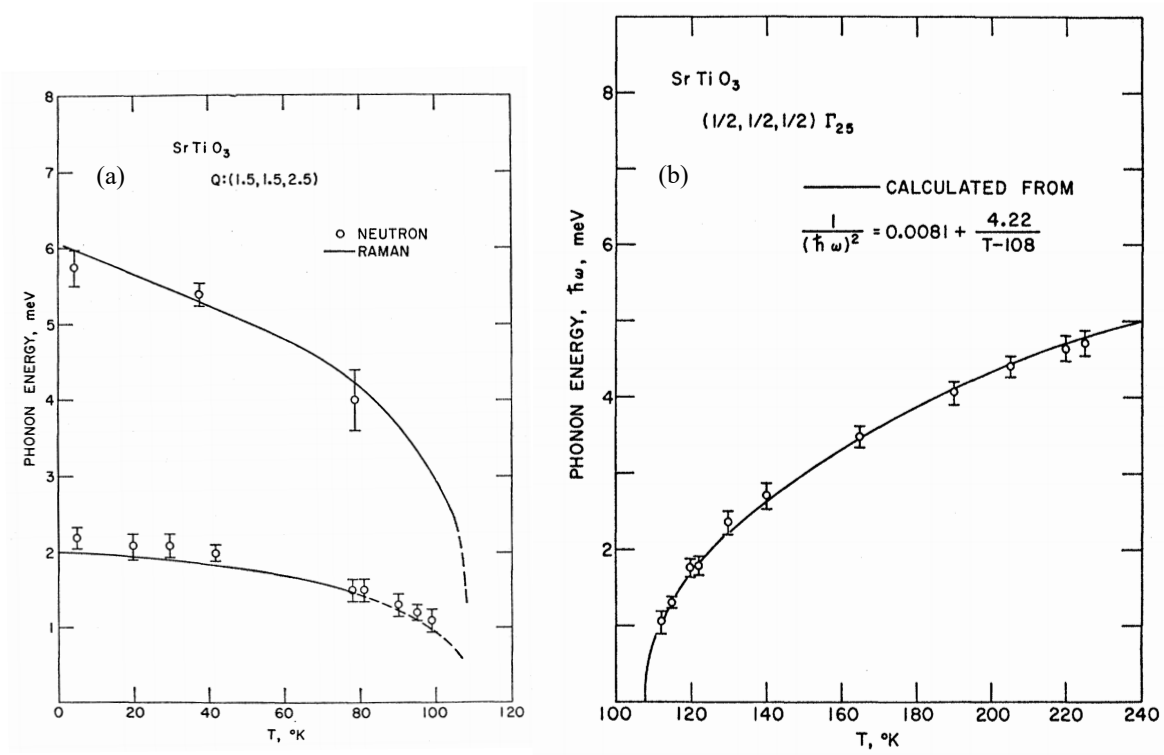

Fig. 4.4 Reproduced from [43] with data from [42]. The temperature dependence of the soft mode frequency of $SrTiO_3$ (a) after and (b) before the structural transition. The wavevector Q in both panels (a) and (b) are in units of the reciprocal lattice vector $(2\pi/a)$, where $a = 3.905$ Å [134] is the high-temperature lattice constant.

4.2 DFT calculations

We have seen in Section 2.3.1 how DFT can be deployed for phonon spectrum calculations. Before going into the experimental details, it will be informative to get an idea of what the phonon spectrum looks like at zero temperature, and how it changes as a function of the lattice constant. We have performed three phonon spectrum calculations using Quantum ESPRESSO [57] on $Sr_3Ir_4Sn_{13}$, labelled C1, C2, and C3 as shown in Figure 4.5. The local density approximation (LDA) was used to approximate the exchange-correlation functional. The pseudopotentials used are norm-conserving and non-relativistic. One parameter specific to Quantum ESPRESSO that strongly affects the results of the calculations is the phonon calculation threshold for self-consistency, `tr2_ph`. The default value of 10^{-12} proved to be insufficient, and it was reduced to 10^{-16}.

C1 was calculated with experimental lattice parameters (from [16]) whereas C2 and C3 were based on two sets of relaxed cell parameters. C1 yielded a calculated pressure of -40.83 kbar. C2 and C3 were calculated with reduced lattice constants that are 1.20% and 1.82% smaller than C1 and have pressures of -15.67 kbar and 0.02 kbar respectively. The atomic positions of C2 and C3 were relaxed. C2 and C3 calculations can be interpreted as high-pressure or large x analogues of C1 (where x is the substitution fraction in the $(Ca_xSr_{1-x})_3Rh_4Sn_{13}$ system). This calculation agrees well with the results of [103] which were calculated with VASP and PHONOPY.

We have also performed phonon spectrum calculations for $Sr_3Rh_4Sn_{13}$ using Quantum ESPRESSO, as shown in Figure 4.7(a). The pseudopotentials used for Sr and Sn are norm-conserving like in the previous calculation, and an ultrasoft pseudopotential is used for Rh. The lattice constant and atom positions for $x = 0$ are from single crystal x-ray diffraction [18]. The other calculations have reduced lattice constants calculated from Vegard's law (see Figure 4.6) and the atomic positions were relaxed. From Figure 4.6, we estimated that the change in lattice constant relative to $x = 0$ is about -0.960% from $x = 0$ to 1, and this was used to calculate the lattice constants for $x = 0.7$–0.89 relative to $x = 0$. The $x = 0$ calculation agrees well with the $Sr_3Rh_4Sn_{13}$ calculation done with VASP and PHONOPY in [18], although their calculation suggests that the system has greater instability towards distortions at the X point instead of the M point.

The usual convention for representing imaginary phonon frequencies, which is followed here, is to simply put them on the negative part of the frequency axis. We can see from calculations for both $Sr_3Ir_4Sn_{13}$ and $Sr_3Rh_4Sn_{13}$ that there are significant imaginary frequencies

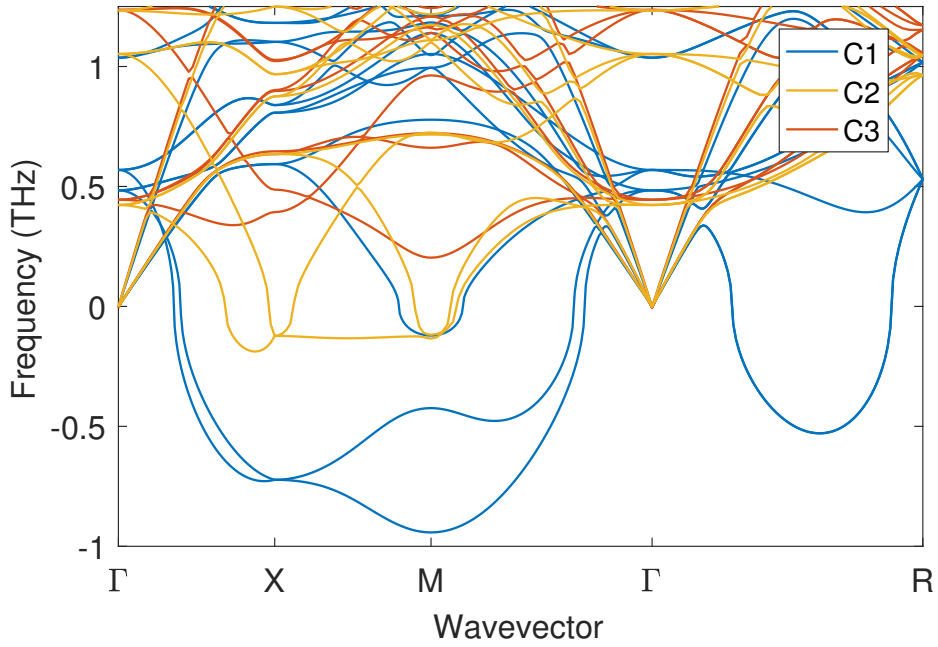

Fig. 4.5 Phonon spectrum calculations of $Sr_3Ir_4Sn_{13}$ in the high-temperature I phase ($Pm\bar{3}n$) performed with experimentally measured lattice parameters, as well as those obtained through a variable cell relaxation procedure with reduced lattice parameters, corresponding to a high pressure or substitution fraction x version of the original cell. The negative portion of the frequency axis represents imaginary frequencies, which indicates lattice instability.

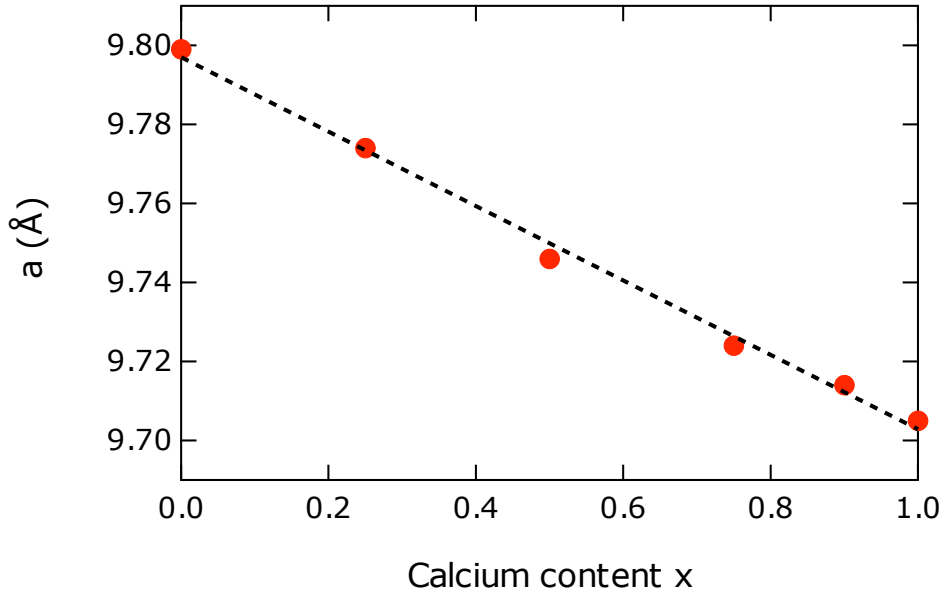

Fig. 4.6 As shown here, the substitution series $(Ca_xSr_{1-x})_3Rh_4Sn_{13}$ obeys Vegard's law. This is reproduced from Supplemental Material of [18]. Relative to $x = 0$, the change in lattice constant is approximately -0.960% from $x = 0$ to 1.

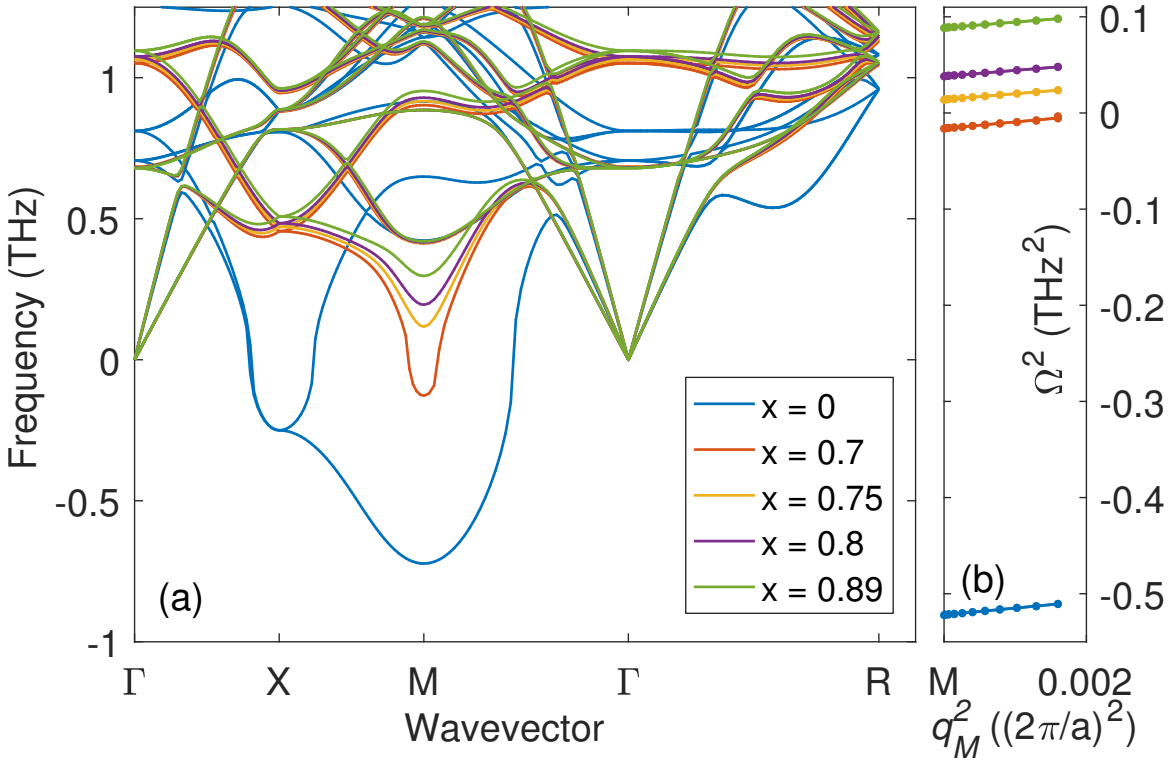

Fig. 4.7 (a) Phonon spectrum calculations for $Sr_3Rh_4Sn_{13}$ in the high-temperature I phase ($Pm\bar{3}n$) using experimentally measured lattice constant for $x = 0$ and reduced lattice constants determined from Vegard's law for the other calculations. The negative portion of the frequency axis represents imaginary frequencies. (b) Frequency squared (Ω^2) of the soft optical mode at the M point as a function of wavevector squared (q_M^2) measured relative to the M point. A negative Ω^2 value means that the frequency is imaginary, which indicates lattice instability.

at the X and M points. Normal modes with imaginary frequencies in DFT calculations mean that the system is unstable with respect to lattice distortions associated with those modes—small distortions will result in a lower overall energy. Going from $x = 0$ to 0.89, we reduced the lattice constant, which is equivalent to increasing hydrostatic pressure. The magnitudes of the imaginary frequencies are reduced until they become real and the high-temperature I phase is stabilised. This occurs by $x = 0.75$, which do not show any imaginary frequencies. However, we can still see the remnant soft mode at the M point. This suggests that the soft optical mode at the M point persists away from the critical point. This also suggests that the critical substitution fraction estimated by DFT is $0.7 < x_c < 0.75$, which is not far from the critical point of $x_c = 0.9$ measured by Goh et al. [18].

The dispersion of the soft optical mode, with frequency Ω and wavevector q_M measured from the M point, can be described by $\Omega^2 = \Delta^2 + v_o^2 q_M^2$. In Figure 4.7(b), we show the dispersion of this soft optical mode. As x goes from 0 to 1, Δ^2 increases and becomes positive at x_c while v_o^2 remains essentially constant. The values of Δ and v_o are listed in Table 4.1. Some additional pieces of information we can extract from our $Sr_3Rh_4Sn_{13}$ phonon calculation are the speeds of sound of the acoustic modes. In the $\Gamma - X$ direction, for $x = 0$, we find the gradients of the two shallower branches to be $v_{a1} = 1903$ m/s, and that of the steeper branch to be $v_{a2} = 3816$ m/s. These values are largely independent of x. Also, these values are comparable to the speeds of sound from the DFT calculations done by Goh et al. [18], which are about 2200 m/s for the shallower branches and 4600 m/s for the steeper branch.

x	Δ (THz)	v_o (m/s)
0	$0.7225i$	2609
0.7	$0.1272i$	2563
0.75	0.1182	2415
0.8	0.1956	2409
0.89	0.2976	2382

Table 4.1 Parameters describing the dispersion of the soft optical mode extracted from phonon spectrum calculations of $(Ca_xSr_{1-x})_3Rh_4Sn_{13}$.

4.3 Experimental results

4.3.1 Sample characterisation

Our experimental work, which includes the measurement of electrical resistivity, thermal conductivity and heat capacity, were done on 7 members ($x = 0$, 0.25, 0.5, 0.75, 0.85, 0.9 and 1) of the substitution series $(Ca_xSr_{1-x})_3Rh_4Sn_{13}$. The substitution fraction x is nominal but we believe that they are close to the real values because the lattice constants, measured by powder x-ray diffraction, vary linearly with x and obey Vegard's law as shown in Figure 4.6. The errors associated with x will be discussed in Section 4.3.4. These samples are single crystals grown by the Sn flux method similar to [102] and are from the same batch as that used in [20]. Electrical resistivity was measured in a Quantum Design Physical Property Measurement System (PPMS) at zero magnetic field, down to about 2 K. All samples were contacted with 25 μm gold wires in the standard 4-point geometry using either spot-welding [136] or Dupont 6838 silver epoxy. A photograph of one of the samples is shown in Figure 4.8. For samples $x = 0$, 0.25, 0.5, 0.75 and 0.85, the exact same sample was used in both electrical resistivity and thermal conductivity measurements. For samples $x = 0.9$ and 1, these two measurements were done on different samples. This is because there was some surface damage during the contact-making process by spot-welding which was acceptable for thermal conductivity but affected electrical resistivity. Hence, for electrical resistivity measurements in these samples, contacts were made with silver epoxy. A summary of the samples measured can be found in Table 4.2. The geometric factor is defined as tw/L, where t, w and L are the thickness, width and length between voltage contacts (for electrical resistivity) respectively. These quantities are measured by taking a photograph with a microscope that has been calibrated and using image processing software. We estimate that each individual length measurement has an error of about 5% owing to the non-uniformity of a real sample. Assuming that the errors are uncorrelated, the error in the geometric factor is about $\sqrt{3} \times 5\% \simeq 8.7\%$. The "voltage" contacts were connected to the $T+$ and $T-$ thermometers and the "current" contacts were connected to the heater and thermal ground during the thermal conductivity experiments. The same geometric factors were used in the calculation of electrical resistivity and thermal conductivity.

In the normalised electrical resistivity data shown in Figure 4.9, we see a distinctive kink at the structural transition temperature T^* for the $x = 0$–0.75 samples, similar to that reported in the literature [16, 18, 102]. The transition at T^* is well defined for $x = 0$ and 0.25, but

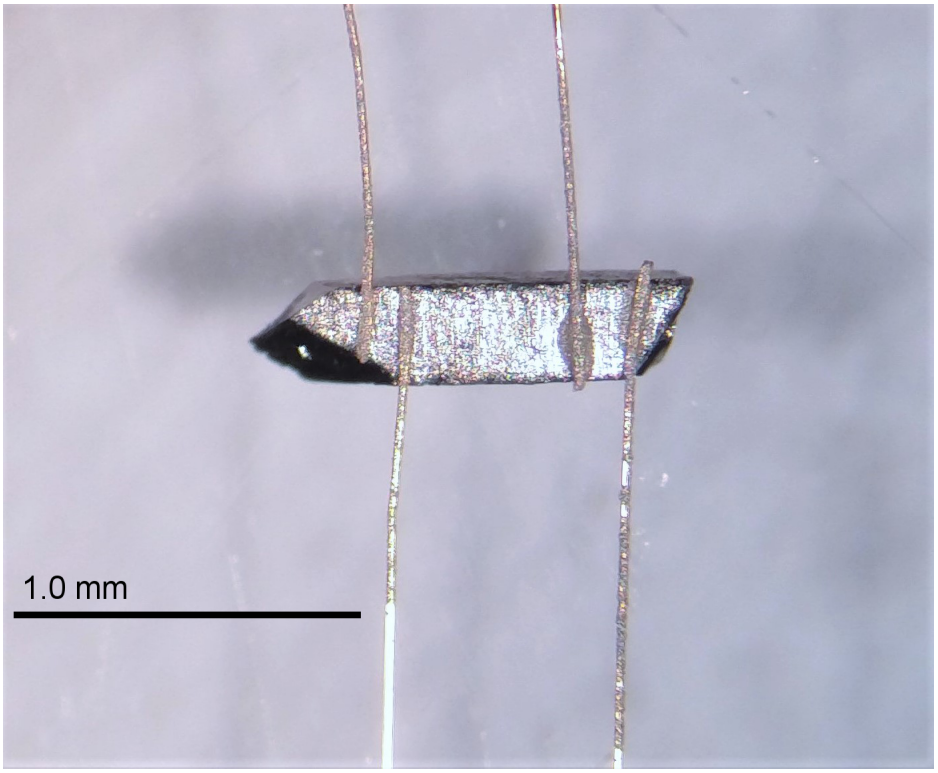

Fig. 4.8 A photograph of a $(Ca_xSr_{1-x})_3Rh_4Sn_{13}$ sample with $x = 0.5$ taken with a microscope.

x	T_c (K)	T^* (K)	Geometric factor (μm)	Room temperature resistivity ($\mu\Omega$m)	Residual resistivity (nΩm)
0	4.7 ± 0.3	137 ± 1	81 ± 7	0.79 ± 0.07	39 ± 4
0.25	5.4 ± 0.2	90 ± 1	53 ± 5	4.0 ± 0.3	760 ± 70
0.5	7.2 ± 0.1	45 ± 4	52 ± 5	1.6 ± 0.1	440 ± 40
0.75	7.4 ± 0.1	30 ± 3	33 ± 3	1.1 ± 0.1	260 ± 20
0.85	7.9 ± 0.2	-	105 ± 9	2.4 ± 0.2	380 ± 34
0.9	$7.8 \pm 0.1^{\rho}$	-	$33 \pm 3^{\kappa}$ $140 \pm 13^{\rho}$	$3.5 \pm 0.3^{\kappa}$ $1.2 \pm 0.1^{\rho}$	$1500 \pm 130^{\kappa}$ $230 \pm 20^{\rho}$
1.0	$8.0 \pm 0.1^{\rho}$	-	$120 \pm 11^{\kappa}$ $260 \pm 23^{\rho}$	$3.8 \pm 0.3^{\kappa}$ $3.7 \pm 0.3^{\rho}$	$700 \pm 60^{\kappa}$ $610 \pm 50^{\rho}$

Table 4.2 A summary of $(Ca_xSr_{1-x})_3Rh_4Sn_{13}$ samples measured. The superscript labels κ and ρ represent the different samples used for thermal conductivity and electrical resistivity measurements respectively. Room temperature resistivities are measured at 300 K. The errors in the resistivities are dominated by the errors in the geometric factor. The variations of room temperature resistivity between samples are large and unexpected. This could be an area for future investigation.

is much more smeared out for $x = 0.5$ and 0.75. In the latter samples, T^* is taken to be the middle of the temperature window over which the transition is observed and half of this temperature width is taken to be the error, which is recorded in Table 4.2. The structural transition temperature of most of the samples is in good agreement with the phase diagram in [18], reproduced in Figure 3.3. The only exception is $x = 0.5$ where Goh et al. [18] measured a more well-defined transition that is about 10 K higher.

The resistivity data shown here is normalised to the room temperature (300 K) value because the measured room temperature resistivities vary strongly between samples and do not appear to follow any clear trend. The room temperature resistivities are recorded in Table 4.2. We are unsure of the origin of these variations. The uncertainty in the geometric factor will affect the determination of the absolute value of resistivity but this should be less than 10%, as noted previously. A similar variation in room temperature resistivities between samples had also been observed by Goh et al. (shown in Supplemental Material of [18]). The room temperature resistivity of $Sr_3Rh_4Sn_{13}$ is about 7 $\mu\Omega$m, which is about a factor of 6 larger than the room temperature resistivity of $Ca_3Rh_4Sn_{13}$, which is about 1.2 $\mu\Omega$m. These are very different from our measured values and suggest that the absolute value of resistivity differ greatly even among samples of the same nominal stoichiometry. One possible explanation is the presence of fractures in some of the samples which will increase the real geometry factor and the apparent resistivity.

When we focus on the low-temperature segment of resistivity shown in the inset in Figure 4.9, we observe a range of temperatures $T_c < T < 40$ K where the resistivity of samples $x = 0.9$ and 1 have a T-linear temperature dependence, much like that previously reported [16, 18]. This feature was attributed by Klintberg et al. [16] to scattering by low-lying phonon modes that are expected to be present in systems close to a structural transition, analogous to simple metals above the Debye temperature.

There were some concerns regarding the purity of these samples and whether the samples consist of a distribution of spatial domains giving rise to a distribution of T_c. To address these concerns, we have measured the susceptibility of two samples with $x = 0.9$ and 1 in a Cryogenic SQUID magnetometer shown in Figure 4.10. The sharpness of the superconducting transitions increases our confidence in the quality of these samples. The superconductivity onset temperature in magnetic susceptibility closely matches that of resistivity.

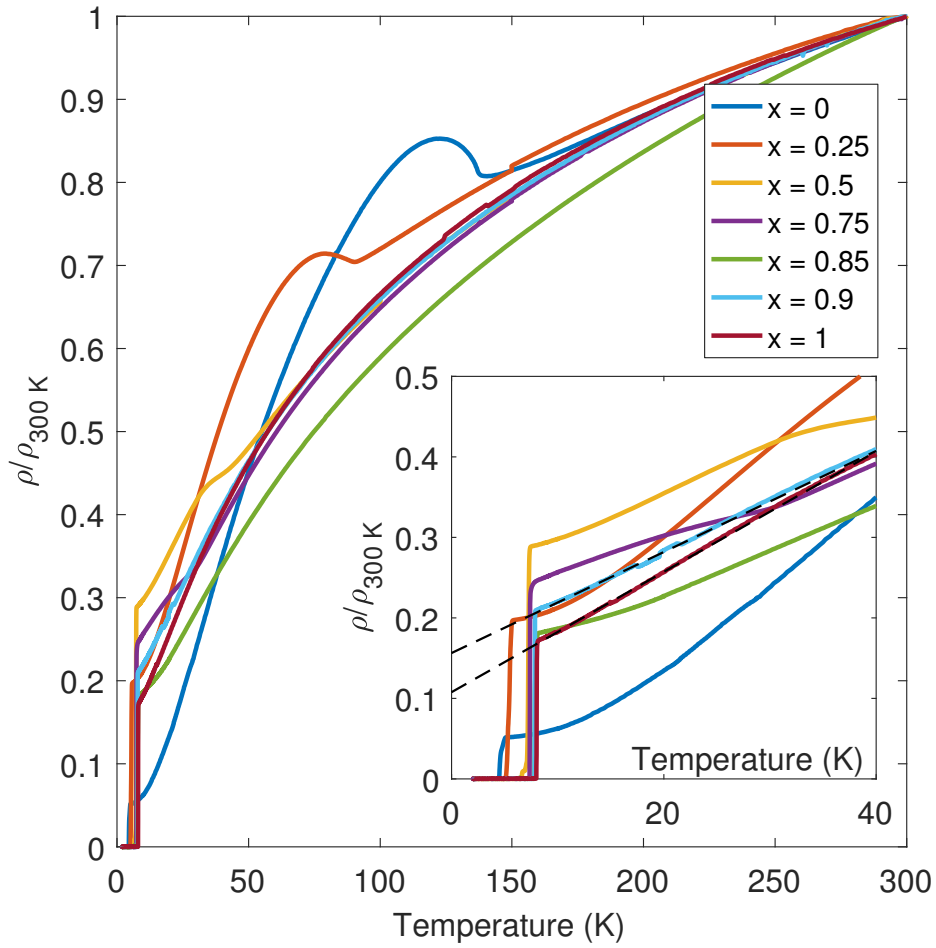

Fig. 4.9 The electrical resistivity of $(Ca_xSr_{1-x})_3Rh_4Sn_{13}$ measured with the 4-point geometry from room temperature to 2 K, normalised to the room temperature value. The differences in the magnitude of the resistivity are mainly due to variations in sample quality. The inset focuses on the low-temperature portion of the resistivity, where we see a wide range of temperatures with T-linear dependence in the $x = 0.9$ and $x = 1$ samples, just like that observed in [18].

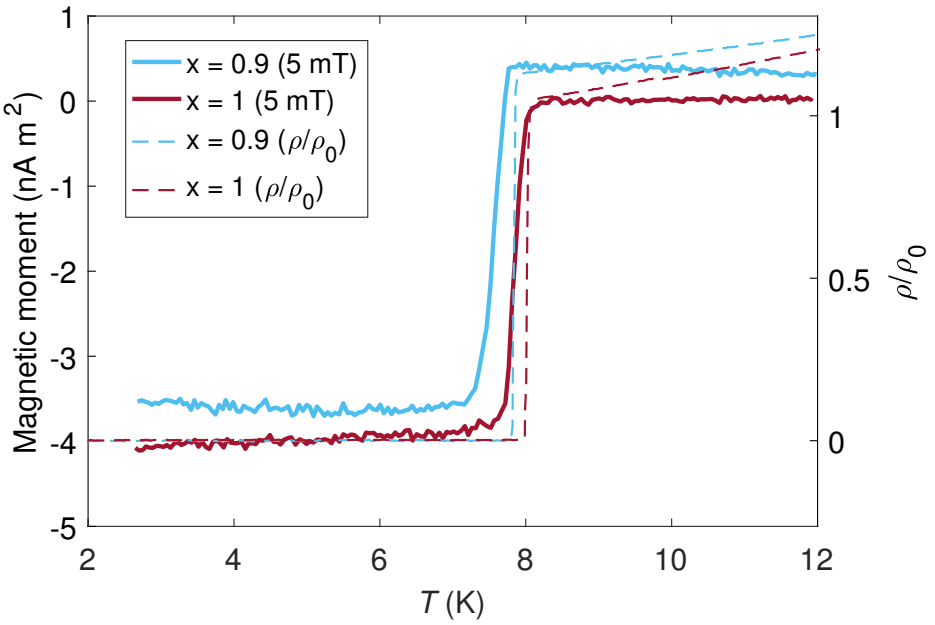

Fig. 4.10 Magnetic moment of two $(Ca_xSr_{1-x})_3Rh_4Sn_{13}$ samples with $x = 0.9$ and 1, as a function of temperature in a small applied field of 5 mT measured in a Cryogenic SQUID magnetometer. The results are not converted to magnetisation as it is difficult to calculate with any reliability the volume and demagnetizing factor of these very small samples. The superconductivity transitions measured in resistivity (normalised by the residual resistivity ρ_0, the vertical axis is on the right-hand side) are shown in dashed lines for comparison.

4.3.2 Heat capacity

We have performed heat capacity measurements down to about 0.5 K for three samples close to the quantum critical point at $x = 0.5$, 0.75 and 0.85 to check for any anomalous behaviour due to the structural transition. This was thought to be unlikely since the heat capacity data from [20] shows no deviation from T^3 behaviour down to 2 K. These three samples are larger crystals from the same batch as those used in the thermal conductivity measurements. The heat capacity data is shown in Figure 4.11. Comparison between our heat capacity data and that from [20] is shown in Table 4.4. The T_c for $x = 0.75$ and 0.85 measured by heat capacity agrees very well with the resistive T_c recorded in Table 4.2 but they differ slightly for $x = 0.5$. The heat capacity T_c for that sample is 6.6 ± 0.1 K and the resistive T_c is 7.2 ± 0.1 K.

The same heat capacity data is plotted on a log-log scale in Figure 4.12. The dark lines show the linear fit regime starting from $T/T_c < 0.25$ and the exponents of the power laws for $x = 0.75$ and 0.85 are close to the expected value of 3 while the exponent for $x = 0.5$ is slightly lower than expected. The errors of the exponent come from the standard error from the least-square fitting routine. For $x = 0.75$, there is an anomalous feature at around $0.0951 < T/T_c < 0.131$ which is excluded from the fit. We did not observe such a feature in the thermal conductivity data, and this feature most likely originates from the heat capacity addenda.

In anticipation of further analysis, we also plot the data for the $x = 0.85$ sample in the form of C/T^3 against T in Figure 4.13 to check if there is a finite T-linear or $T^{1.5}$ term in the heat capacity, which will show up as a divergence as $T \to 0$. Since C/T^3 seems to have no temperature dependence, we conclude that neither terms are present. This is consistent with the scenario whereby the $A_3T_4Sn_{13}$ system has a fully gapped, s-wave superconductivity.

4.3.3 Thermal conductivity

Our thermal conductivity experiments were done on samples with the same seven stoichiometries. These samples were measured down to about 0.3 K in zero field and the raw data is shown in Figure 4.14(a). For the $x = 0$ and 0.25 samples, there are visible peaks at around 15 K and 30 K respectively that are typical of the electronic thermal conductivity of relatively pure metallic samples [135]. All the samples show a distinct kink in thermal

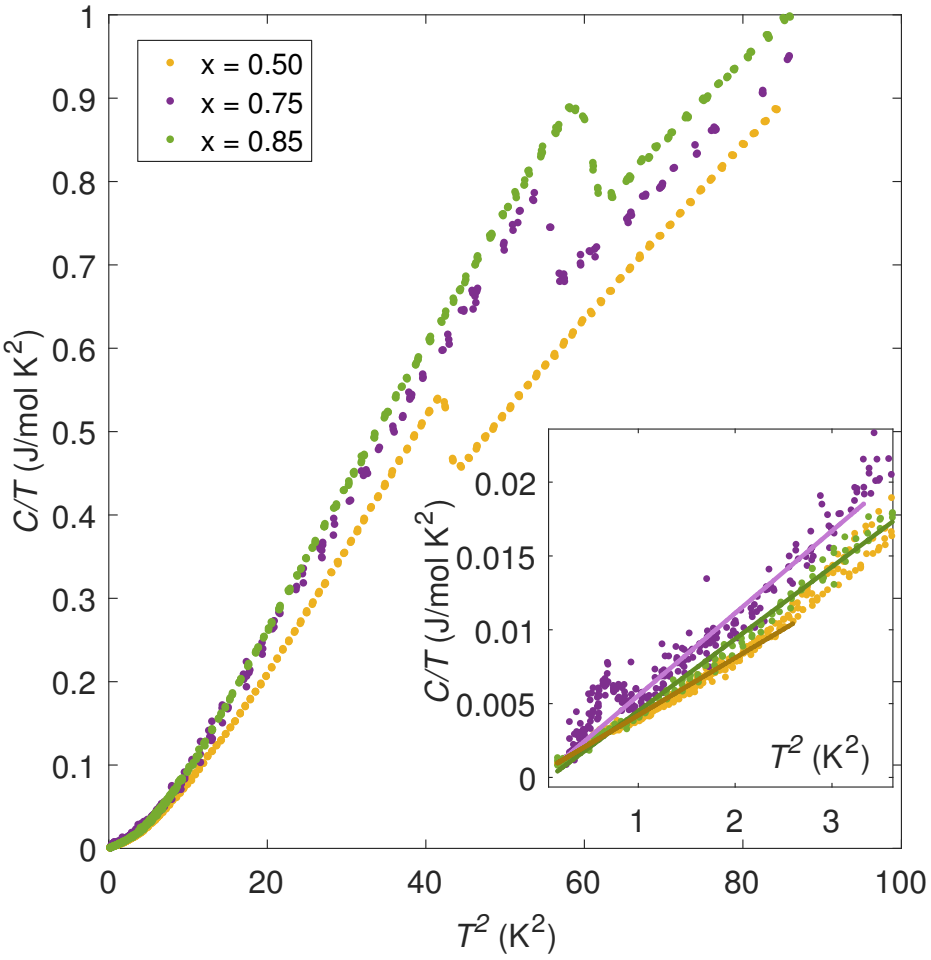

Fig. 4.11 The heat capacity of three $(Ca_xSr_{1-x})_3Rh_4Sn_{13}$ samples in the series closest to the critical point. The sharpness of the superconductivity transition feature indicates the bulk quality of the samples. The inset shows the linear fits used to extract the gradient in the range of $T/T_c < 0.25$. There is an anomalous peak-like feature in the $x = 0.75$ sample in the inset. We believe that this feature is due to the heat capacity addenda rather than the sample. The size of the heat capacity jump at the superconducting transition is consistent with that observed by Yu et al. [20], which is about twice that of the BCS value and indicates strong electron-phonon coupling.

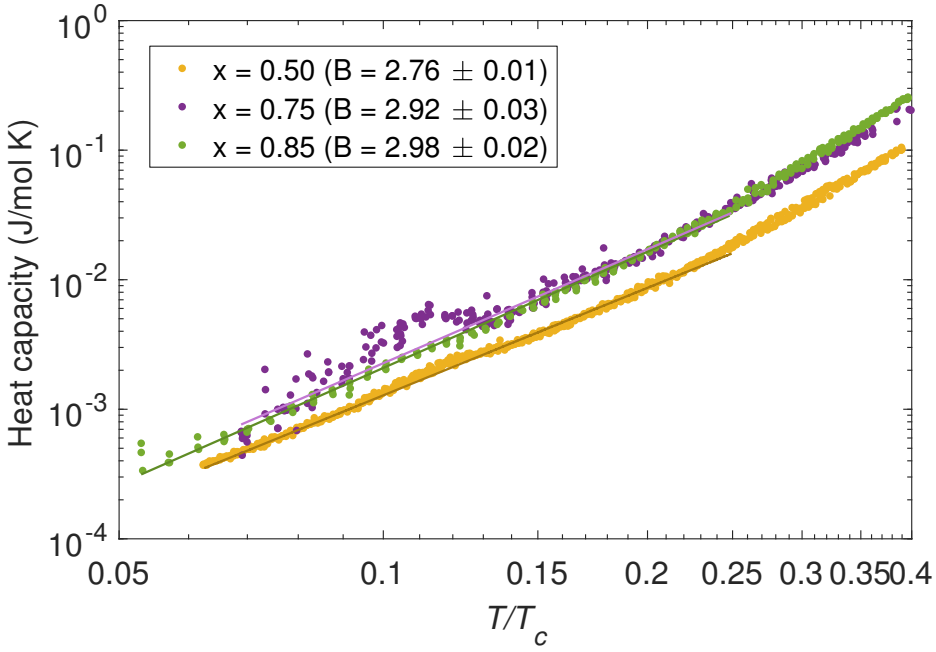

Fig. 4.12 The heat capacity data of three $(Ca_xSr_{1-x})_3Rh_4Sn_{13}$ samples in a log-log plot. The range of the power law fit starts from $T/T_c < 0.25$ excluding a range of temperatures $0.0951 < T/T_c < 0.131$ where the $x = 0.75$ sample shows an anomalous peak-like feature. We believe that this feature is due to the heat capacity addenda rather than the sample. The exponent of the power law is given as B in parentheses. The temperature dependence of the heat capacity for all samples follows approximately a T^3 power law.

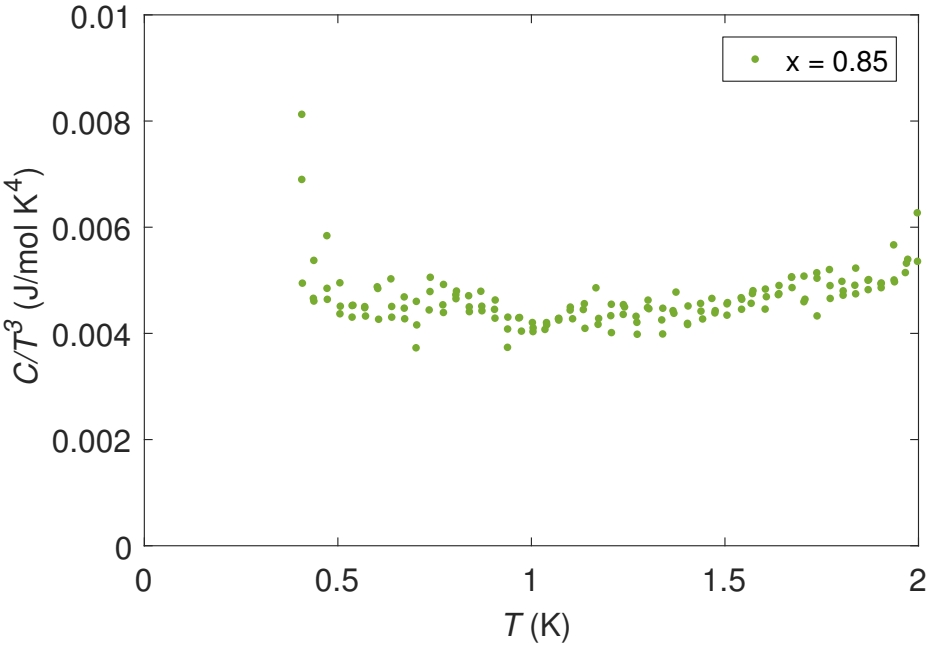

Fig. 4.13 Low-temperature heat capacity data of a $(Ca_xSr_{1-x})_3Rh_4Sn_{13}$ sample with $x = 0.85$. We want to check for the existence of T-linear or $T^{1.5}$ contributions, which from the data is negligible.

conductivity at the superconducting transition temperature. The effects of superconductivity on thermal conductivity are more clearly seen when plotted in κ/T in Figure 4.14(b). Up until around T_c, the thermal conductivity is dominated by electrons, as evinced by the near temperature independence of κ/T. The dramatic peak at $T/T_c \sim 0.5$ is very similar to that observed in Pb-Bi alloys [137] as well as in tantalum (see Figure 2.6) and niobium [79]. As we have discussed in Section 2.5.1, this is usually attributed to the reduction in electron-phonon scattering which greatly increases the mean free paths of the phonons, and more than compensates for the loss of thermal conductivity from the normal state electrons.

4.3.4 Low-temperature power laws

It is very interesting to look at thermal conductivity at the lowest temperatures ($T/T_c < 0.25 \sim$ 1–2 K), which is dominated by lattice conduction (cf. Section 4.1.2). Using the simple kinetic theory, the thermal conductivity of an isotropic material is given by Equation 2.27. It is natural to expect that the phonon mean free path at these temperatures to be limited by the boundary of the sample. This is reasonable considering these samples have maximum phonon mean free path of about 300 μm or less (as we will see later in Table 4.5).

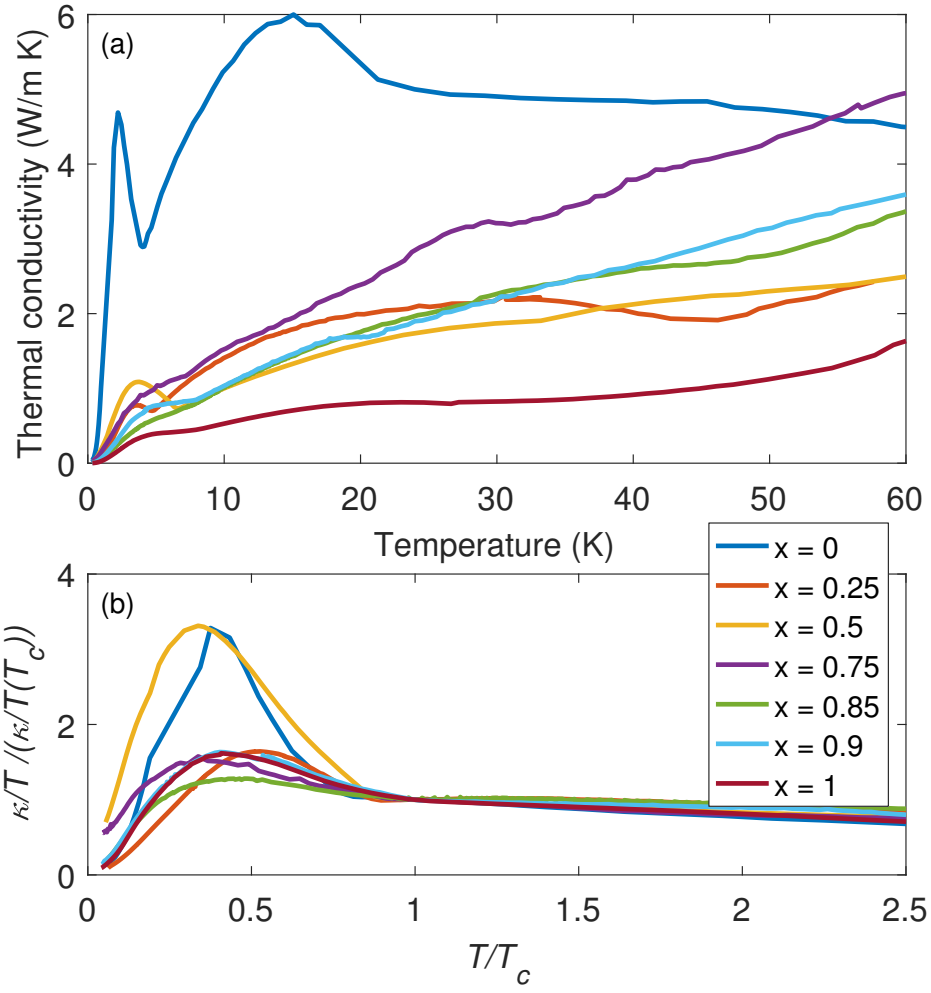

Fig. 4.14 (a) The thermal conductivity of members of the series $(Ca_xSr_{1-x})_3Rh_4Sn_{13}$. The sharp kink below 8 K signifies the onset of superconductivity. (b) Temperature dependence of κ/T. The temperature is normalised by the respective T_c of the sample and the vertical axis is normalised by its value at $T = T_c$. The freezing out of normal state electrons below T_c results in reduced electron-phonon scattering and an enhancement in phonon thermal conductivity. This creates the peak in κ/T below T_c.

For comparison, in LiF [138], samples which are several mm thick reach their boundary-limited regime by about 6 K. For ease of comparison, this data is reproduced in Figure 4.15. In this scenario, the thermal conductivity should have the same temperature dependence as the lattice heat capacity, which is proportional to T^3 [139].

The temperature dependence of the thermal conductivity is shown in Figure 4.16 in a log-log plot. We can see that while the data is well described by a simple power law $\kappa \propto T^A$, the exponent A varies as we traverse the phase diagram. In Figure 4.17, the exponent A is plotted against the substitution fraction x. For the end member $Sr_3Rh_4Sn_{13}$, the expected T^3 power law is observed. The exponent A decreases steadily as we cross the phase diagram via substitution of Sr by Ca, and it dips to a minimum of about 1.7 at $x = 0.75$, near the quantum critical point. After that, A recovers sharply to about 2.5 at the other end member $Ca_3Rh_4Sn_{13}$.

The residual of the power law fits is shown as the inset in Figure 4.16 . We can see that the residual has some temperature correlations as opposed to being completely random. There are two possible explanations for this. Firstly, this could be due to some small remaining electronic contribution to thermal conductivity. Alternatively, it is also possible that the thermal conductivity could be described by a more complicated function that only resembles a power law in this temperature regime. Either way, this deviation will dominate in the error analysis of A. We estimate the error of A by using two other temperature cutoffs—$T/T_c < 0.3$ and $T/T_c < 0.2$—and use half of the difference in A between these cutoffs as the error. These cutoffs are chosen because we expect the phonon thermal conductivity to dominate at approximately this temperature range as seen in Figure 2.6. This error analysis procedure cannot be applied to the $Sr_3Rh_4Sn_{13}$ sample because of a gap in the data in the temperature range of $0.2 < T/T_c < 0.3$, and we assigned to it the same error as the $x = 0.5$ sample. The error in stoichiometry x, estimated from deviations from Vegard's law shown in Figure 4.6, is about 2.2%. These errors are reflected in the error bars in Figure 4.17.

Using the power law exponents A that we have obtained, we performed a linear fit to the thermal conductivity data with the form $\kappa = aT^A + bT$. The exponents A are fixed. This is to check if there is any significant residual metallic contribution to thermal conductivity. We list the values of A and b in Table 4.3. The relative T-linear contributions to thermal conductivity are small and the errors in b are significant, suggesting that the metallic T-linear contribution is frozen out. This is within our expectation since we have numerous pieces of evidence pointing towards a nodeless superconducting gap in the $A_3T_4Sn_{13}$ system.

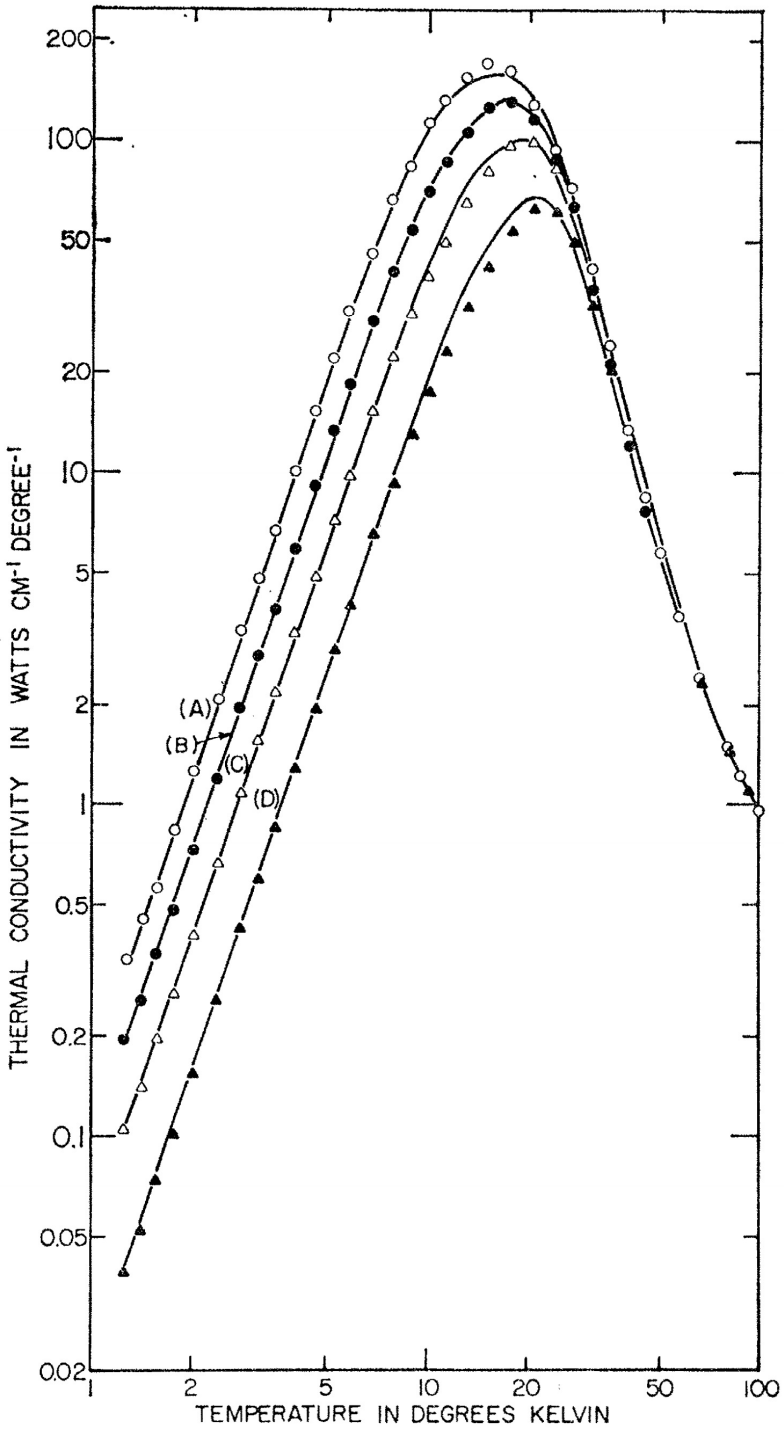

Fig. 4.15 Reproduced from [138]. Thermal conductivity as a function of temperature, shown in a log-log scale, of LiF crystals with sandblasted surfaces. These samples show excellent agreement with boundary-limited phonon thermal conductivity with T^3 temperature dependence. The samples labelled A to D have effective dimensions of 7.25 mm, 4.00 mm, 2.14 mm and 1.06 mm respectively.

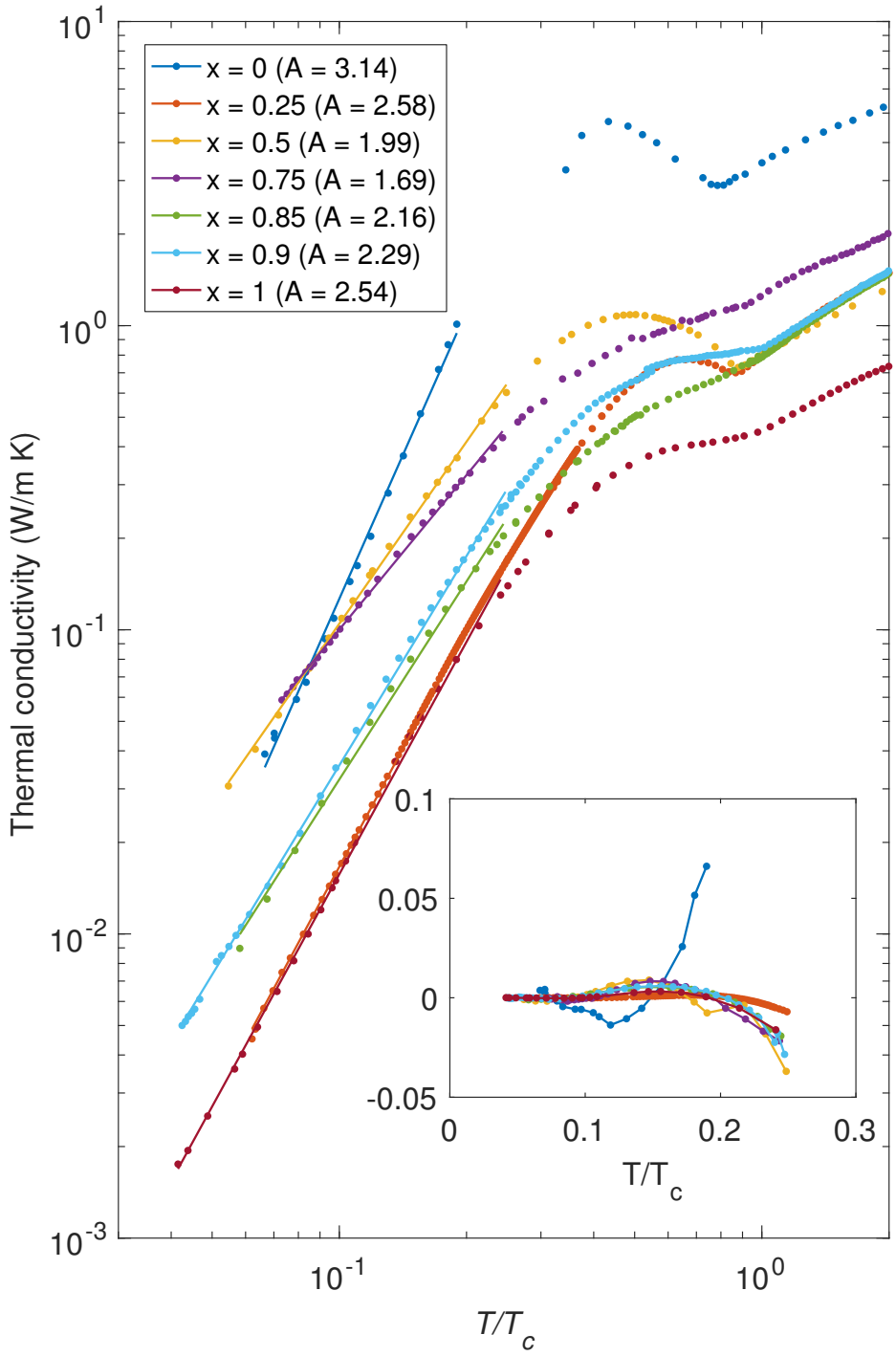

Fig. 4.16 The thermal conductivity of $(Ca_xSr_{1-x})_3Rh_4Sn_{13}$ samples on a log-log plot. The data is represented by dots and the solid lines show the linear fits from $T/T_c < 0.25$ to the lowest temperature measured. The exponent of the power law from the fit is given as A in parentheses. The inset shows the residual of the power law fits. The residual is clearly correlated at higher temperatures, and this is important when estimating the error of the exponent A.

x	A	b ($\times 10^{-3}$ W/m K^2)
0	3.14 ± 0.034	-38.8 ± 9.4
0.25	2.58 ± 0.040	4.1 ± 0.5
0.5	1.99 ± 0.034	20.5 ± 5.1
0.75	1.69 ± 0.035	13.8 ± 4.4
0.85	2.16 ± 0.10	12.7 ± 3.3
0.9	2.29 ± 0.049	11.1 ± 2.4
1	2.54 ± 0.051	4.3 ± 1.3

Table 4.3 The power law exponent A and the coefficient b of the T-linear portion of thermal conductivity of $(Ca_xSr_{1-x})_3Rh_4Sn_{13}$.

We have measured different samples with the same nominal stoichiometry of $x = 0.5$ and 0.75 with different surface treatments. Samples $x = 0.5$ S4 and $x = 0.75$ S1, which are shown in the previous figures, were contacted as grown without any special treatment. Samples $x = 0.5$ S6 and $x = 0.75$ S3 have surfaces that were roughened with grit 1000 sandpaper. The purpose of this surface treatment is to rule out specular reflections which could result in thermal conductivity power law exponent of less than 3. The results of these measurements are shown in Figure 4.18. The range of temperatures for the power law fit is truncated for $x = 0.75$ S3 to match S1. The exponents of the power law fits are slightly different between samples with the same nominal stoichiometry and this could be explained by differences in the true stoichiometry of these two samples. The significance of these results and their implications on boundary scattering and specular reflection will be discussed in greater detail later in Section 4.4.1.

4.3.5 Phonon mean free path

To better inform and constrain theoretical explanations for our observations, we will estimate the phonon mean free path with the assumption that all the heat is transported by the lowest acoustic phonon modes. To this end, we need the speed of sound and the phonon heat capacity. We can find the phonon heat capacity coefficient β defined by the molar heat

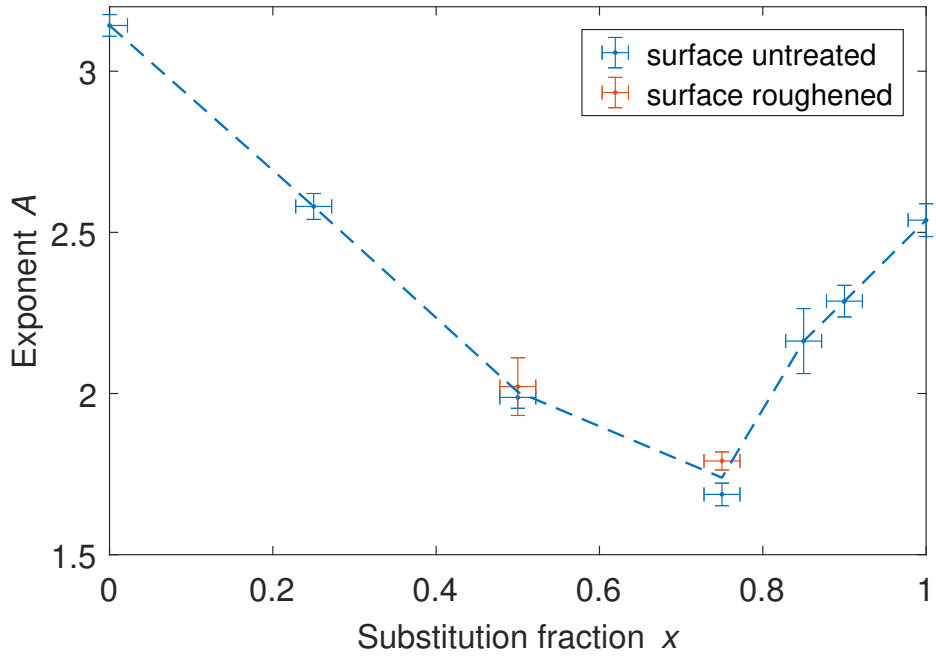

Fig. 4.17 The thermal conductivity power law exponents A of $(Ca_xSr_{1-x})_3Rh_4Sn_{13}$ from Figure 4.16 are extracted and plotted against the substitution fraction x. A clear trend, presented by the dashed line as a guide to the eye, can be seen, with the minimum close to the quantum critical point. The estimated errors in the exponent and in x are shown, and their derivation is discussed in the text.

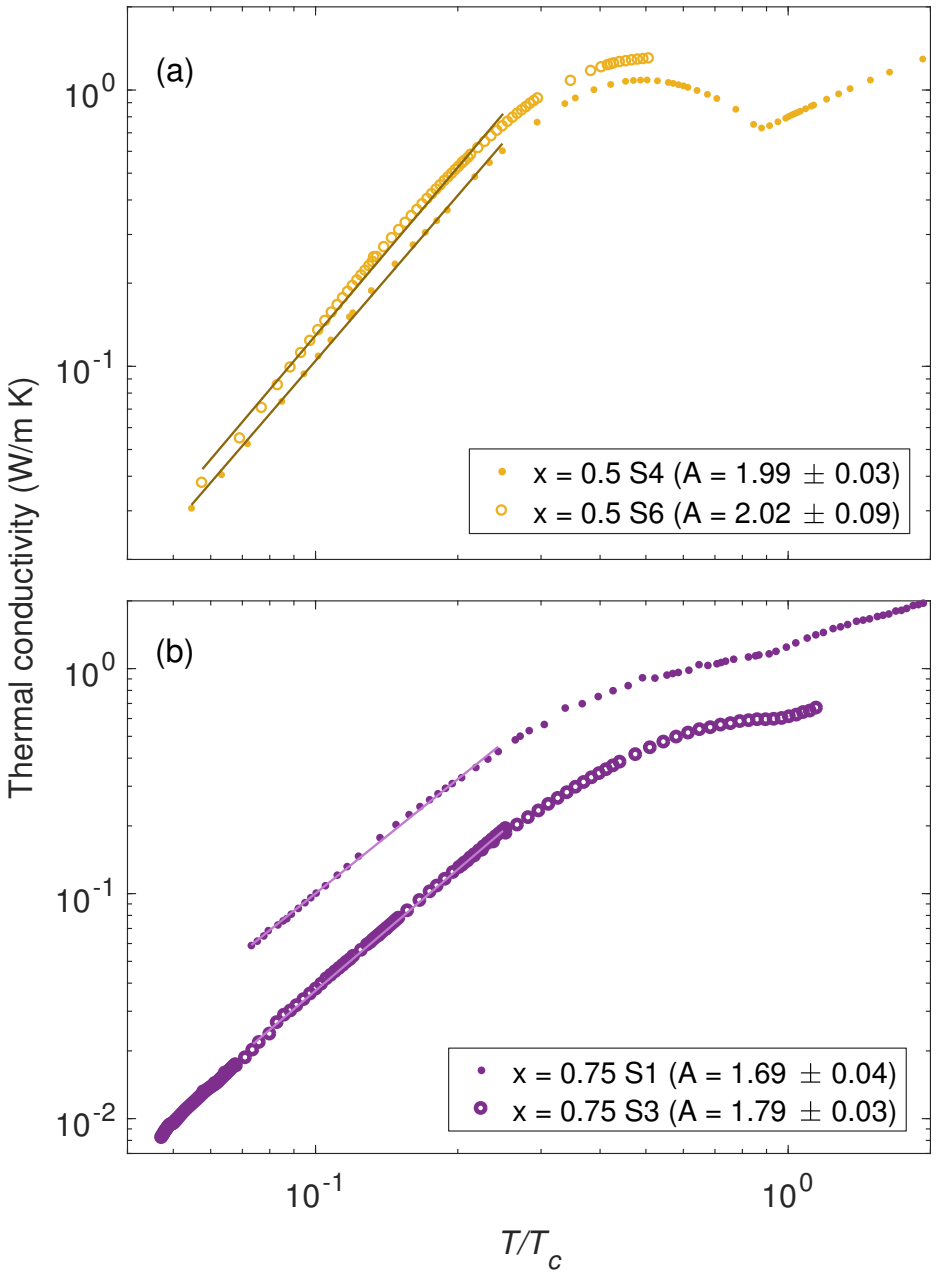

Fig. 4.18 Runs with $(Ca_xSr_{1-x})_3Rh_4Sn_{13}$ samples with different surface treatments. Samples $x = 0.5$ S4 and $x = 0.75$ S1 are measured as grown while samples $x = 0.5$ S6 and $x = 0.75$ S3 have surfaces that were roughened with grit 1000 sandpaper. (a) Two samples with $x = 0.5$. S6 deviates more from the linear fit, and this is reflected in the larger error in exponent A. (b) Two samples of $x = 0.75$. The fit range of S3 is truncated to match that of S1.

capacity $C_{ph} = \beta T^3$ from [20, 124, 140] using

$$\beta = \frac{12\pi^4}{5\Theta_D^3} NR, \tag{4.2}$$

where Θ_D is the Debye temperature, $N = 20$ is the number of atoms in a formula unit and R is the gas constant [62]. This is presented in Table 4.4. We have also included β from our own heat capacity data, which was obtained by doing a linear fit to the data in the region $T/T_c < 0.25$, shown in the inset in Figure 4.11. The error of β is generated by the fitting routine.

x	β (mJ/mol K^4) from measurement down to 2 K [20]	β (mJ/mol K^4) from own measurements and other sources down to 0.5 K or lower
0	2.68	2.43 [124]
0.25	3.03	-
0.5	4.93	3.89 ± 0.02
0.75	8.98	5.46 ± 0.08
0.85	-	4.84 ± 0.04
0.9	8.98	-
0.95	9.31	-
1	8.35	3.07 [140]

Table 4.4 Phonon heat capacity of $(Ca_xSr_{1-x})_3Rh_4Sn_{13}$, extracted from [20, 124, 140] as well as our own heat capacity data. The values of β differ significantly for $x = 1$. This is possibly due to the different functional forms used by Yu et al. and Hayamizu et al. to fit the data. Hayamizu et al. also measured down to much lower temperatures (0.4 K) than Yu et al. (2 K).

The discrepancy between the two sets of data could be attributed to the different fitting methods employed. Yu et al. fitted the normal state heat capacity data from 2 to 7 K to the

functional form [20]

$$C_n(T) = \gamma T + \beta T^3 + \kappa \frac{e^{\Theta_E/T}}{\left(e^{\Theta_E/T}-1\right)^2}\left(\frac{\Theta_E}{T}\right)^2, \tag{4.3}$$

where the first and last terms correspond to the electronic and soft optical phonon contributions. We, on the other hand, assumed that these contributions would be frozen out at $T/T_c < 0.25$ and fitted the data only to βT^3. Nonetheless, at the lowest temperatures, the general trend of increasing phonon heat capacity near the quantum critical point remains. In the right-hand column, β increased by about a factor of 2 going from $x = 0$ to 0.75. Interestingly, the temperature dependence of these phonons at $x = 0.75$ and 0.85 remains T^3, as we have seen in Section 4.3.2. The low-frequency dispersion of the acoustic modes of $Sr_3Rh_4Sn_{13}$ and $Ca_3Rh_4Sn_{13}$ from the DFT calculation shown in Figure 4 of [18] are virtually identical. The same is true for the calculations of $Sr_3Ir_4Sn_{13}$ and $Ca_3Ir_4Sn_{13}$ in Figure 4 of [103], as well as our own phonon calculations shown in Figure 4.5 and 4.7. This would suggest that the heat capacity of the acoustic modes is constant across the phase diagram and the additional heat capacity is due to the soft optical modes. However, below the structural transition temperature, the zone edge soft optical branch folded back to the zone centre. Much like the 105 K antiferroic transition in $SrTiO_3$ [42], the soft optical branch could interact with the acoustic branch (see Figure 4.3), suppress its frequency and speed of sound and result in higher heat capacity.

The heat capacity values used for calculation of mean free path are from the right-hand column of Table 4.4, using linear interpolation to estimate the heat capacity for $x = 0.25$ and 0.9. The volumetric heat capacity is calculated by dividing by the molar volume of 2.8313×10^{-4} m^3/mol.

In Section 4.2, we found that the speed of sound of the shallower acoustic branches of $Sr_3Rh_4Sn_{13}$ is about 1903 m/s and the steeper acoustic branch has a gradient that is approximately 3816 m/s. The shallower branch should dominate thermal conductivity since the heat capacity is inversely proportional to the cube of the Debye temperature, which in turn is proportional to the speed of sound. As a check, we also estimated the speed of sound of the acoustic branch v_a from the Debye temperature Θ_D and the Debye wave-number q_D using the equation [139]

$$v_a = \frac{k_B \Theta_D}{\hbar q_D}, \tag{4.4}$$

where $q_D = \left(\frac{6\pi^2}{V_c}\right)^{\frac{1}{3}}$ and V_c is the volume of the unit cell divided by the number of atoms in the unit cell. For $\Theta_D = 252$ K [124] and an I' phase lattice constant of 19.5714 Å [18], we obtain a speed of sound of 2422 m/s. This is slightly higher than DFT values, which is reasonable since we ignored the steeper acoustic branch. For the following calculations, the speed of sound of 1903 m/s will be used.

Using the above values for heat capacity and speed of sound, our thermal conductivity data and Equation 2.27, we can compute the normalised phonon mean free path, which is shown in Figure 4.19. The maximum mean free path $l_{\max}$ used in the normalisation is the diameter of a cylindrical sample with the same cross-sectional area as the real sample [141]. This is defined as

$$l_{\max} \sim 2\sqrt{tw/\pi}, \tag{4.5}$$

where t and w are the thickness and width of the real sample respectively. Table 4.5 shows the values of $l_{\max}$ of the samples. Given that the individual fractional errors in t and w is about 5%, the fractional error in $l_{\max}$ is about $\sqrt{2}/2 \times 5\% \simeq 3.5\%$. This representation gives us a better understanding of the differences between the samples. For the $x = 0$ sample, $l/l_{\max}$ is close to 1 and is practically constant for $T/T_c < 0.25$. Similar results were observed in tantalum below its superconducting transition temperature [79]. Therefore, it is reasonable to expect that l for this sample is limited by boundary scattering and is hence temperature independent. The other samples have normalised mean free paths that have a power law temperature dependence for $T/T_c < 0.25$ and the mean free paths for this temperature range are less than $l_{\max}$.

4.4 Discussion

Before moving on to discuss various theoretical explanations, we will summarise the main experimental results.

1. The low-temperature ($T/T_c < 0.25$) thermal conductivity can be presented as a power law whose exponent varies from about 3 for $x = 0$ to down to about 1.7 for $x = 0.75$ near the quantum critical point.

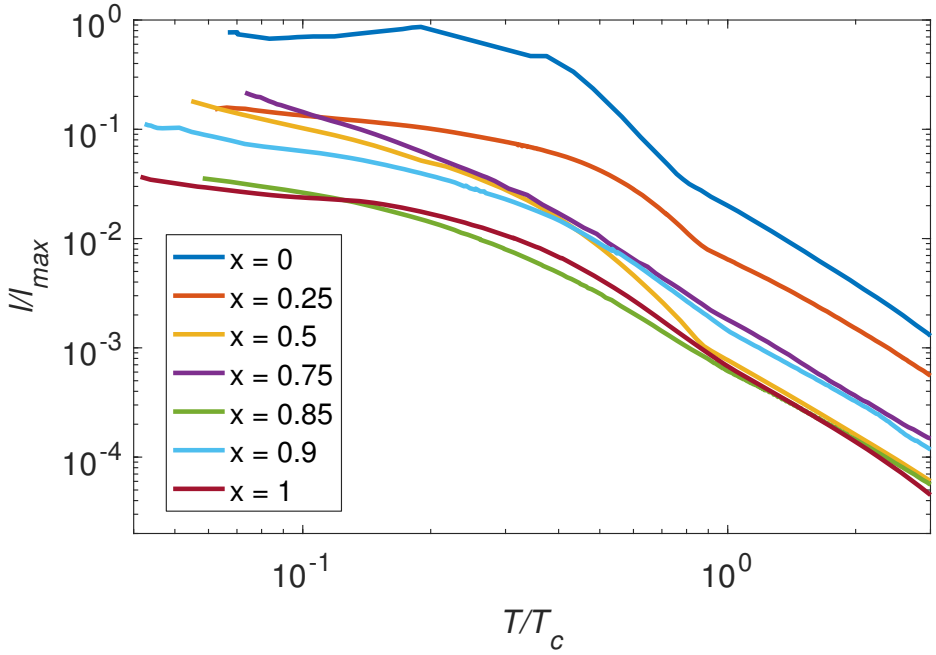

Fig. 4.19 The normalised phonon mean free path $l/l_{\max}$ of $(Ca_xSr_{1-x})_3Rh_4Sn_{13}$ where $l_{\max}$ is the maximum possible mean free path. It is of the order of the linear dimension of the sample and is tabulated in Table 4.5. Only the $x = 0$ sample has reached a constant l at the lowest temperatures.

x	$l_{\max}$ (μm)
0	237 ± 12
0.25	109 ± 5
0.5	282 ± 14
0.75	117 ± 6
0.85	246 ± 12
0.9	127 ± 6
1	182 ± 9

Table 4.5 The maximum possible mean free path $l_{\max}$ of $(Ca_xSr_{1-x})_3Rh_4Sn_{13}$ samples assuming diffuse scattering at the boundaries, determined from sample dimensions.

2. The heat capacities for samples $x = 0.75$ and 0.85 are essentially T^3.

3. The mean free paths for all samples other than $x = 0$ are smaller than the effective dimension of the sample and hence are not boundary limited.

One plausible reason for the anomalous thermal conductivity is that the samples have domains of varying x, leading to a distribution of superconducting transition temperatures. Depending on the exact distribution of T_c, one can in principle construct the observed temperature dependence. However, such a scenario will manifest as a very broad jump in heat capacity and magnetic susceptibility at T_c. In Figure 4.11, the heat capacity jump at the transition temperature is fairly sharp for all samples. The same is true for the susceptibility measurement in Figure 4.10. These measurements together can rule out the scenario of a broad T_c distribution.

4.4.1 Phonon scattering mechanisms

We will now review the behaviour of various well-known phonon scattering mechanisms and consider if they are applicable to this problem.

- *Umklapp scattering.* The treatment of lattice vibrations relies on the harmonic approximation (cf. Section 2.3.1). This assumes that the dominant term in the Taylor expansion of the lattice potential in atomic displacement is the quadratic term. However, we need to remember the importance of the higher order anharmonic terms. When they are treated perturbatively, the cubic, quartic and higher order terms represent three-phonon, four-phonon and higher number phonon scattering processes. In the three-phonon case, momentum and energy conservation dictates that

$$\begin{aligned} \mathbf{q}_1 + \mathbf{q}_2 &= \mathbf{q}_3 + \mathbf{g} \\ \omega_{\mathbf{q}_1} + \omega_{\mathbf{q}_2} &= \omega_{\mathbf{q}_3}, \end{aligned} \tag{4.6}$$

  where $\mathbf{q}$ and $\omega_{\mathbf{q}}$ are the phonon wavevector and frequency respectively and $\mathbf{g}$ is a reciprocal lattice vector. Scattering processes where $\mathbf{g} = 0$ are known as normal processes and they do not contribute to thermal resistance since they do not disrupt the heat flux [62, 135]. Processes where $\mathbf{g} \neq 0$ are known as umklapp processes and they represent the transfer of momentum from the phonons to the entire crystal. For most materials,

umklapp processes are exponentially frozen out below half of the Debye temperature due to the lack of phonon modes with high wavevectors [135]. For the $A_3T_4Sn_{13}$ materials, however, this might not be the case because of the presence of the soft optical modes. This will be discussed in further detail later.

- *Point defect and isotope scattering.* The presence of impurities and isotopes with masses that are different from their neighbours at length scales much smaller than the typical phonon wavelength at low temperatures produces scattering similar to Rayleigh scattering, with a scattering probability that is proportional to q^4. Using the simple dominant phonon analysis at low temperatures, the dominant phonon has a wavevector that is proportion to T. Hence, the scattering probability goes as T^4 and $\kappa \sim T^{-1}$ [135, 142].

- *Dislocation scattering.* Dislocations, also known as line defects, are one-dimensional defects in the crystal. Unlike point defects, the main contribution to thermal resistance is not from the core of the defect but the strain field surrounding the core that has a much larger spatial extent. There is a change in the speed of sound in the strained region which acts to refract incoming phonons and reduce the heat flux. The scattering probability is proportional to q and in the dominant phonon picture, proportional to T. This gives a thermal conductivity which goes as T^2 [135]. However, changing the amount of strain changes the coefficient of the thermal conductivity temperature dependence but not the power law exponent, which remains proportional to T^2 as seen in an experiment on Cu-Zn alloys [143].

- *Boundary scattering.* At low temperatures, as other scattering mechanisms are frozen out, the mean free path of phonons l increases until it is comparable to the dimensions for the sample. For a cylindrical sample, according to Casimir theory, the maximum l is approximately the diameter of the sample [144]. When this limit is reached, l becomes temperature independent and κ will be proportional to the heat capacity $C \propto T^3$ [135]. However, in samples with highly polished surfaces, it is possible for phonons to be specularly instead of diffusively reflected at the surface and l is larger than the diameter of the sample, and the exponent of the power law could be reduced slightly. For example, the T^3 power law observed in Al_2O_3 with rough surfaces is reduced to $T^{2.77}$ in samples with optically smooth surface [145]. In samples with smooth surfaces, the phonon mean free path at the lowest temperatures is significantly (up to a factor 4) greater than the predictions of Casimir theory. Similar low power-law exponents have also been observed previously in LiF [138] and Nd_2CuO_4 [146],

and have been attributed to specular reflection off the surface of the sample.

Boundary scattering is the most likely mechanism to explain the T^3 temperature dependence of κ for the $x = 0$ sample, but it cannot be the dominant scattering mechanism for the rest of the samples. The low power law exponent cannot be explained by specular reflection at the surface. This scenario is ruled out by the fact that the mean free path is smaller than the effective dimension of the sample and by the $x = 0.5$ and 0.75 samples with different surface treatments (see Figure 4.18).

Since our tuning parameter in this system is the substitution of Sr by Ca, we will have a large amount of scattering due to mass inhomogeneities. One might suspect that this is related to the anomalous thermal conductivity but we will show that this is not the case. We expect the mass inhomogeneities due to the random placement of Ca and Sr atoms to appear on length scales of several I phase lattice constants since there are six Sr/Ca atoms per unit cell in the I phase. We will compare this length scale to the wavelength of the dominant acoustic mode at 1 K. The frequency of the dominant acoustic mode at a given low temperature is $f = k_B T/h$ and its wavelength is

$$\lambda = \frac{v_a}{f} = \frac{v_a h}{k_B T}. \tag{4.7}$$

Using the speed of sound $v_a = 1903$ m/s found in Section 4.2, we get a wavelength of about 91 nm. This is more than 90 I phase lattice constants. This implies that mass inhomogeneities due to chemical substitution can be treated as point defects and cannot explain the anomalous power laws.

Scattering from line defects gives a T^2 power law which describes the $x = 0.5$ sample well but not the other samples since the exponent is independent of the amount of strain [135, 143]. Therefore, the results that we have obtained cannot be explained by conventional phonon scattering off of line defects. Hence, we are left with the possibility of phonon-phonon umklapp scattering that is usually frozen out at low temperatures in other materials but could possibly be active in our materials because of the soft optical modes. We will explore this possibility in detail below.

4.4.2 Umklapp scattering

Unlike most systems where zone edge modes have frequencies comparable to or higher than the Debye frequency and hence are exponentially suppressed at low temperatures, the soft optical modes at the M points, as seen in the DFT calculation in Figure 4.7, are potentially thermally accessible at the lowest temperature close to the quantum critical point since the frequency goes to zero. However, these high wavevector optical modes are much more strongly scattered by point or line defects in the crystal [135] and hence most of the lattice heat conduction should be due to the acoustic modes at low temperatures. If we hypothesise that the acoustic modes are mainly scattered via phonon-phonon umklapp processes by the soft optical modes, then it is conceivable that the acoustic phonon mean free path has a power law dependence as the scattering phase space shrinks with temperature. In this section, we will calculate thermal conductivity when phonon-phonon umklapp scattering is dominant using the Boltzmann transport theory outlined in Section 2.5 and in Chapter VIII of [62]. All frequency and energy quantities are expressed in units of temperature (in K) such that $\hbar = k_B = 1$.

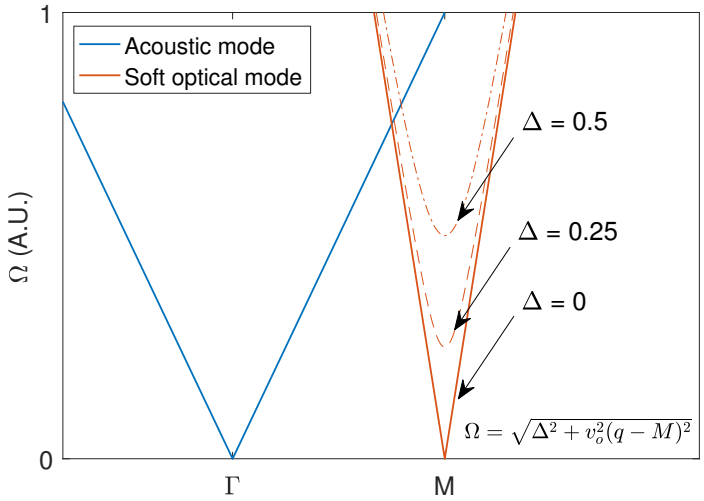

Fig. 4.20 A cartoon of a very simple phonon spectrum showing only the acoustic and soft optical phonon branches. The frequency of the phonon branch is Ω and Δ is the frequency of the soft mode.

From Equation 8.2.13 of [62], the thermal resistivity is given by

$$1/\kappa \propto \frac{1}{T^2C^2} \int d\mathbf{q}_1 \int d\mathscr{S}\, n^0_{\mathbf{q}_1} n^0_{\mathbf{q}_2} (1 + n^0_{\mathbf{q}_3}) q_1 q_2 q_3, \tag{4.8}$$

where $\mathbf{q}_1$, $\mathbf{q}_2$ and $\mathbf{q}_3$ are three phonon wavevectors like in Equation 4.6, C is the heat capacity and $n^0_{\mathbf{q}} = 1/\exp(\hbar\omega_{\mathbf{q}}/k_BT - 1)$ is the equilibrium phonon distribution. The integrals $d\mathbf{q}_1$ and $d\mathscr{S}$ are taken over the three-phonon wavevector space and all phonon modes, constrained by energy and momentum conservation in Equation 4.6. This expression is a possible solution to the Boltzmann equation using the simplest trial function that satisfies the condition of vanishing thermal resistance for normal processes. We have solved this numerically to obtain the thermal conductivity of acoustic phonon modes scattered by soft optical modes. This model is shown as a cartoon in Figure 4.20. The integral of $d\mathbf{q}_1$ is constrained to the acoustic branch and $d\mathscr{S}$ the optical branches centred on the M points in the Brillouin zone. The cutoff wavevector is half the length of the reciprocal lattice vector. The phonon dispersions for the acoustic (Ω_a) and optical (Ω_o) branches are

$$\begin{aligned} \Omega_a &= v_a q \quad \text{and} \\ \Omega_o &= \sqrt{\Delta^2 + v_o^2 (q - M)^2}, \end{aligned} \tag{4.9}$$

where $\Delta \sim 2\sqrt{|T - T^*|}$ is the frequency of the soft mode estimated from the inelastic neutron scattering shown in Figure 4.2. The speed of sound v_a for the acoustic branch is 2000 m/s, and the results are shown for several v_o.

Figure 4.21 shows the results of the calculation at the critical point of $T^* = 0$ ($\Delta = 0$) plotted for arbitrary units of thermal conductivity as a function of temperature. The thermal conductivity follows a power law, but the exponent ranges from 3.6 to 4, which is very different from the experimental observation.

A conceivable reason for the failure of this theory is that we have neglected the finite linewidth of the soft optical modes due to anharmonic coupling to other modes. Under the harmonic approximation, lattice vibrations have no damping and are perfectly oscillatory in time. In frequency space, this is represented by a Dirac delta function with zero linewidth. However, anharmonic effects which are treated as phonon-phonon scattering introduce a finite lifetime to the lattice vibrations and modulate the oscillations in time with an exponentially decaying envelope. The Fourier transform of that is a Lorentzian function with a finite linewidth. As seen in Figure 4.2 reproduced from [22], the linewidth close to the critical point is comparable to the centre frequency. In the next section, we will develop a phenomenological model that better describes the experimental observations.

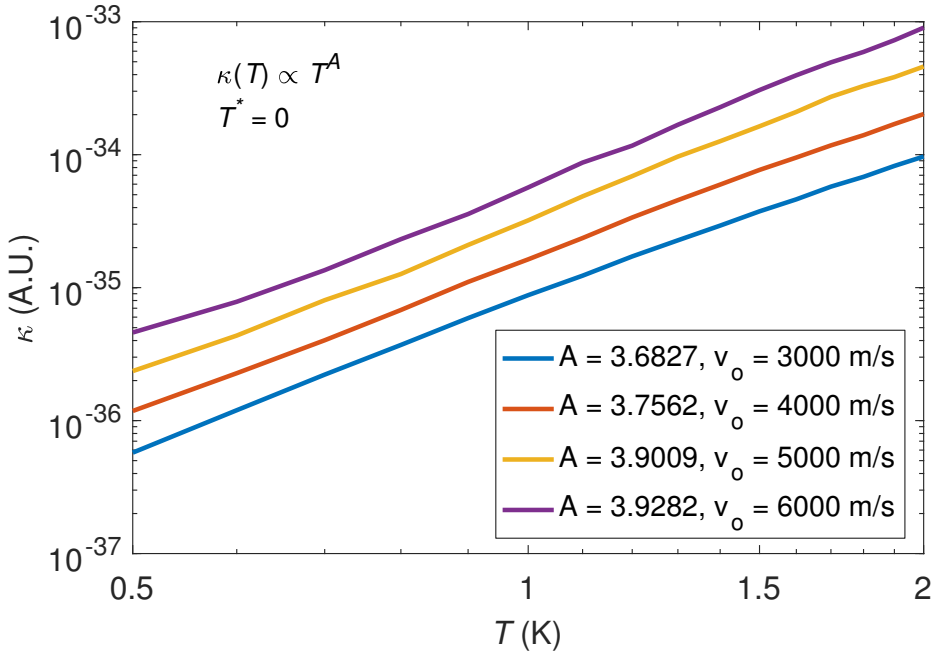

Fig. 4.21 Temperature dependence of thermal conductivity of the acoustic phonon modes limited by umklapp scattering between 0.5 and 2 K, for several v_o.

4.4.3 Phenomenological model

We will now try to build a phenomenological model that improves upon the previous umklapp scattering model. This model was constructed with help from Gilbert Lonzarich and we will refer extensively to his book chapter [30]. Similar to the previous model, we assume that the acoustic modes are responsible for all the thermal conductivity and they have conventional T^3 heat capacities. They are scattered by fluctuations in the order parameter present due to proximity to the structural transition and the mean free path is inversely proportional the scattering rate, $l \sim \Gamma_{ph}^{-1}$. We will be using methods described in Section 2.1 and in [30], and the order parameter ϕ is taken to be the set of average atomic displacements associated with the structural transition. We will adopt the hypothesis that the dominant acoustic phonon scattering mechanism at low temperatures is proportional to the variance of the order parameter. The spatial and temporal fluctuations of the order parameter are captured by the soft optical phonon mode. Instead of focusing on the Taylor expansion of the free energy, we will look at the expansion of the inverse susceptibility, $\chi^{-1}(q,\omega)$, where $q = 0$ is the M point. Like in the previous section, all frequency and energy quantities will be expressed in units of temperature. The inverse susceptibility can be expanded in powers

of frequency ω and wavevector q:

$$\begin{aligned} \chi^{-1}(q,\omega) &= \Omega^2 - i\gamma\omega - \omega^2 \\ \Omega^2 &= \Delta^2 + v_o^2 q^2. \end{aligned} \tag{4.10}$$

The parameters Δ, v_o and γ are to be determined and are in general functions of temperature. The susceptibility is mathematically identical to the response function of a damped harmonic oscillator if we interpret Ω and γ as the natural frequency and the damping constant respectively. Indeed, the physical motivation behind our phenomenological model is that the fluctuations of the order parameter can be described by a damped harmonic oscillator. With this interpretation, $\Omega = \sqrt{\Delta^2 + v_o^2 q^2}$ is the phonon dispersion of the soft mode that goes to zero at the phase transition. This model is very similar to the model described by Equation 4.79 of [147] using the renormalisation group approach. One basic requirement of this hypothesis is that the phonon mean free paths for all samples other than $x = 0$ have power law temperature dependences and they must be less than the effective dimension of the samples. This is consistent with what we have observed in Section 4.3.5.

From our hypothesis, the scattering rate of the acoustic phonons, Γ_{ph}, by the fluctuations in the order parameter field is proportional to its thermal variance, which is in turn given by the fluctuation-dissipation theorem [30]

$$\Gamma_{ph} \propto \langle \phi^2 \rangle = \frac{2}{\pi} \int_0^{\omega_c} d\omega \int_0^{q_c} d\mathbf{q}\, n_B(\omega, T)\, \mathrm{Im}\, \chi(q,\omega), \tag{4.11}$$

where $n_B = 1/(\exp(\omega/T) - 1)$ is the Bose-Einstein distribution. The imaginary part of the susceptibility is

$$\mathrm{Im}\, \chi(q,\omega) = \frac{\gamma\omega}{\gamma^2\omega^2 + (\Omega^2 - \omega^2)^2}. \tag{4.12}$$

We will estimate the temperature dependence of the phonon scattering rate, Γ_{ph}, at the critical point of $T^* = 0$ to see if it can reproduce the same experimental power law exponent. We can obtain crude estimates of the parameters Δ and γ from the inelastic neutron scattering experiment [22] (reproduced in Figure 4.2) and v_o from our DFT calculations. From Figure 4.2(b), we extract from the curve $\Delta(T) \sim 2\sqrt{|T - T^*|}$, similar to the analysis in Section

4.4.2. The parameter γ can be estimated from the full width at half maximum (FWHM) of the energy scans to be between 2–15 K and it increases as the transition is approached, though it is hard to find its exact temperature dependence. For our model, we will use a constant, temperature independent γ and $v_o = 2400$ m/s (see Table 4.1). We will show that the predictions of this model are quite insensitive to the exact values of γ within a certain reasonable range.

The integral in Equation 4.11 is solved numerically with cutoffs ω_c of 300 K and q_c of half the reciprocal lattice vector. The results are shown in Figure 4.22 for a few different values of γ. They are fitted to power laws and the exponents are extracted. We find that while the magnitude of the scattering varies significantly with γ, the value of the exponent varies only a little, approximately between 1.5–1.6. This means that the mean free path is approximately $l \sim T^{-1.5}$ and with a conventional T^3 heat capacity, $\kappa \sim T^{1.5}$. This is broadly consistent with the thermal conductivity power law exponent observed close to the critical point.

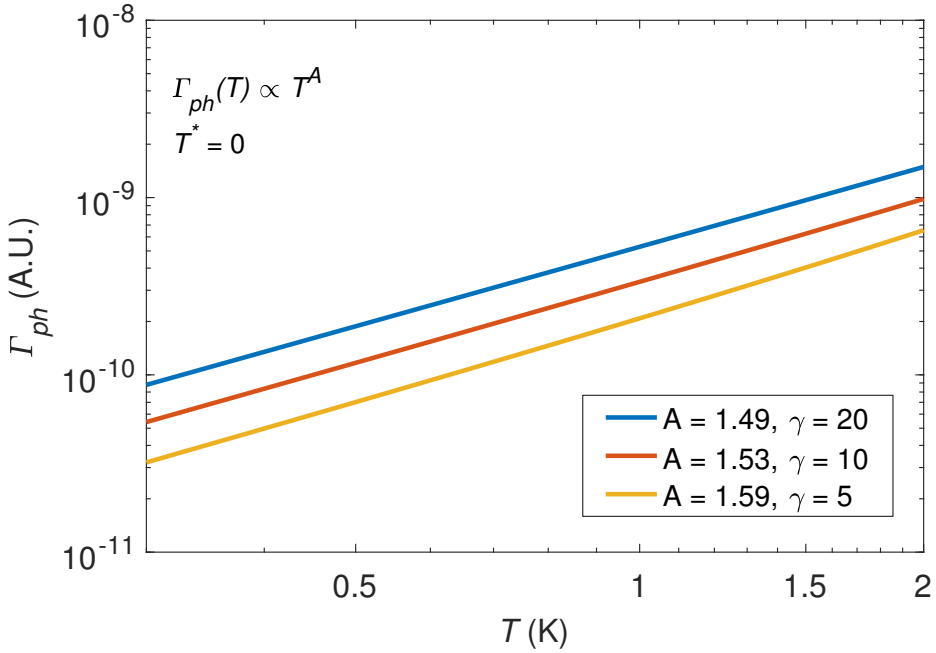

Fig. 4.22 Low-temperature acoustic phonon scattering rate due to fluctuations in the order parameter calculated from the phenomenological model for several values of γ.

While this model reproduced the thermal conductivity power law exponent near the structural critical point, we need to check what the contribution to heat capacity due to the order parameter fluctuation is. The entropy of the fluctuations is modified by damping and at a

certain frequency ω and wavevector q is given by [30]

$$S = S_\omega \left(\mathrm{Im} \frac{\partial \ln \chi(q,\omega)}{\pi \partial \omega} \right). \tag{4.13}$$

The entropy of an undamped oscillator is S_ω. It is related to n_B by $T\partial S_\omega/\partial T = \omega \partial n_B/\partial T$ [30]. The heat capacity is

$$\begin{aligned} C(T) &= \int_0^{\omega_c} d\omega \int_0^{q_c} d\mathbf{q}\, T \frac{\partial S}{\partial T} \\ &= \int_0^{\omega_c} d\omega \int_0^{q_c} d\mathbf{q}\, \frac{\gamma\omega^2 \left(\omega^2+\Omega^2\right) \mathrm{csch}^2\left(\frac{\omega}{2T}\right)}{4\pi T^2 \left(\gamma^2\omega^2 + \left(\omega^2-\Omega^2\right)^2\right)}. \end{aligned} \tag{4.14}$$

Once again, Equation 4.14 is computed numerically with the same cutoffs and the heat capacity of the fluctuations is compared with that of the undamped acoustic mode shown in Figure 4.23. The same set of values for γ as Figure 4.22 is used and the speed of sound of the acoustic modes is set to $v_a = 2000$ m/s. The undamped acoustic mode has a T^3 dependence as expected and the power law exponent of the order parameter fluctuations is approximately 1. Clearly, the fluctuations have greater heat capacity contributions than the acoustic modes. However, contradictory to the predictions of the model, this T-linear contribution is not observed experimentally down to about 0.5 K as seen in Figure 4.13.

4.4.4 Intrinsic quasi-static spatial disorder

This result suggests that our phenomenological model could not capture the dynamics of the soft optical modes correctly. It is possible that the temporal fluctuations of the order parameter are slow or even quasi-static, giving rise to a very small heat capacity that is not experimentally observed. However, there could be spatial disorder which will still result in scattering of the acoustic phonon modes. The frequencies of the soft optical modes harden after the structural transition as temperature is lowered. This has been observed by neutron and Raman scattering in $SrTiO_3$ as shown in Figure 4.4 and is illustrated in a simple cartoon representation of the phonon dispersion in Figure 4.24. The thermally active optical modes are shown in solid orange-olive–coloured lines and as temperature is lowered, they

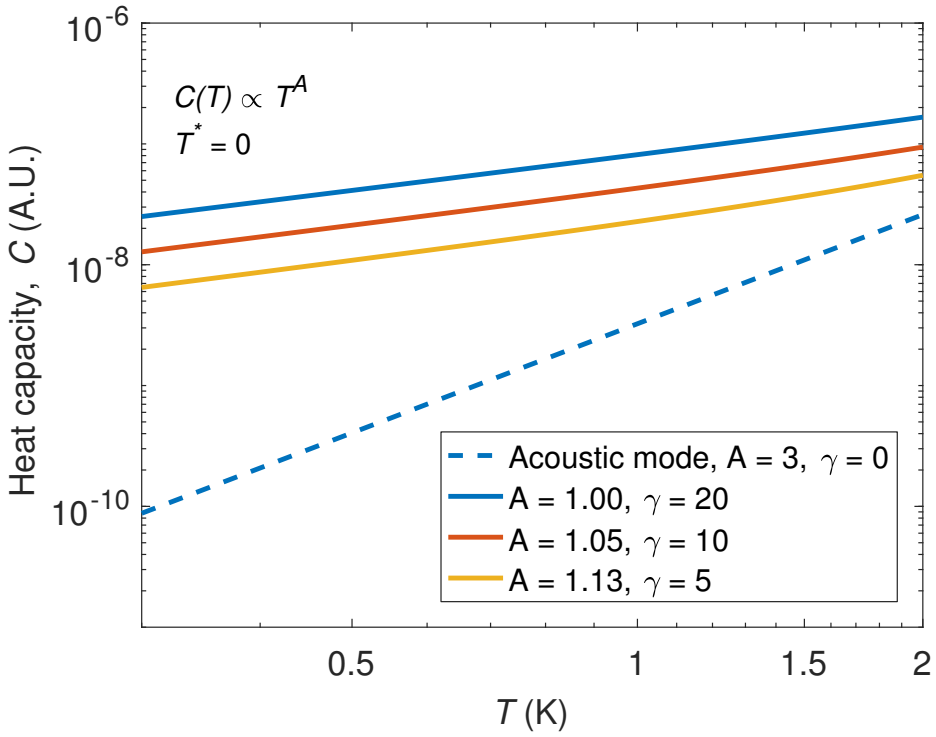

Fig. 4.23 Heat capacity of the order parameter fluctuations and the acoustic mode calculated from the phenomenological theory for several values of γ.

eventually get frozen out. Nonetheless, it is possible that their spatial modulations are frozen in, resulting in intrinsic, quasi-static spatial disorder. Since the optical branch is centred at the Γ point, any frozen-in spatial modulation will have very long wavelengths and could contribute strongly to the scattering of the acoustic modes.

If this spatial disorder is strong enough, it will destroy the long-range crystalline order of the lattice and the system will resemble a glass. In this extreme case, using the dominant phonon approximation, the mean free path will be [62, 148]

$$l \sim \frac{1}{q^2} \sim \frac{1}{T^2}. \tag{4.15}$$

This will result in T-linear thermal conductivity. Of course, our $(Ca_xSr_{1-x})_3Rh_4Sn_{13}$ system is not in this statically disordered limit, and hence we observed a thermal conductivity power law exponent between 3 and 1.7.

There is some experimental evidence supporting this quasi-static disorder picture. When measuring the single crystal x-ray diffraction patterns of $Th_3Rh_4Sn_{13}$ and several other

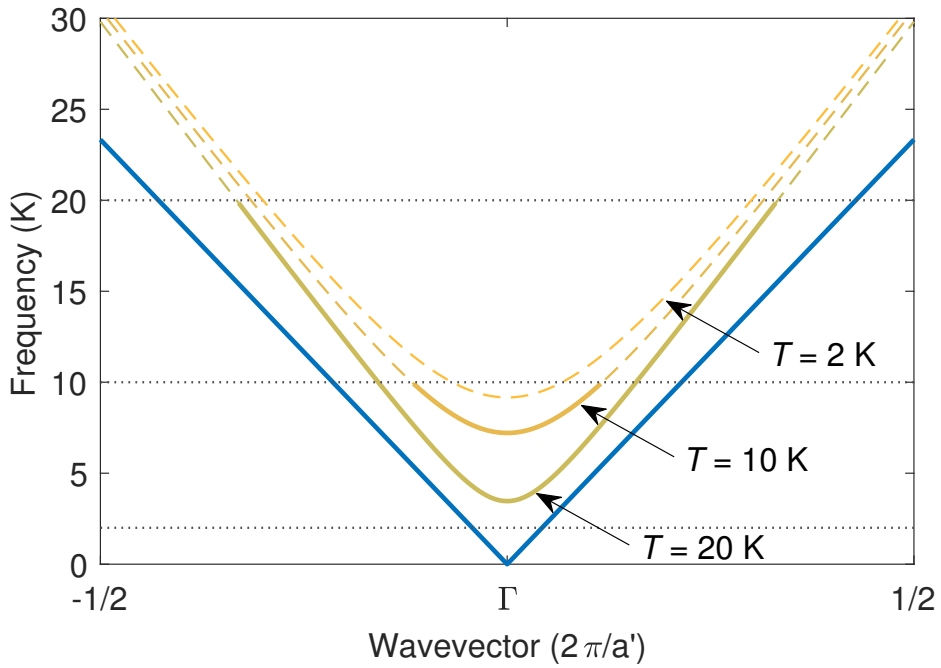

Fig. 4.24 A cartoon representation of the dispersion of acoustic (blue) and soft optical (orange-olive) branches at different temperatures. The vertical axis shows the phonon frequency in units of kelvins. The system is in the I' phase with lattice constant a' and the soft optical branch is folded back from the zone-edge M point to the Γ point. Solid-line segments of the optical branch represent thermally active modes while the dashed-line segments represent frozen modes.

$M_3Rh_4Sn_{13}$ materials, Miraglia et al. [105] discovered that unlike compounds with M = La, Ce Pr, Nd, Sm and Gd which have Bragg reflections associated with the I' phase, $Th_3Rh_4Sn_{13}$ does not have the superstructure peaks. However, the length of the major axis of the thermal ellipsoids of the Sn icosahedra of $Th_3Rh_4Sn_{13}$ is large, and this is indicative of the I' phase structure. Based on this evidence, Miraglia et al. suggested that the distortions associated with the structural transition—the order parameter—in $Th_3Rh_4Sn_{13}$ are not long range. It is possible that $Th_3Rh_4Sn_{13}$ is an extreme example where the fluctuations are large enough to completely destroy the superstructure distortions.

In conclusion, we have observed anomalous power laws with low exponents in thermal conductivity near the quantum critical point that are not observed in heat capacity. These results could not be explained by the usual scattering mechanisms. We proposed a phenomenological model which worked well to explain the thermal conductivity data, but it also predicts an anomalous contribution to the heat capacity. We then discussed the scenario of quasi-static disorder as a possible explanation. More work needs to be done in refining this model, or a more sophisticated theory is required.

Chapter 5

YFe_2Ge_2

5.1 Introduction

YFe_2Ge_2 is a strongly-correlated superconductor that has received significant attention from the condensed matter community recently because of its associations with other iron-based superconductors. It has a resistive superconducting transition temperature of about 1.8 K while the bulk transition is about 1 K [29]. In this chapter, we will explore the nature of the superconductivity in YFe_2Ge_2 using thermal conductivity and heat capacity as our primary probes.

5.1.1 Iron-based superconductors

Since we will be comparing YFe_2Ge_2 to other iron-based superconductors (FeSCs), we will first briefly review the salient features of this class of materials [10]. The structure of FeSCs consists of Fe-*A* layers, where *A* is a pnictogen or chalcogen, separated by "blocking layers" which could range from nothing (e.g. FeSe) to large perovskite layers $Sr_2(Sc,V)O_3$ (e.g. $Sr_4(Sc,V)_2O_6Fe_2As_2$ [149]). We will mainly focus our discussion on the "122" family with $BaFe_2As_2$ as the parent compound (we will refer to this family of compounds as Ba-122), which has most of the interesting properties of the FeSCs [10]. The phase diagram of the Ba-122 family, tuned by chemical substitution, is shown in Figure 5.1. $BaFe_2As_2$ is a metal with an antiferromagnetic (AFM) phase at low temperatures. The AFM transition

is coupled to a structural transition from tetragonal to orthorhombic [150]. With increasing chemical substitution, the magnetic-structural transition is suppressed and gives rise to superconductivity.

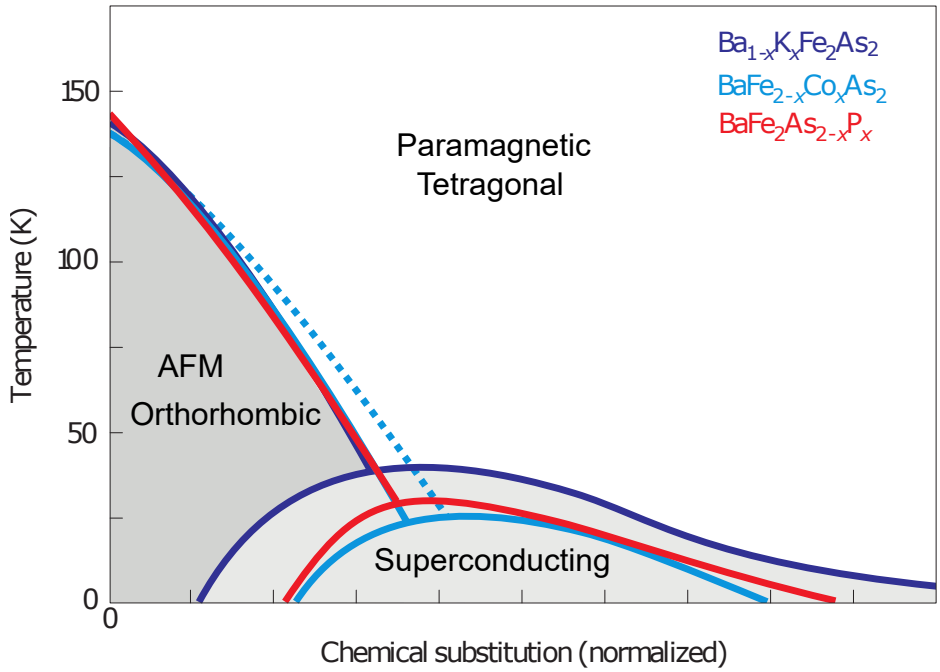

Fig. 5.1 Reproduced from [10]. This phase diagram is representative of most FeSCs.

The electronic structure of the Ba-122 family is highly two-dimensional and consists of three hole-like cylindrical Fermi surfaces centred at the Γ point (Brillouin zone centre, in the folded Brillouin zone with two Fe per cell) and two electron-like cylindrical sheets centred at the X-point (0.5, 0.5, 0) [151]. An example of this electronic structure is shown in Figure 5.2(a), calculated for $BaFe_2(As_{0.67}P_{0.33})_2$. Such an electronic structure lends itself to significant Fermi surface nesting, with **q**-vector = (0.5, 0.5, 0), which is the same wavevector as the AFM order. Indeed, the gapping out of part of the Fermi surface has been observed in $BaFe_2As_2$ and $SrFe_2As_2$ [152], and this argues for an itinerant magnetic order in the Ba-122 family. As the AFM order is suppressed, we expect the presence of strong spin fluctuations which could act as pairing glue for superconductivity.

The superconductivity in FeSCs probably has singlet spin pairing, as suggested by NMR Knight shift measurements [154]. Theoretically, it has been predicted that the pairing symmetry for FeSCs is $s_\pm$ [23]. In this model, the superconducting order parameter maintains the symmetry of the underlying lattice (hence s-wave) but changes sign between the hole-like Fermi surface at the Γ point and the electron-like Fermi surface at the X-point [10].

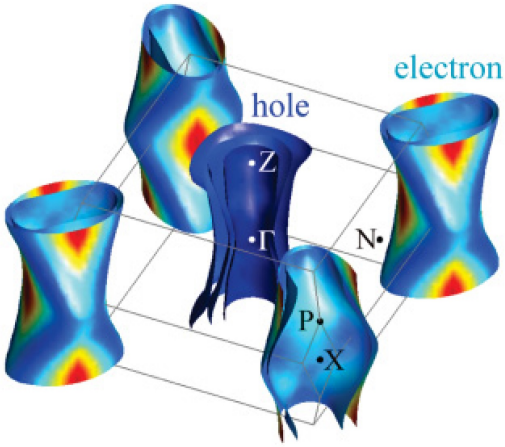

(a) $BaFe_2(As_{0.67}P_{0.33})_2$

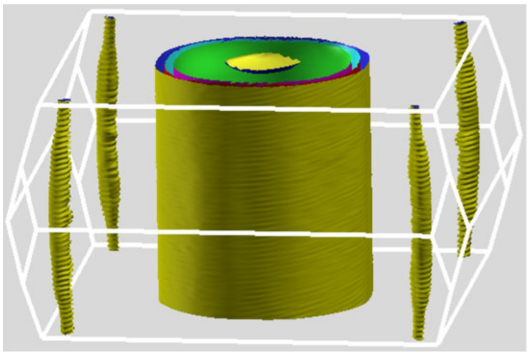

(b) KFe_2As_2 tetragonal phase

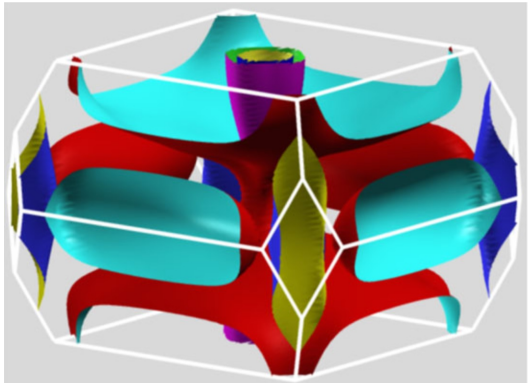

(c) KFe_2As_2 collapsed tetragonal phase

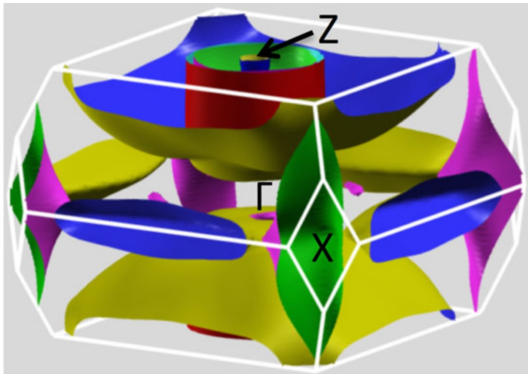

(d) YFe_2Ge_2

Fig. 5.2 Fermi surface of several FeSCs. The high symmetry points are labelled in panels (a) and (d). Panel (a) is reproduced from [153] and panels (b)-(d) are reproduced from [29]. (a) DFT calculation of optimally-doped $BaFe_2(As_{0.67}P_{0.33})_2$ with $T_c = 31$ K (b) KFe_2As_2 in the tetragonal phase (c) KFe_2As_2 in the pressured-induced collapsed tetragonal (cT) phase (d) YFe_2Ge_2

The $s_\pm$ pairing symmetry is supported by a series of phase-sensitive experiments for FeSCs near optimal doping with relatively high T_c's. A scanning SQUID measurement of polycrystalline $NdFeAsO_{0.94}F_{0.06}$ ($T_c = 48$ K) found no signs of half-integer flux-quantum, which would be generated by spontaneous orbital currents in a polycrystalline d-wave superconductor [155]. An unconventional phase-sensitive experiment using a loop made with a Nb wire and a polycrystalline $NdFeAsO_{0.88}F_{0.12}$ ($T_c \sim 50$ K) sample found half-integer flux-quantum jumps that could only be observed if the current experiences π phase shifts across some grain boundaries [156], and is hence incompatible with a simple s-wave (without sign change between bands) superconducting order parameter. Finally, the Josephson effect has been observed between the c-axis of $Ba_{1-x}K_xFe_2As_2$ (with $x = 0.29$ and 0.49, T_c of 29 K and 26 K) and Pb, a conventional s-wave superconductor, which should rule out a pure d-wave symmetry since in that case, the Josephson currents will cancel [157].

Thermal conductivity measurements of $Ba_{1-x}K_xFe_2As_2$ ($x = 0.25$, 0.28, $T_c = 26$ K, 30 K) seems to support the $s_\pm$ pairing picture because the residual T-linear thermal conductivity term, κ_0/T, is negligible [24] (cf. Section 2.5.1). However, the magnetic field dependence of κ_0/T at low fields is much stronger than the typical exponentially-activated behaviour of an isotropic s-wave, leading to the conclusion that there must be strong anisotropy in the gap structure [24]. The strength of this anisotropy seems to increase as the system is tuned away from the parent $BaFe_2As_2$ compound, as demonstrated in the thermal conductivity of $BaFe_{2-x}Co_xAs_2$ with $x = 0.048$, 0.074, 0.108 and 0.114 ($T_c = 17.1$, 22.2, 14.6 and 10.1 K) [158]. Similar to the previous experiment, no κ_0/T is observed at zero field. In field, the rate of thermal conductivity enhancement increases rapidly with x from the typical field dependence of a fully-gapped isotropic s-wave to a strongly anisotropic s-wave with deep minima that is almost nodal-like [158]. Finally, for some FeSCs like KFe_2As_2 ($T_c = 3$-4 K) [25, 77, 159], LaFePO ($T_c = 7.5$ K) [87] and $BaFe_2(As_{1-x}P_x)_2$ ($x = 0.33$, $T_c = 30$ K) [160], there is evidence for line nodes from thermal conductivity measurements which found finite κ_0/T at zero field and strong enhancement of κ_0/T with small fields.

There are two possible reasons for the observation of line nodes in certain FeSCs. Firstly, there might be modulations of the s-wave gap that preserve the symmetry of the lattice (see Figure 2.5). If the modulations are deep enough, the gap might change sign and accidental nodes are created. These accidental nodes are either intrinsically absent in other FeSCs or they could be lifted via intraband scattering [161]. This is the explanation proposed by Sutherland et al. for LaFePO [87]. The alternative explanation, advanced by Reid et al. for KFe_2As_2 [25], is that KFe_2As_2 has a d-wave pairing symmetry. This is supported by the

observations that the measured value of κ_0/T is close to the theoretically predicted universal value for a d-wave symmetry with four line nodes and is insensitive to an order of magnitude change in impurity level (measured by residual resistivity) [25, 159]. The idea of an evolution of the pairing symmetry from s-wave to d-wave with hole-doping is supported by theoretical renormalisation-group studies [162]. However, another thermal conductivity experiment by Watanabe et al., who measured $Ba_{1-x}K_xFe_2As_2$ samples with $x = 0.76$, 0.88, 0.93 and 1, has cast doubt about the d-wave interpretation [26]. In particular, the value of κ_0/T for KFe_2As_2 was about 0.20 W/m K^2 which is significantly different from the value of 0.33 W/m K^2 measured by Reid et al.. Moreover, κ_0/T varies strongly and non-monotonically from $x = 0.88$ to 0.93 to 1, which calls into question its universality. These results are more consistent with the multiband s-wave with accidental nodes picture. The most direct evidence for an s-wave pairing symmetry comes from the laser ARPES experiment by Okazaki et al. who found strongly anisotropic gaps on each of the three hole-like Fermi surfaces around the Brillouin zone centre, one of which has eight line nodes [27]. This is clearly inconsistent with d-wave pairing symmetry. Finally, Hardy et al. fitted their heat capacity data of KFe_2As_2 to a self-consistent four-band model with s-wave gap symmetry [28] and found qualitative agreement with results from the laser ARPES experiment. The combination of these experiments strongly suggests that KFe_2As_2 has an s-wave pairing symmetry with accidental nodes.

High-quality single crystal KFe_2As_2 has been studied under hydrostatic pressure by Tafti et al. and T_c was found to vary non-monotonically with pressure, with a linear reduction from 0 to approximately 17 kbar followed by a slight enhancement from 17 to 26 kbar [163]. The same effect was observed in $RbFe_2As_2$ and $CsFe_2As_2$ at similar pressures [164]. Further increasing pressure proved to be detrimental to superconductivity in KFe_2As_2 from about 31 kbar onwards [165]. At about 160 kbar, a first-order structural transition from tetragonal to "collapsed tetragonal (cT)" phase occurs where there is a discontinuous increase (decrease) in the a-axis (c-axis) lattice constant [165, 166]. The electronic structure of KFe_2As_2 in the tetragonal and cT phase are shown in Figure 5.2(b) and (c). Just into the cT phase, Nakajima et al. observed the resistive onset of superconductivity at around 11 K [165]. Similar high-pressure measurements done by Ying et al. [167] saw full superconductivity transition in resistivity that onset at around 12 K in the cT phase. Their measurement also revealed highly oscillatory behaviour of T_c as a function of pressure before the cT phase, agreeing qualitatively with measurements by Taufour et al. [168]. A theoretical study related the superconductivity in the cT phase of KFe_2As_2 to its electronic structure which exhibits nesting between the hole (at Γ point) and electron pockets (at X-point), which is reflected as a peak

in its electronic susceptibility at that wavevector [169]. This should favour the $s_\pm$ pairing symmetry. However, it is worth noting that the existence of superconductivity in the cT phase might be highly dependent on the high-pressure experimental conditions as pointed out by Wang et al. [166], who did not observe said phenomenon.

5.1.2 YFe_2Ge_2

YFe_2Ge_2 is closely related to the Ba-122 family of FeSCs. It has the same tetragonal $ThCr_2Si_2$ structure (space group I4/mmm, crystal structure shown in Figure 5.3) [170] and by electron counting, it would be equivalent to KFe_2As_2. It has a very large Sommerfeld coefficient of between 90 and 100 mJ/mol K^2, about 8 to 10 times that of the predicted band structure value, which indicates strong electron correlations [29, 171, 172]. Moreover, an anomalous $T^{1.5}$ power law temperature dependence in resistivity below 10 K is observed, signalling the breakdown of Fermi liquid theory [173]. A similar $T^{1.5}$ power law in resistivity was observed at ambient pressure in KFe_2As_2 from 20 K down to T_c in zero field, and down to 50 mK in a field of 5 T [159]. The power law was attributed to the scattering of electrons via antiferromagnetic spin fluctuations in a three-dimensional material [159, 174]. This is reminiscent of the cubic, heavy-fermion superconductor $CeIn_3$ which has a $T^{1.6\pm0.2}$ resistivity power law [2]. Moreover, YFe_2Ge_2 has a very similar electronic structure as the cT phase of KFe_2As_2 (as shown in Figure 5.2(c) and (d)), which are much more three-dimensional compared to the other FeSCs.

Like the FeSCs, the nature of the potential magnetic instabilities in YFe_2Ge_2 is very complicated. Although no magnetic order is measured experimentally in YFe_2Ge_2 [173], it appears to be on the threshold of some form of magnetic order. Two independent DFT calculations have predicted that a variety of magnetic orders of Fe atoms, including ferromagnetic and antiferromagnetic orders with various wavevectors, all have lower energy than the non-spin-polarised (NSP) case. In particular, the A-type order, where the Fe atoms are ferromagnetically aligned in plane but antiferromagnetically aligned along the c-axis, are predicted by both studies to be the most favourable state, although the magnitude of the energy advantage as compared to the NSP scenario differs by about 7 times between them [171, 172]. These predictions are not unreasonable given that $Lu_{1-x}Y_xFe_2Ge_2$ has the A-type order from $x = 0$ to about 0.18 [175]. Recent spectroscopic work by Sirica et al. [176] has shown, through core-level photoemission spectroscopy, that Fe in YFe_2Ge_2 has

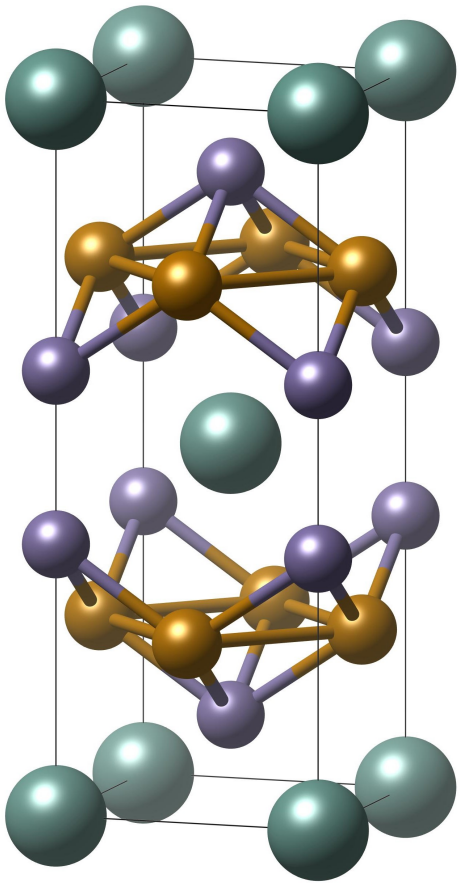

Fig. 5.3 The crystal structure of YFe_2Ge_2 with experimental lattice parameters from [173]. The teal, golden and purple spheres represent Y, Fe and Ge respectively.

an itinerant magnetic moment of order 1 μ_B. This is not inconsistent with DC magnetisation measurements which showed that YFe_2Ge_2 is non-magnetic [173] as photoemission is sensitive to magnetic fluctuations on the time scale of about 10^{-17} to 10^{-16} s [176]. This is reminiscent of previous spectroscopic measurements in other FeSCs which showed similar magnetic moments in Fe [177, 178]. In a theoretical study, Guterding et al. [179] have extracted exchange coupling constants of a two-dimensional Heisenberg model from DFT energies of $RbFe_2As_2$ and YFe_2Ge_2 as well as a few intermediate compounds smoothly interpolated with the virtual crystal approximation (VCA). VCA is a computational method which uses virtual atoms, which have properties interpolated between close-by elements in the periodic table, to model materials with disorder due to chemical substitution. They obtained the exchange coupling constants between different Fe sites and found that the near neighbour coupling J_1 went from about 20 meV (antiferromagnetic) to -20 meV (ferromagnetic). From this result and other analysis, they have concluded that the ferromagnetic interaction in the Fe planes, induced by the substitution of As by Ge and of Rb by Y, has suppressed superconductivity in YFe_2Ge_2 [179]. While this is a compelling argument, it is likely that the magnitudes of the magnetic interaction energy scales are overestimated [180]. Nevertheless, this work suggests that the type of magnetic fluctuations in YFe_2Ge_2 might be different from other FeSCs.

The crystal growth of high-quality, bulk-superconducting YFe_2Ge_2 is very challenging. Despite the presence of superconducting transitions in resistivity and magnetisation, the heat capacity anomaly, which is indicative of bulk superconductivity, was not observed in early studies of YFe_2Ge_2 [173, 181]. This prompted Kim et al. to conclude that superconductivity in YFe_2Ge_2 is filamentary and only exists under certain strains [181]. The demonstration of bulk superconductivity with heat capacity anomaly was only recently achieved with samples that have residual resistance ratios (RRR) of between 70 and 200 [29]. While the superconductivity in YFe_2Ge_2 is not filamentary, it is fragile—much like the superconductivity in the cT phase of KFe_2As_2.

5.1.3 Motivation

By performing thermal conductivity measurements as functions of temperature and magnetic field, we wish to find out more about the superconducting gap structure of YFe_2Ge_2. This will then constrain the possible pairing mechanism (e.g. phonons, spin-fluctuations) for YFe_2Ge_2. In addition, this will also tell us more about the nature of superconductivity

of KFe_2As_2 in the pressure-induced cT phase, which is harder to access with experimental probes. As we have seen previously from the electronic structure and the $T^{1.5}$ resistivity, YFe_2Ge_2 is a more three-dimensional material compared to other FeSCs. If we find evidence that the nature of superconductivity in YFe_2Ge_2 is similar to the other FeSCs with higher T_c's, we can then make a meaningful comparison of their differences, and deduce the implications for unconventional superconductivity.

5.2 Experimental results

The thermal conductivity of two samples of YFe_2Ge_2—RF34B14-1 and RF73B-S7, has been measured in zero field down to about 0.3 K here in Cambridge. These high-quality samples were grown by Jiasheng Chen using methods described in [29], and he is also credited with the heat capacity data presented here. RF34B14-1 was prepared and contacted by Ben Seddon. These samples were chosen from the RF34 and RF73 batches because of their high residual resistivity ratios (RRR) of 100 or more. The difference between the batches is that RF73 is grown with higher purity Y (99.9% for RF34 and 99.99% for RF73). In addition to the experiments done in Cambridge, our collaborators Rob Hill, William Toews and Jennifer Reid from the University of Waterloo have also measured the thermal conductivity of RF34B14-1 in a dilution fridge down to 50 mK and in fields of up to 2.5 T.

The samples are first polished down to a good geometric factor with 1000 grit sandpaper and then contacted using either 50 μm silver wire or 25 μm gold wire with Dupont 6838 silver epoxy. Making low-resistance contacts to YFe_2Ge_2 is complicated by the tendency of Y to oxidise after 30-40 min, as indicated in the recent photoemission spectroscopy experiment [176]. This can be mitigated by passing a pulse of current through the contacts after they have been cured at 200 °C for 45 mins, which will reduce the contact resistance from a few Ω to several hundred mΩ. The current pulse is sourced from a capacitive-discharge spot-welder [136] that has been charged to between 9 and 15 V. Alternatively, one could cure the 6838 silver epoxy at 450 °C for 30 minutes, which is much higher than the recommended curing temperature. This method has also produced low-resistance contacts of the order of several hundred mΩ. Having low-thermal-resistance current contacts is important because for a given heat current, the contact thermal resistance will determine the temperature difference between the sample and the measurement stage. A highly resistive contact will limit the lowest temperature at which the sample can be measured. Experimentally, we

have found that for silver epoxy contacts, the electrical resistance correlates well with the thermal resistance. The details about each sample can be found in Table 5.1.

Sample	Geometric factor (μm)	Contact resistance at 300 K (mΩ)	Preparation
RF34B14-1	21.6 ± 2.5	180 ± 20	6838 silver epoxy cured at 450 °C for 30 min
RF73B-S7	19.5 ± 1.0	140 ± 20	6838 silver epoxy cured at 200 °C for 45 min, followed by pulsing.

Table 5.1 A summary of the YFe_2Ge_2 sample preparation procedures and properties. Contact resistance refers to the combined 2-point resistance measured across the current contacts less the 4-point sample resistance measured at room temperature.

5.2.1 Resistivity

The zero-field resistivity data for the two samples of YFe_2Ge_2 is plotted in Figure 5.4. The low-temperature segment between 2 and 10 K shows a very clear $T^{1.5}$ behaviour consistent with previous reports [29, 173, 181]. The value of the residual resistivity, ρ_0, will be used to calculate the normal state electronic thermal conductivity κ_e using the Wiedemann-Franz law (WFL) $\kappa_e/T = L_0/\rho$, where $L_0 = 2.44 \times 10^{-8}$ W Ω K^{-2}. The residual resistivity of RF73B-S7 is about 40% lower than RF34B14-1, which is consistent with the fact that it was grown from higher purity Y. At 2 K, we can see the beginning of the superconducting transition, which should pass through the mid-point at around 1.83 K [29].

5.2.2 Heat capacity

Heat capacity measurements have been performed by Jiasheng Chen on relatively larger samples from both the RF34 and RF73 crystal growth batches. The results in zero field from 0.3 to 4 K are shown in Figure 5.5. The C/T temperature dependence is quite unusual because it starts to slowly rise with decreasing temperature before its peak at 1 K, which is taken to be the bulk superconducting transition. The size of the jump of the heat capacity

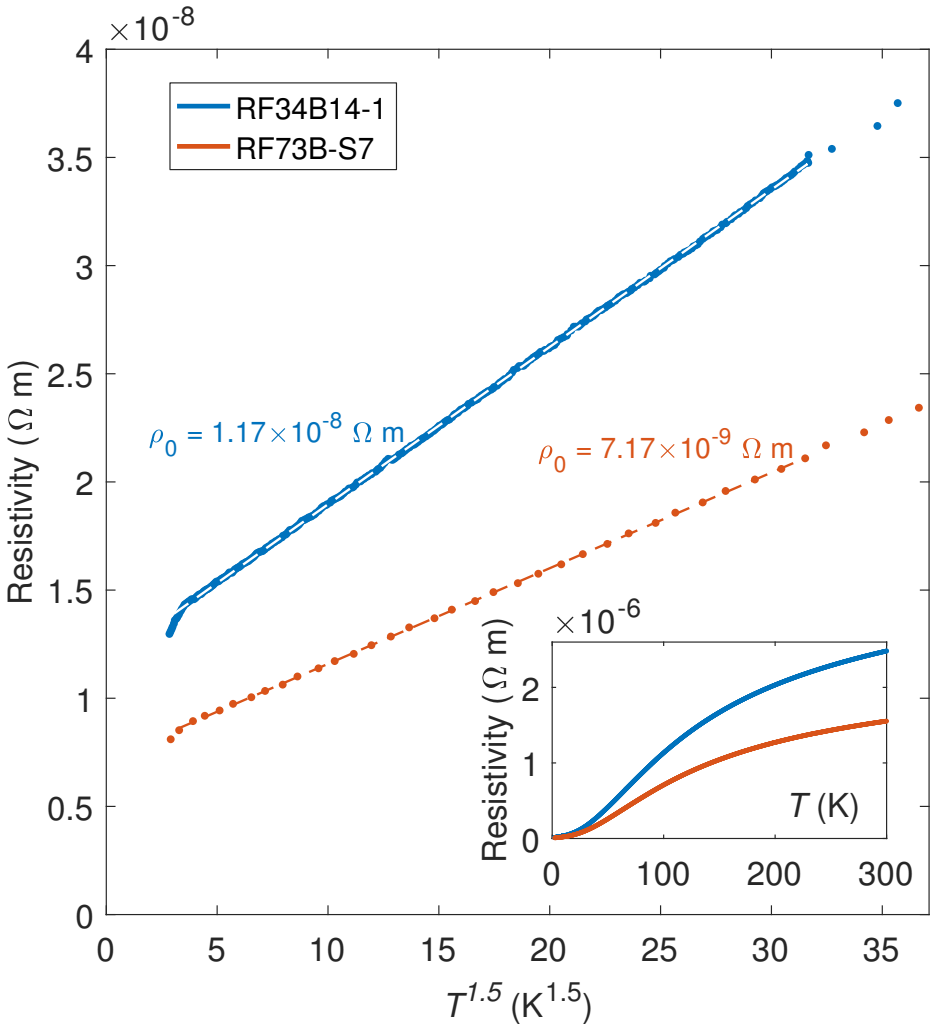

Fig. 5.4 The zero-field resistivity data of two YFe_2Ge_2 samples from 2 to 300 K measured in Cambridge. The measurement of RF34B14-1 was made by Ben Seddon. The data between 2 to 10 K fits well to $\rho(T) = \rho_0 + AT^{1.5}$. The value of the residual resistivity, ρ_0, is shown.

anomaly is also quite small, about 25 to 30% of the normal state value, much less than the BCS value for $\Delta C/\gamma T_c \sim 2.43$ [182]. However, it is comparable to the size of the heat capacity anomaly in KFe_2As_2 which is approximately 50% of the normal state value [28].

The data for RF34, which was measured up to about 20 K, is plotted as C/T against T^2 in Figure 5.6. The function $C/T = \gamma + \beta T^2$ is used to fit the data in the range of temperatures between 10 and 20 K. This is to avoid the upturn in C/T starting around 10 K. The purpose of this fit is to extract the phonon heat capacity, $\beta = 0.541$ mJ/mol K^4, to estimate the phonon thermal conductivity which will be useful for further analysis later. We can use Equation 4.2 to calculate the Debye temperature, $\Theta_D = 262$ K, which is very similar to the 280 K estimate from [183]. Dividing by the molar volume 4.95×10^{-5} m^3/mol from the lattice constants from [29], the volumetric phonon heat capacity coefficient is $\beta = 10.9$ J/m^3 K^4. The speed of sound can be estimated from Equation 4.4 to be $v_s \sim 2200$ m/s. The maximum, boundary-limited phonon mean free path, $l_{max} = 177 \pm 20$ μm, is calculated from Equation 4.5, where the width and thickness of the sample are approximately 207 μm and 119 μm respectively. The upper bound of the phonon thermal conductivity, $\kappa_{ph} \sim 1.44\ T^3$ W/m K, is estimated using the kinetic formula, Equation 2.27. This is plotted in Figure 5.9.

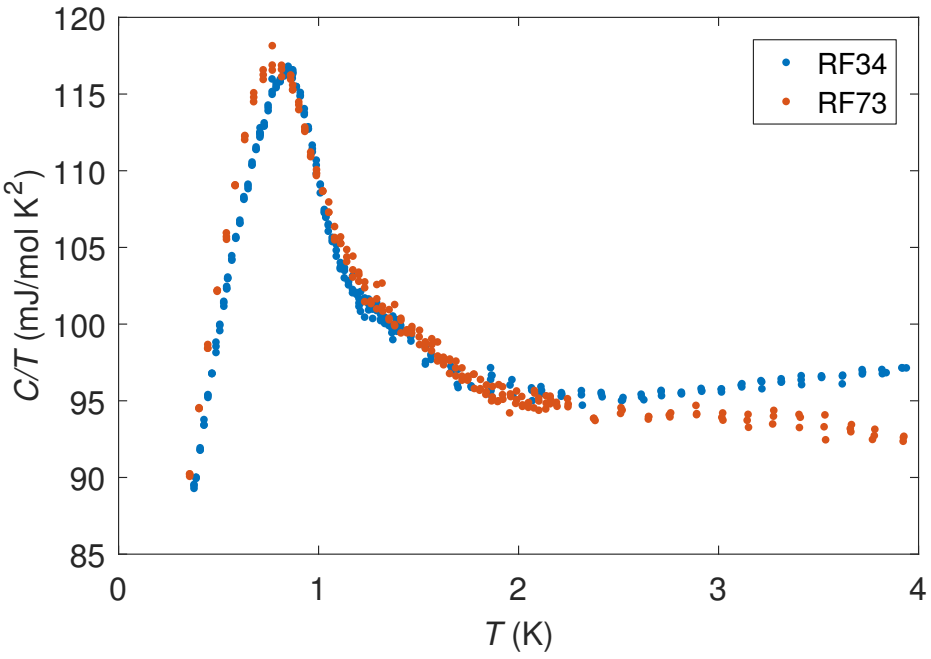

Fig. 5.5 Heat capacity data of two YFe_2Ge_2 samples measured by Jiasheng Chen from the same crystal growth batches as samples used for thermal conductivity.

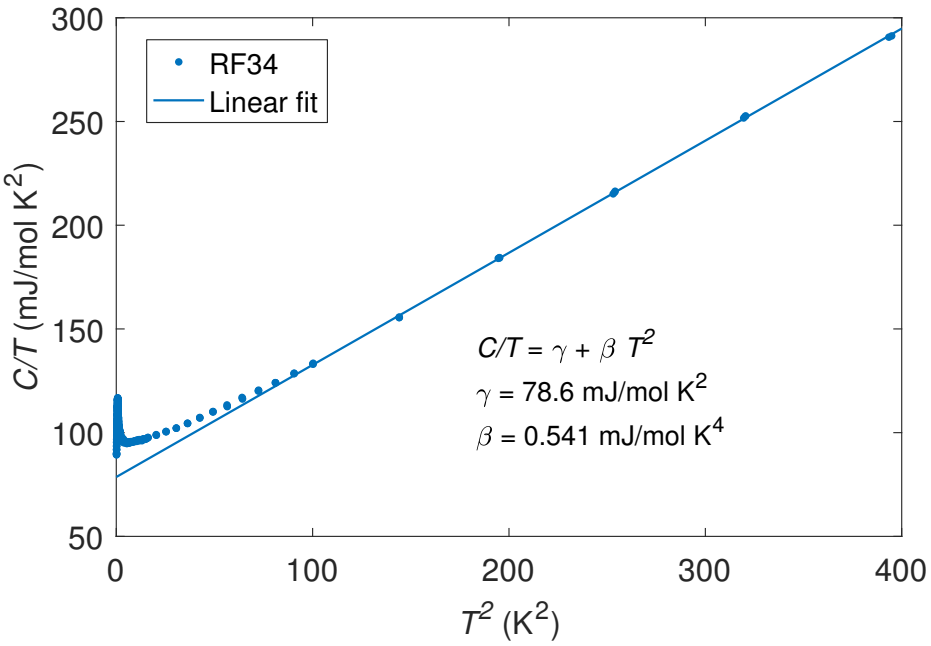

Fig. 5.6 Heat capacity data of YFe_2Ge_2 plotted as C/T against T^2. The linear fit regime is done between 10 and 20 K.

5.2.3 Thermal conductivity

The zero-field thermal conductivity data collected in Cambridge for the two samples of YFe_2Ge_2 is shown in Figure 5.7. We have measured thermal conductivity for a full range of temperatures from 0.3 to about 80 K for RF34B14-1 while for RF73B-S7, we have focused on the lower temperature range. For RF34B14-1, the small, broad peak at around 15 K is likely due to the crossover from lattice scattering at high temperatures and impurity scattering at low temperatures as the dominant mechanism for electronic thermal resistance [135]. At T_c, the thermal conductivities of the samples are reduced and no phonon thermal conductivity peak (like that shown in Figure 2.6 and Figure 4.14) is observed. This suggests that the phonon mean free path is not drastically increased when entering the superconducting phase.

The κ/T data is shown in Figure 5.8. While the temperature dependence of these samples shows similar behaviour, their absolute values vary significantly between samples. The main feature seen in both samples is a peak in κ/T at around 1 K. This approximately coincides in temperature with the peak of the superconducting heat capacity anomaly in C/T, as shown in Figure 5.5. The peak value for both samples agrees quite well with the WFL expectation indicated by L_0/ρ_0. There is a peak-like feature for RF73B-S7 at around 0.45 K and a hint

of a shoulder could be seen in RF34B14-1 at around 0.55 K. The interpretation of these features will be discussed later. While it is certainly dangerous to extrapolate the data from 0.3 K to 0 K, it is quite likely that the residual heat conduction is significantly higher for RF73B-S7 than for RF34B14-1.

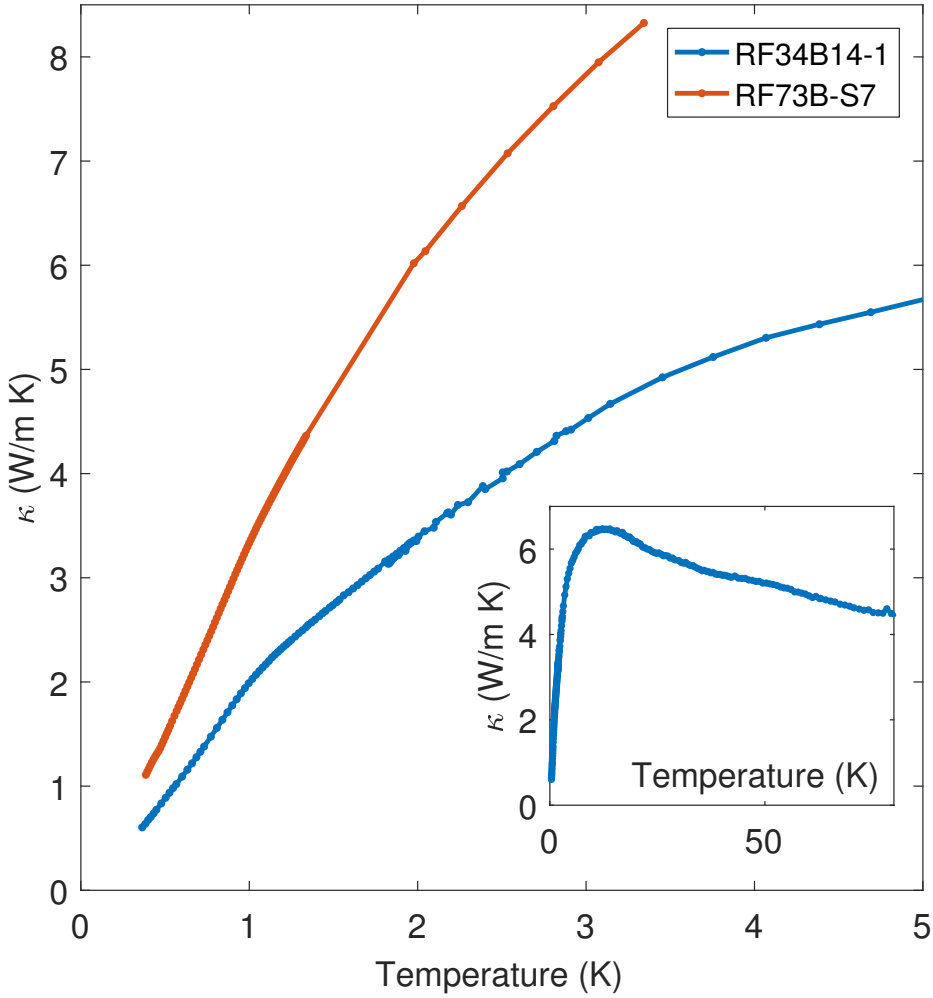

Fig. 5.7 The raw thermal conductivity between 0.3 and 5 K for YFe_2Ge_2 samples RF34B14-1 and RF73B-S7 at zero field measured in Cambridge. The inset shows the thermal conductivity data for RF34B14-1 up to 80 K.

We will now discuss the thermal conductivity measurements done in Waterloo on RF34B14-1. Their measurement technique is very similar to the steady-state measurement technique described in Section 2.5.2, but it is shielded from electromagnetic interference by a copper box [184]. In Figure 5.9, the temperature dependence of κ/T at several field values is plotted and compared with the zero-field κ/T measurement of the same sample done in Cambridge. The agreement between these two independent measurements is good and the

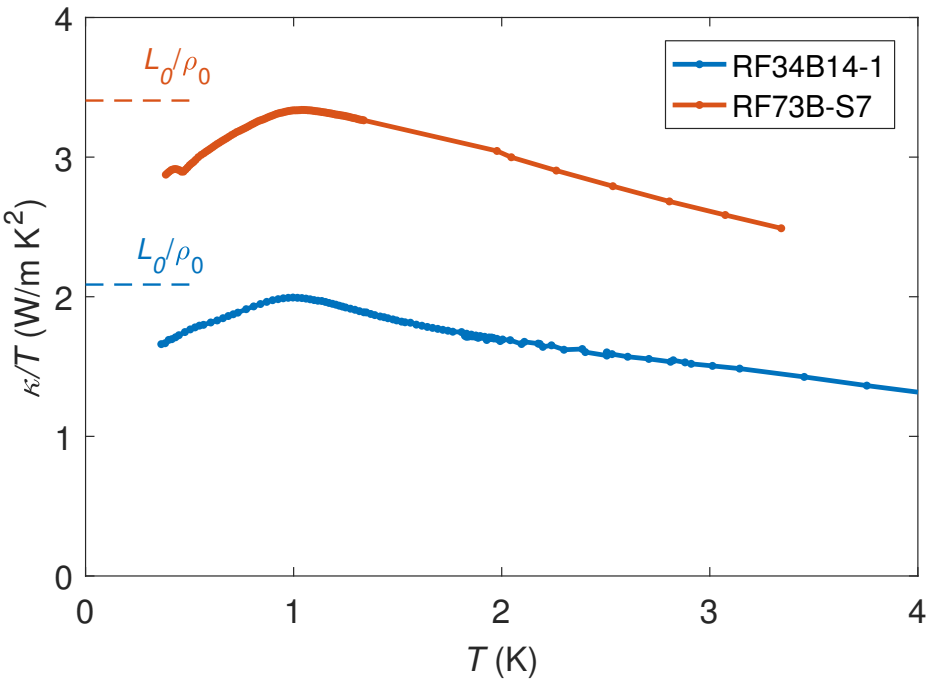

Fig. 5.8 A comparison of κ/T between YFe_2Ge_2 samples RF34B14-1 and RF73B-S7 at zero field measured in Cambridge. The values of κ/T are approaching the WFL value (L_0/ρ_0) indicated by the dashed lines before the onset of bulk superconductivity at around 1 K.

maximum difference between them is about 3.5%. The zero-field κ/T is fitted to a T-linear function as shown by the blue dashed line and the residual value, κ_0/T, is approximately 1.28 W/m K^2. The normal state κ_e/T estimated from the residual resistivity is represented by the black dashed line. This agrees well with κ/T at 2.5 T. Also shown in Figure 5.9 is the maximum phonon contribution to thermal conductivity if the phonons are limited by boundary scattering, which we have estimated from phonon heat capacity in Section 5.2.2. We can see that at temperatures lower than 0.3 K, the maximum possible phonon contribution is less than 10% of the total thermal conductivity and this ratio decreases further with decreasing temperature. Hence, we could ignore the phonon contribution and make the approximation that the residual thermal conductivity is entirely due to the electrons. In small fields of 0 to 100 mT, κ/T, from 0.05 to 0.5 K, increases rapidly with field, but is largely field independent from 0.5 to 1 K. Only at higher fields of 500 mT or more does κ/T (between 0.5 and 1 K) start increasing with field. At around 1 to 2.5 T, κ_0/T approaches L_0/ρ_0 .

In Figure 5.10, thermal conductivity is measured as a function of field. The symmetry of thermal conductivity about zero field gives us confidence that the remnant field of the magnet is insignificant. In Figure 5.11, thermal conductivity has been normalised by the normal state value at $H_{c2} = 2.3$ T [29] to show the enhancement of thermal conductivity in field. The data from the same absolute field value are averaged together. The crosses and dashed lines are interpolated and extrapolated data from the temperature scans in Figure 5.9. Also shown in Figure 5.11 is the data for the d-wave superconductor $Tl_2Ba_2CuO_{6+\delta}$ [83] and the s-wave superconductor Nb [88]. The field dependence of κ/T clearly resembles the nodal more than the fully gapped superconductor, although the residual value of κ/T is much larger than that of $Tl_2Ba_2CuO_{6+\delta}$. When plotted against $\sqrt{H/H_{c2}}$ as shown in Figure 5.12, the thermal conductivity at 100 mK and 435 mK have regions of $\sqrt{H}$ dependence. This is consistent with the Volovik effect discussed previously (cf. Section 2.5.1) and indicates a nodal gap structure. It is interesting to note that at both temperatures, there is a region of field close to zero where the thermal conductivity is essentially independent of field up to about 20 mT at 100 mK and up to about 90 mT at 435 mK. These values are much larger than the lower critical field of about 2 mT [173].

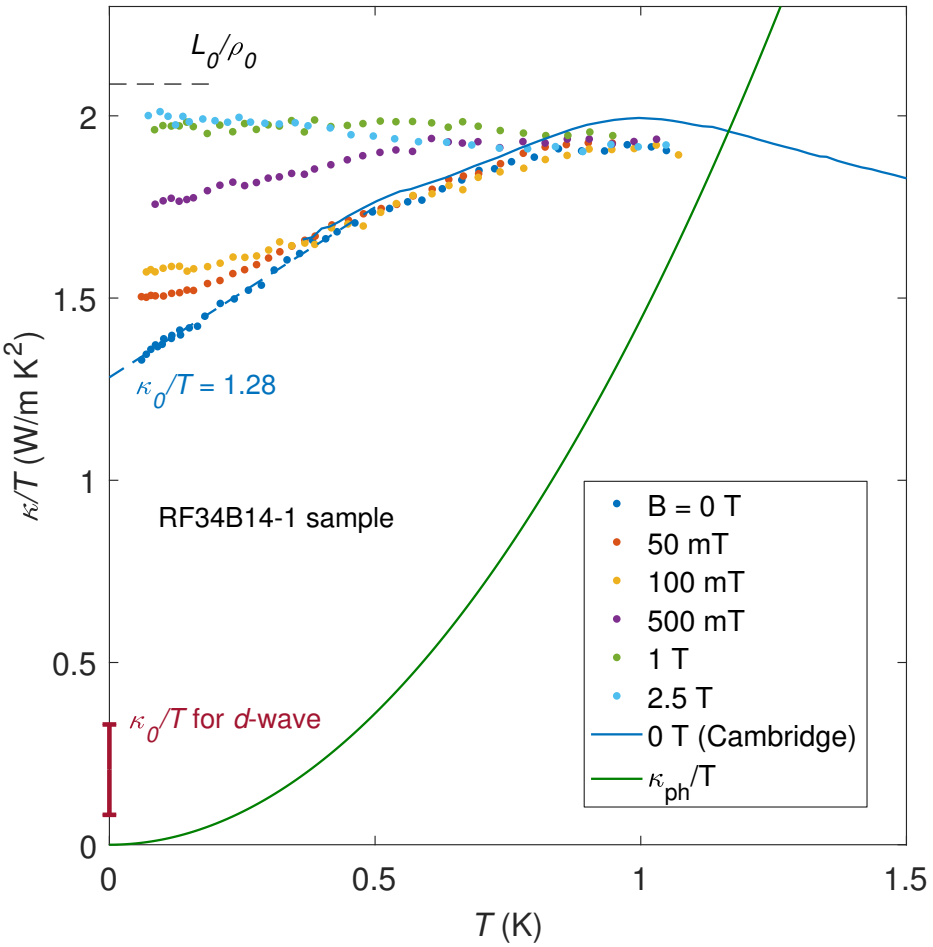

Fig. 5.9 Value of κ/T as a function of temperature for the YFe_2Ge_2 sample RF34B14-1 measured in Waterloo at several fields. This is compared with the zero-field measurement of the same sample done in Cambridge. The estimate of the range of κ_0/T for a d-wave superconductor discussed in Section 5.3 is shown as a maroon bar. The black dashed line represents L_0/ρ_0, which is the normal state κ/T value calculated using WFL. The experimental κ_0/T estimated by fitting the zero-field κ/T data for the range $T < 0.5$ K is 1.28 W/m K^2. The maximum calculated phonon contribution is also shown.

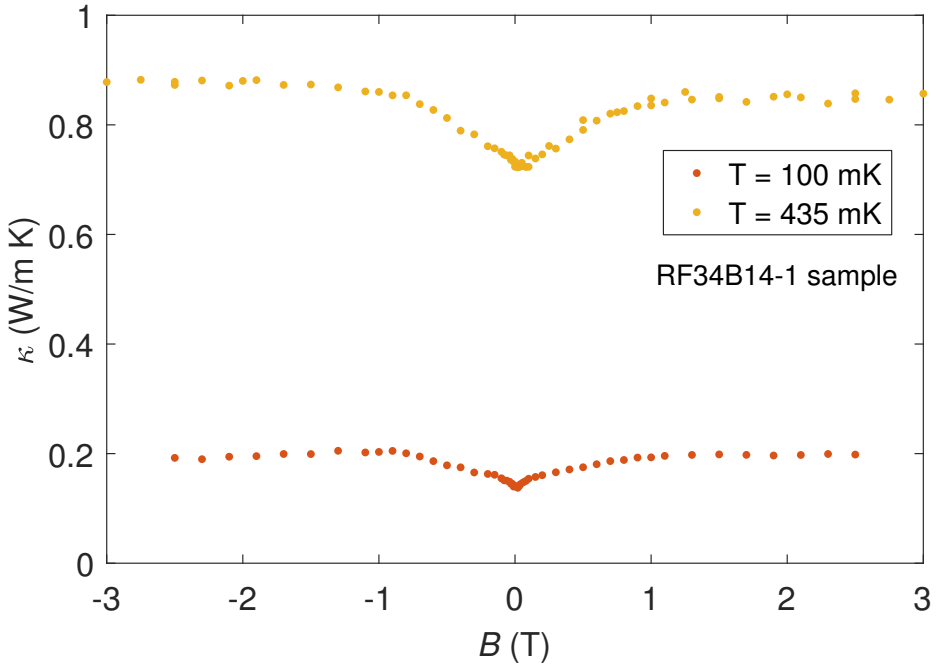

Fig. 5.10 Thermal conductivity as a function of field at two temperatures of YFe_2Ge_2 sample RF34B14-1 measured in Waterloo.

5.3 Discussion

We will now summarise the main experimental results before moving on to further discussion.

1. The heat capacity has a broad superconducting anomaly and the peak of the anomaly is at about 1 K, compared to the resistive transition temperature of about 1.8 K.
2. In zero field, the residual heat conduction, κ_0/T, is about 1.28 W/m K^2, which is a significant fraction of the normal state value of about 2 W/m K^2.
3. In field, the thermal conductivity has a $\sqrt{H}$ dependence that is consistent with the Volovik effect in nodal superconductors.

The most important question that we wish to answer with these experiments is whether YFe_2Ge_2 is a nodal superconductor. From the finite residual heat conduction, it is tempting to conclude that it is. However, we need to consider the more trivial possibility that YFe_2Ge_2 is a fully gapped superconductor but the finite κ_0/T is due to non-superconducting, metallic

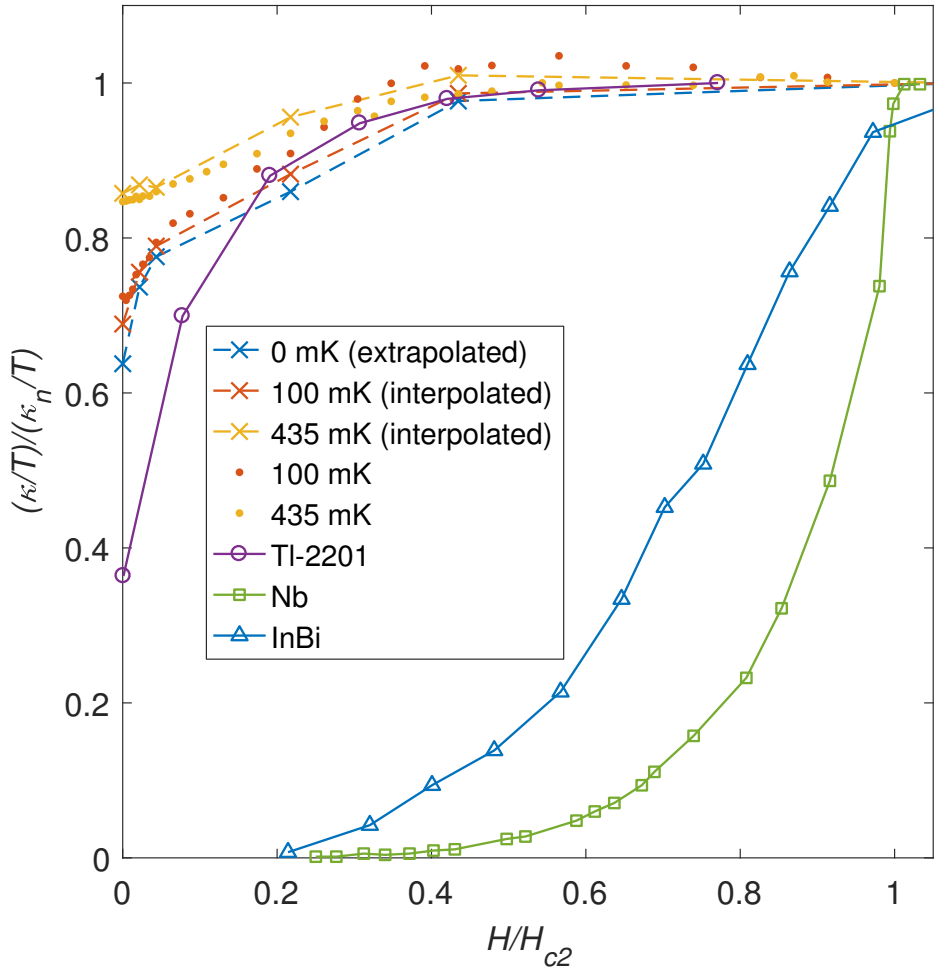

Fig. 5.11 Thermal conductivity normalised by the normal state value at H_{c2} of 2.3 T, as a function of field at different temperatures for YFe_2Ge_2 sample RF34B14-1 measured in Waterloo. The dots are data from field scans, where measurements at the same absolute field value are averaged. The crosses and dashed lines are interpolated and extrapolated data from temperature scans at fixed fields. The data from the d-wave superconductor $Tl_2Ba_2CuO_{6+\delta}$ [83], the clean-limit s-wave superconductor Nb [88] and the dirty-limit s-wave superconductor InBi [185] are shown for comparison.

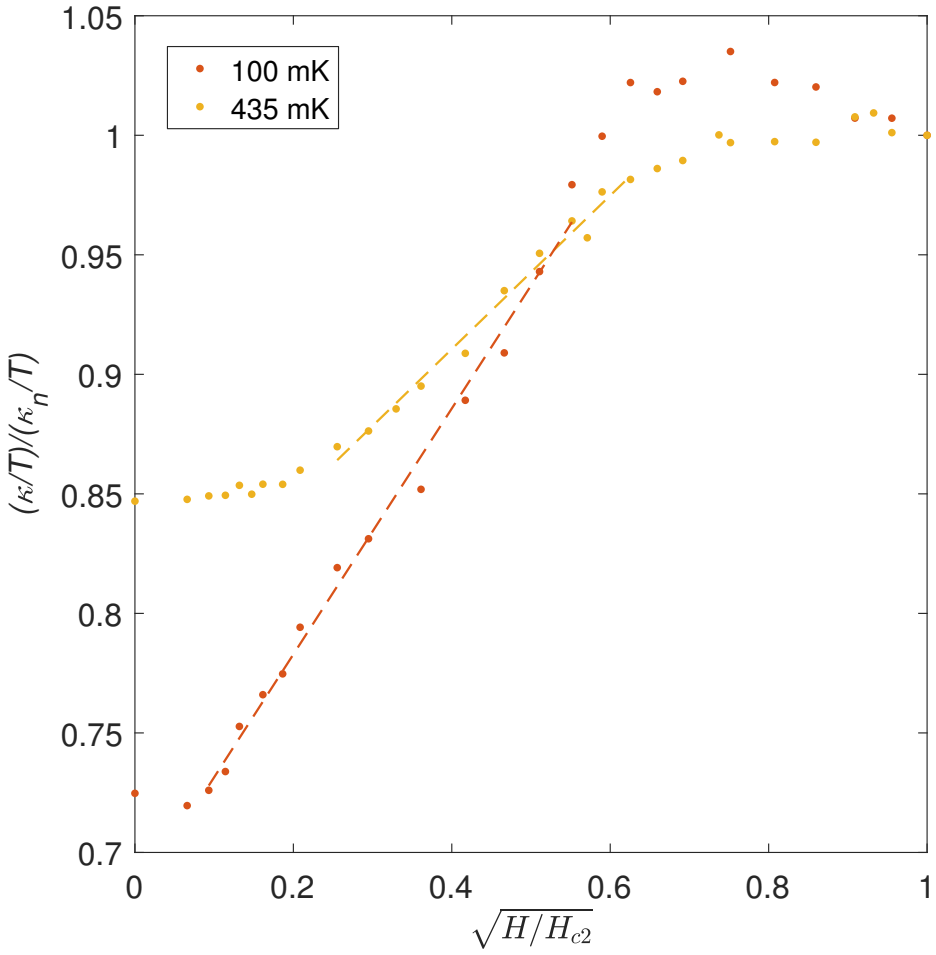

Fig. 5.12 Thermal conductivity of YFe_2Ge_2 sample RF34B14-1 at 100 mK and 435 mK as a function of the square root of field. The dashed lines are guides to the eye to show regions of $\sqrt{H}$ dependence. In this sample, κ/T has a clear $\sqrt{H}$ field dependence. This is consistent with the Volovik effect, which occurs when the energy of the quasiparticles near the nodal region is Doppler shifted by the local superfluid velocity. This suggests that YFe_2Ge_2 has a nodal superconducting gap structure.

impurity phases. These impurity phases could comprise off-stoichiometry YFe_2Ge_2 that is non-superconducting or simply domains of starting material such as Fe. To investigate this possibility, we assume that the YFe_2Ge_2 samples have a distribution of T_c, possibly due to slight variations of stoichiometry across the sample. We also assume that a perfectly pure sample will have the standard BCS heat capacity anomaly of a fully gapped *s*-wave superconductor as tabulated in [186], shown in the inset in Figure 5.13. Using these two assumptions, we performed a constrained linear least-squares fit to find the underlying T_c distribution from the experimental heat capacity data. We divide T_c from 0 to 2 K into 200 bins, and the objective of this fit is to find the fractional amount of the sample in each T_c bin. We assume that every bin has a BCS heat capacity temperature dependence and the total heat capacity is simply the weighted sum of the contribution from all the bins. The results are shown in Figure 5.13 and Figure 5.14. The additional constraints on the fit are the maximum gradient (~ 8 K^{-2}) and curvature (~ 60 K^{-3}) of the distribution, motivated by the physical reasoning that gradients in stoichiometry should create a smoothly varying T_c distribution. The results are not very sensitive to the value of these constraints. The upper bound of the non-superconducting fraction for each sample is estimated by assuming that the portion of the distribution lower than the lowest measured temperature in the heat capacity measurement is non-superconducting. This is represented by the shaded areas to the left of the vertical dashed lines in Figure 5.14.

With these assumptions, less than 20% of the sample is non-superconducting. This should give a residual heat conduction $\kappa_0/T \sim 0.4$ W/m K^2, which is a factor of 3 less than the extrapolated value of 1.28 W/m K^2. Moreover, if the residual heat conduction is purely due to non-superconducting, metallic impurities and the pure YFe_2Ge_2 is a fully gapped superconductor, we would expect an exponential field dependence like Nb, contradictory to what we have seen in Figure 5.11 and 5.12. Hence, we can rule out this trivial case.

Having concluded that YFe_2Ge_2 is a nodal superconductor, we will further discuss whether this is a symmetry-imposed node (e.g. *d*-wave) or an accidental one. In the former case, the value of κ_0/T should be given by a universal value independent of impurity scattering [81] as we have discussed in Section 2.5.1. In the latter case, YFe_2Ge_2 could have an *s*-wave pairing symmetry with accidental nodes. The gap may have the same sign (simple *s*-wave) or different signs ($s_\pm$) between different Fermi sheets. The size of the gap on different sheets could be very different, like in KFe_2As_2 [27, 28]. The magnitude of the residual heat conduction will not be universal and will depend on the impurity concentration [187].

We could estimate the magnitude of the universal heat conduction, κ_0/T, for a *d*-wave

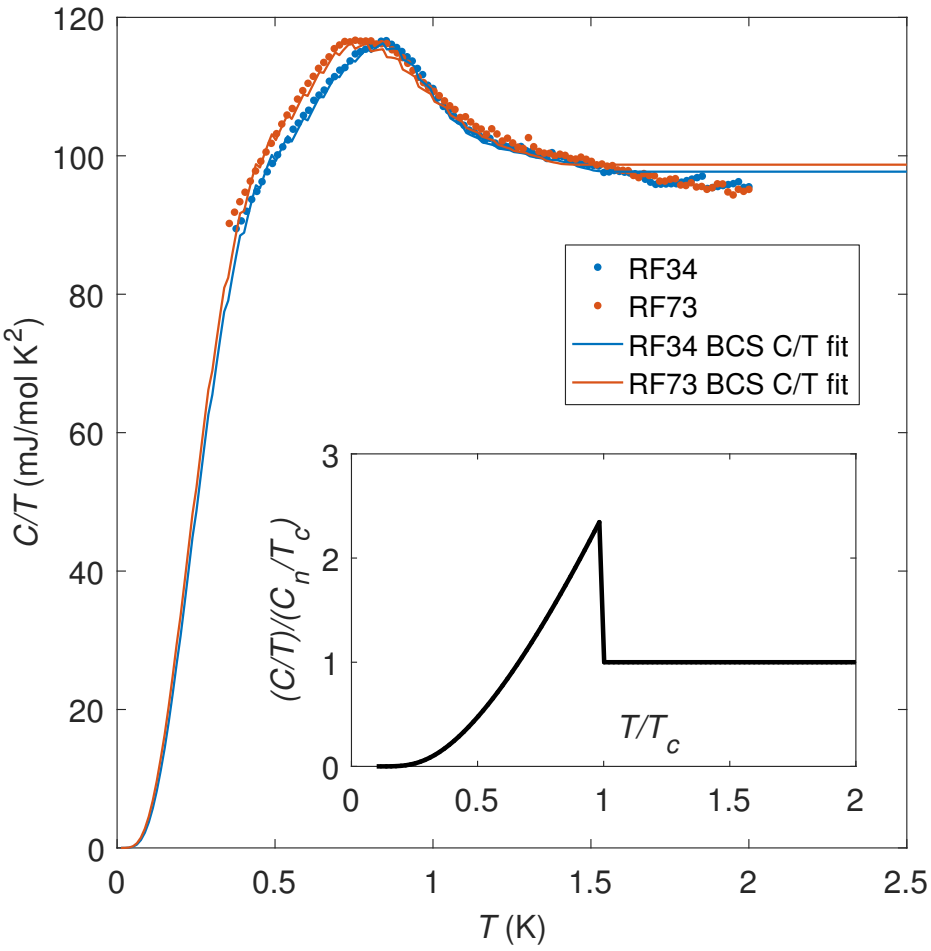

Fig. 5.13 Fit to the heat capacity data of two YFe_2Ge_2 samples, assuming the BCS functional form (shown in inset), to find the underlying T_c distribution.

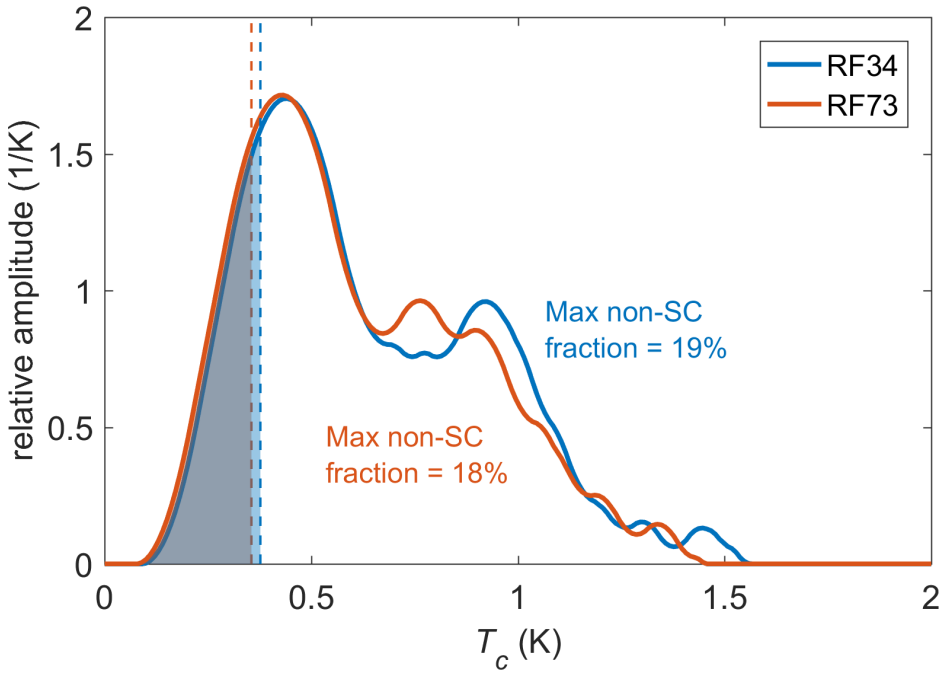

Fig. 5.14 The distribution of T_c of two YFe_2Ge_2 samples that will give the experimental heat capacity temperature dependence. The vertical dashed line shows the lowest temperature data point in the heat capacity measurement. The shaded part of the distribution to the left of the dashed line is assumed to be non-superconducting to obtain an upper bound on the non-superconducting fraction.

pairing symmetry from Equation 2.33. The combination of a $d_{x^2-y^2}$ pairing state and a cylindrical Fermi surface, which is predicted to exist in YFe_2Ge_2 about the Z point [29, 171, 172] (see Figure 5.2(d)), will give rise to four line nodes [81]. If we assume the d-wave superconducting gap function to be $\Delta(\phi) = \Delta_0 \cos 2\phi$, $\mu = 2$ and Δ_0 can be estimated from T_c in the weak coupling regime using $\Delta_0 = 2.14\ k_B T_c$ [81]. The density of states will be estimated from the heat capacity using [62]

$$\frac{C_e}{T} = \frac{1}{3}\pi^2 k_B^2\, N_f. \tag{5.1}$$

The Fermi velocity can be estimated from the coherence length, ξ_0, and the transition temperature, using [182]

$$\begin{aligned} \xi_0 &= \frac{\hbar v_f}{\Delta_{BCS}\,\pi} \\ &= \frac{\hbar v_f}{1.76\,T_c\,\pi}. \end{aligned} \tag{5.2}$$

A summary of the values used to estimate κ_0/T is listed in Table 5.2. To find the density of states per unit volume, we divide by the volume of the formula unit, which is 8.216×10^{-29} m^3 [29]. The estimated value of κ_0/T ranges from 0.082 to 0.33 W/m K^2 and this is represented by the maroon bar in Figure 5.9. The upper limit of this estimation is about a factor of 4 less than the experimental observation. Although this calculation is done for a d-wave pairing symmetry with four line nodes, other more complicated pairing states with combinations of line nodes and point nodes will have very similar values as shown in Table I of [81].

Even though the κ_0/T estimate for a d-wave is a factor of 4 or more too small, it is hard to rule out symmetry-imposed nodes based on this alone. There are several assumptions that we have made which could easily account for that factor of 4. For example, we have assumed a very simple superconducting gap function of $\Delta(\phi) = \Delta_0 \cos 2\phi$, but the real gap function could have a gentler slope near the nodes [75].

Nevertheless, the κ/T data supports the notion of accidental nodes more since they could give rise to large residual thermal conductivity. A crude extrapolation from 0.3 K to zero temperature of κ/T in Figure 5.8 shows that the purer RF73B-S7 have higher residual heat

Quantity (units)	Value (measurement)
T_c (K)	1.8 (resistivity)
	1.0 (heat capacity)
ξ_0 (Å)	120 (critical field from resistivity)
	180 (critical field from heat capacity)
C_e/T (mJ/mol K^2)	95
N_f (states/eV F.U.)	40.2
v_f (m/s)	8.69×10^3–2.35×10^4
Δ_0 (meV)	0.18–0.33

Table 5.2 Values of quantities used in the estimation of universal heat conduction of YFe_2Ge_2 obtained from [29].

conduction than RF34B14-1. This also supports the picture of accidental nodes since the residual heat conduction varies inversely with impurity scattering [187]. When we consider the temperature dependence of κ/T, we find that it is approximately T-linear up to about 0.5 K. This behaviour is very similar to the accidentally nodal superconductor, LaFePO [87], and is distinctly different from the T^2 leading-order correction to κ/T for symmetry-imposed nodes [81], which was observed in the d-wave superconductor $YBa_2Cu_3O_{6.9}$ [75] (cf. Section 2.5.1).

There are also several other pieces of experimental evidence that suggest the superconductivity in YFe_2Ge_2 is similar to that of KFe_2As_2 [27, 28], which is likely to be multiband s-wave with accidental nodes. In Figure 5.8, one can observe a peak-like feature in RF73B-S7 and a small hint of a shoulder in RF34B14-1 as mentioned previously. These features could be readily explained in a multiband picture where the gaps on different bands differ in size and the interband coupling is weak. As the sample is cooled below its T_c, different gaps 'turn on' at different rates which could produce features like those seen in Figure 5.8.

All in all, we have strong indications that YFe_2Ge_2 is a nodal superconductor and have circumstantial evidence for multiband s-wave superconductivity with accidental nodes. In order to prove this conclusively, we need more thermal conductivity measurements of a series of samples with different impurity concentrations. Nonetheless, the existence of nodes

in the gap structure of YFe_2Ge_2 implies a strongly anisotropic gap which then suggests that YFe_2Ge_2 exhibits unconventional superconductivity, and is worthy of further study.

Chapter 6

Summary

Materials in proximity to quantum critical points (QCPs) experience strong fluctuations in the order parameter associated with the transition and often, as a result, display interesting properties. In this dissertation, we have used a variety of experimental probes such as Shubnikov-de Haas quantum oscillations, thermal conductivity and heat capacity, to better understand two such materials — $A_3T_4Sn_{13}$ and YFe_2Ge_2.

$A_3T_4Sn_{13}$ (A = Ca, Sr; T = Ir, Rh) is a family of quasi-skutterudite superconductors with moderate T_c's between 4 and 8 K. Although the superconductivity is believed to be phonon-mediated with s-wave pairing symmetry, an unusual second-order structural transition makes this material family fascinating to study. Whether this structural transition is a result of three distortions with perpendicular wavevectors resulting in a cubic-to-cubic transformation, or each wavevector acting independently giving rise to cubic-to-tetragonal transformations and formation of twinned domains is a disputed issue. We have measured quantum oscillations in the resistivity of $Sr_3Ir_4Sn_{13}$ and compared it to density functional theory (DFT) calculations for both scenarios. Our results strongly suggest that the former interpretation is correct.

The structural transition temperature T^* in $A_3T_4Sn_{13}$ can be suppressed to zero by tuning with physical or chemical pressure. In $(Ca_xSr_{1-x})_3Rh_4Sn_{13}$, the quantum critical point can be accessed purely by chemical substitution at $x \sim 0.9$. In the vicinity of the QCP, we expect large fluctuations of the order parameter at low temperatures, which for a structural transition could manifest as a structural disorder. We have measured thermal conductivity at temperatures much lower than T_c and found that it is well described by a single power

law with suppressed exponents near the QCP. The heat capacity, however, remains $\sim T^3$. After excluding conventional phonon scattering mechanisms, we propose the possibility of intrinsic quasi-static spatial disorder that is related to the structural QCP.

There are several possibilities for future work related to structural quantum criticality. The low-temperature thermal conductivity of perovskite materials close to structural transitions, like ScF_3 and $SrTiO_3$, could be investigated and compared to $(Ca_xSr_{1-x})_3Rh_4Sn_{13}$. In addition, x-ray diffraction experiments on single crystals of $(Ca_xSr_{1-x})_3Rh_4Sn_{13}$ across the phase diagram should also be interesting. If the intrinsic spatial disorder picture is accurate, this should show up as an increase in the thermal ellipsoids of Sn atoms as the system is tuned towards the structural QCP (similar to [105]). Finally, resonant ultrasound spectroscopy might be another valuable probe to investigate structural criticality. Spatial disorder in a sample might manifest as significant broadening of peaks in the measured spectrum.

YFe_2Ge_2 is closely linked to the "122" family of iron-based superconductors like KFe_2As_2, although it has a significantly lower $T_c \sim 1$ K. It has a rather three-dimensional Fermi surface which closely resembles that of KFe_2As_2 in the pressure-induced collapsed tetragonal phase. YFe_2Ge_2 is in proximity to several types of magnetic order which are predicted by DFT calculations to have lower energy than the non-spin polarised case. Even though YFe_2Ge_2 is non-magnetic, its superconductivity could be strongly affected by magnetic fluctuations. Through a collaboration with researchers at the University of Waterloo, we have measured the thermal conductivity of YFe_2Ge_2 down to millikelvin temperatures and up to 2.5 T in field. Our results suggest that YFe_2Ge_2 is a nodal superconductor. This result could assist in the explanation of the unconventional superconductivity in iron-based superconductors.

While our data suggest that YFe_2Ge_2 has a nodal gap structure, it is unclear whether this is due to pairing symmetry or is accidental. This problem can be addressed in a future project. If the sample growth technique is refined such that bulk-superconducting, single-crystal YFe_2Ge_2 samples are readily available, a direct and convincing measurement will be thermal conductivity in field with high angular resolution (much like [153]). Since thermal conductivity is very rapidly enhanced, even in small fields of about 50 mT, this measurement should be possible with two perpendicular sets of small superconducting Helmholtz coils placed next to the sample. As the field is rotated in the basal plane of the sample, one should observe either four or eight peaks in thermal conductivity per complete rotation. This will signify the presence of four or eight line nodes, which correspond to the scenarios of symmetry-imposed or accidental nodes respectively.

Appendix A

Thermal conductivity results of SmB_6

SmB_6 is a Kondo insulator with a small gap at the Fermi level due to hybridisation of the 4f and 5d bands [188] which shows up at low temperatures from 20 K down to 4 K as a divergence in resistivity and Hall coefficient [189, 190]. Unlike a semiconductor, however, the resistivity and Hall coefficient plateau at temperatures below 4 K [191]. The resolution of this puzzle began with the theoretical prediction that Kondo insulators like SmB_6 can have an insulating bulk with a topologically protected conductive surface [192, 193]. This was quickly backed up by experimental evidence from surface conductance and Hall measurements [194, 195]. Recently, the report of the observations of bulk quantum oscillations [196] in SmB_6, contradictory to previous quantum oscillation measurement which only saw surface contributions [197] and the conventional expectation that insulators do not have quantum oscillations, generated rigorous response from the research community [198, 199].

The thermal conductivity of SmB_6, which is part of ongoing work [200], is equally enigmatic. In zero field, SmB_6 behaves like an ordinary insulator. However, it has significantly enhanced thermal conductivity in magnetic fields up to 12 T [200]. Here, we show zero-field thermal conductivity data measured in Cambridge on a floating-zone–grown sample from 50 K down to 0.4 K, which was part of the sample-screening process (Figure A.1). The geometric factor of the sample is 73 ± 6 μm. We compare our measurement with that by Toews and Hill from the University of Waterloo on another floating-zone–grown single-crystalline sample (labelled FZ1 in [200]). We also plot on the same figure the thermal conductivity data by Sera et al., which was also done on a single crystal floating-zone–grown sample [96]. All three samples exhibit thermal conductivity peaks at around 14 K, which is likely due to the cross-over between impurity scattering of phonons at high temperatures ($\kappa \sim T^{-1.5}$) and

boundary scattering at lower temperatures ($\kappa \sim T^3$) [135]. The height of the peak is a good indication of sample quality. We find that the quality of our SmB_6 sample is comparable to that of Sera et al. while the sample measured in Waterloo is of higher quality. We expect that the difference in thermal conductivity due to sample quality to vanish in the boundary scattering limit. This is indeed observed as our data agrees closely with the measurement by Toews and Hill below 1 K (see inset in Figure A.1).

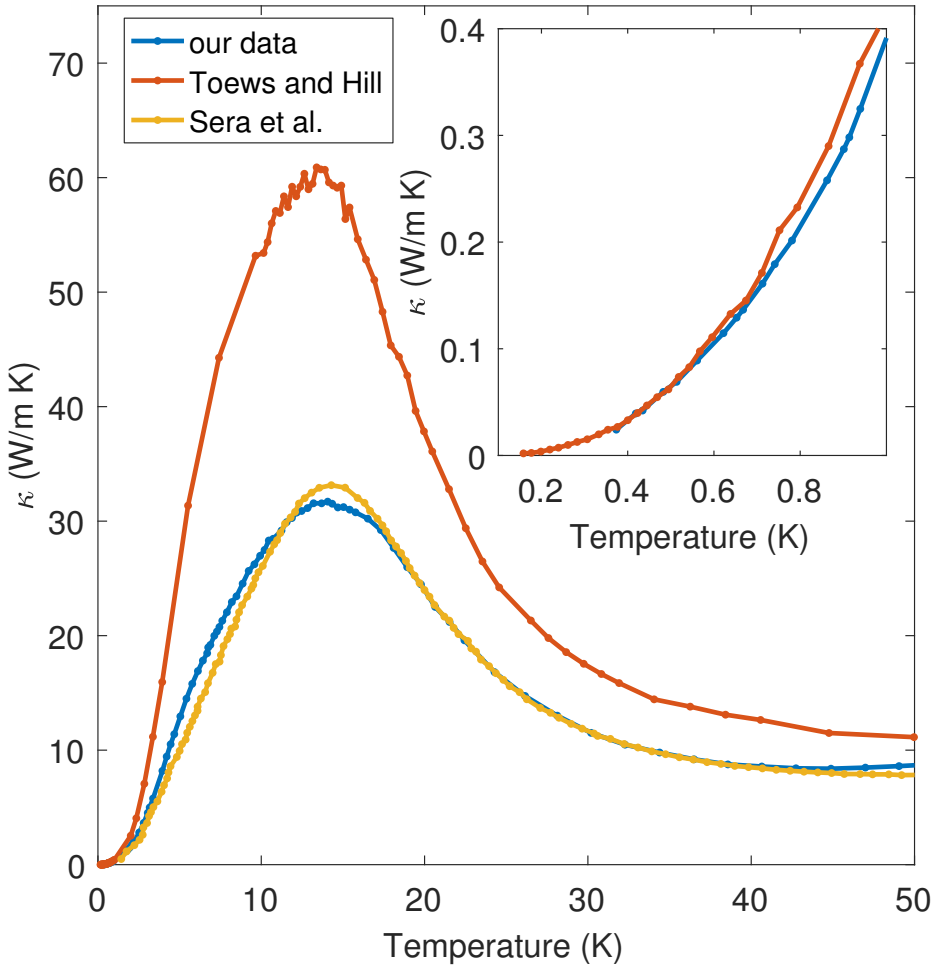

Fig. A.1 Thermal conductivity of a floating-zone–grown SmB_6 sample measured at zero magnetic field, compared to similar measurements by Toews and Hill (FZ1 in [200]) and Sera et al. [96]. The inset shows the data below 1 K.

References

[1] P. Gegenwart, J. Custers, C. Geibel, K. Neumaier, T. Tayama, K. Tenya, O. Trovarelli, and F. Steglich. Magnetic-Field Induced Quantum Critical Point in $YbRh_2Si_2$. *Physical Review Letters*, 89(5):056402, July 2002.

[2] N. D. Mathur, F. M. Grosche, S. R. Julian, I. R. Walker, D. M. Freye, R. K. W. Haselwimmer, and G. G. Lonzarich. Magnetically mediated superconductivity in heavy fermion compounds. *Nature*, 394(6688):39–43, July 1998.

[3] S. Kasahara, T. Shibauchi, K. Hashimoto, K. Ikada, S. Tonegawa, R. Okazaki, H. Shishido, H. Ikeda, H. Takeya, K. Hirata, T. Terashima, and Y. Matsuda. Evolution from non-Fermi- to Fermi-liquid transport via isovalent doping in $BaFe_2(As_{1-x}P_x)_2$ superconductors. *Physical Review B*, 81(18):184519, May 2010.

[4] F. Steglich, J. Aarts, C. D. Bredl, W. Lieke, D. Meschede, W. Franz, and H. Schäfer. Superconductivity in the Presence of Strong Pauli Paramagnetism: $CeCu_2Si_2$. *Physical Review Letters*, 43(25):1892–1896, December 1979.

[5] C. Petrovic, P. G. Pagliuso, M. F. Hundley, R. Movshovich, J. L. Sarrao, J. D. Thompson, Z. Fisk, and P. Monthoux. Heavy-fermion superconductivity in $CeCoIn_5$ at 2.3 K. *Journal of Physics: Condensed Matter*, 13(17):L337, 2001.

[6] J. G. Bednorz and K. A. Müller. Possible highT c superconductivity in the Ba-La-Cu-O system. *Zeitschrift für Physik B Condensed Matter*, 64(2):189–193, June 1986.

[7] M. K. Wu, J. R. Ashburn, C. J. Torng, P. H. Hor, R. L. Meng, L. Gao, Z. J. Huang, Y. Q. Wang, and C. W. Chu. Superconductivity at 93 K in a new mixed-phase Y-Ba-Cu-O compound system at ambient pressure. *Physical Review Letters*, 58(9):908–910, March 1987.

[8] B. Keimer, S. A. Kivelson, M. R. Norman, S. Uchida, and J. Zaanen. From quantum matter to high-temperature superconductivity in copper oxides. *Nature*, 518(7538):179–186, February 2015.

[9] Yoichi Kamihara, Takumi Watanabe, Masahiro Hirano, and Hideo Hosono. Iron-Based Layered Superconductor $La[O_{1-x}F_x]FeAs$ (x = 0.05 to 0.12) with T_c = 26 K. *Journal of the American Chemical Society*, 130(11):3296–3297, March 2008.

[10] Johnpierre Paglione and Richard L. Greene. High-temperature superconductivity in iron-based materials. *Nature Physics*, 6(9):645–658, September 2010.

[11] F. L. Ning, K. Ahilan, T. Imai, A. S. Sefat, M. A. McGuire, B. C. Sales, D. Mandrus, P. Cheng, B. Shen, and H.-H Wen. Contrasting Spin Dynamics between Underdoped and Overdoped $Ba(Fe_{1-x}Co_x)_2As_2$. *Physical Review Letters*, 104(3):037001, January 2010.

[12] S. E. Rowley, L. J. Spalek, R. P. Smith, M. P. M. Dean, M. Itoh, J. F. Scott, G. G. Lonzarich, and S. S. Saxena. Ferroelectric quantum criticality. *Nature Physics*, 10(5):367–372, May 2014.

[13] Benjamin K. Greve, Kenneth L. Martin, Peter L. Lee, Peter J. Chupas, Karena W. Chapman, and Angus P. Wilkinson. Pronounced Negative Thermal Expansion from a Simple Structure: Cubic ScF_3. *Journal of the American Chemical Society*, 132(44):15496–15498, November 2010.

[14] Sahan U. Handunkanda, Erin B. Curry, Vladimir Voronov, Ayman H. Said, Gian G. Guzmán-Verri, Richard T. Brierley, Peter B. Littlewood, and Jason N. Hancock. Large isotropic negative thermal expansion above a structural quantum phase transition. *Physical Review B*, 92(13):134101, October 2015.

[15] Chen W. Li, Xiaoli Tang, J. A. Muñoz, J. B. Keith, S. J. Tracy, D. L. Abernathy, and B. Fultz. Structural Relationship between Negative Thermal Expansion and Quartic Anharmonicity of Cubic ScF_3. *Physical Review Letters*, 107(19):195504, November 2011.

[16] Lina E. Klintberg, Swee K. Goh, Patricia L. Alireza, Paul J. Saines, David A. Tompsett, Peter W. Logg, Jinhu Yang, Bin Chen, Kazuyoshi Yoshimura, and F. Malte Grosche. Pressure- and Composition-Induced Structural Quantum Phase Transition in the Cubic Superconductor $(Sr,Ca)_3Ir_4Sn_{13}$. *Physical Review Letters*, 109(23):237008, December 2012.

[17] Martin T. Dove. *Structure and Dynamics: An Atomic View of Materials*. Oxford Master Series in Physics. Oxford University Press, March 2003.

[18] S.K. Goh, D.A. Tompsett, P.J. Saines, H.C. Chang, T. Matsumoto, M. Imai, K. Yoshimura, and F.M. Grosche. Ambient Pressure Structural Quantum Critical Point in the Phase Diagram of $(Ca_xSr_{1-x})_3Rh_4Sn_{13}$. *Physical Review Letters*, 114(9):097002, March 2015.

[19] S. Y. Zhou, H. Zhang, X. C. Hong, B. Y. Pan, X. Qiu, W. N. Dong, X. L. Li, and S. Y. Li. Nodeless superconductivity in $Ca_3Ir_4Sn_{13}$: Evidence from quasiparticle heat transport. *Physical Review B*, 86(6):064504, August 2012.

[20] Wing Chi Yu, Yiu Wing Cheung, Paul J. Saines, Masaki Imai, Takuya Matsumoto, Chishiro Michioka, Kazuyoshi Yoshimura, and Swee K. Goh. Strong Coupling Superconductivity in the Vicinity of the Structural Quantum Critical Point in $(Ca_xSr_{1-x})_3Rh_4Sn_{13}$. *Physical Review Letters*, 115(20):207003, November 2015.

[21] Iain W. H. Oswald, Binod K. Rai, Gregory T. McCandless, Emilia Morosan, and Julia Y. Chan. The proof is in the powder: revealing structural peculiarities in the $Yb_3Rh_4Sn_{13}$ structure type. *CrystEngComm*, 19(25):3381–3391, 2017.

[22] D. G. Mazzone, S. Gerber, J. L. Gavilano, R. Sibille, M. Medarde, B. Delley, M. Ramakrishnan, M. Neugebauer, L. P. Regnault, D. Chernyshov, A. Piovano, T. M. Fernández-Díaz, L. Keller, A. Cervellino, E. Pomjakushina, K. Conder, and M. Kenzelmann. Crystal structure and phonon softening in $Ca_3Ir_4Sn_{13}$. *Physical Review B*, 92(2):024101, July 2015.

[23] I. I. Mazin, D. J. Singh, M. D. Johannes, and M. H. Du. Unconventional Superconductivity with a Sign Reversal in the Order Parameter of $LaFeAsO_{1-x}F_x$. *Physical Review Letters*, 101(5):057003, July 2008.

[24] X. G. Luo, M. A. Tanatar, J.-Ph. Reid, H. Shakeripour, N. Doiron-Leyraud, N. Ni, S. L. Bud'ko, P. C. Canfield, Huiqian Luo, Zhaosheng Wang, Hai-Hu Wen, R. Prozorov, and Louis Taillefer. Quasiparticle heat transport in single-crystalline $Ba_{1-x}K_xFe_2As_2$: Evidence for a k-dependent superconducting gap without nodes. *Physical Review B*, 80(14):140503, October 2009.

[25] J.-Ph. Reid, M. A. Tanatar, A. Juneau-Fecteau, R. T. Gordon, S. René de Cotret, N. Doiron-Leyraud, T. Saito, H. Fukazawa, Y. Kohori, K. Kihou, C. H. Lee, A. Iyo, H. Eisaki, R. Prozorov, and Louis Taillefer. Universal Heat Conduction in the Iron Arsenide Superconductor KFe_2As_2: Evidence of a d-Wave State. *Physical Review Letters*, 109(8):087001, August 2012.

[26] D. Watanabe, T. Yamashita, Y. Kawamoto, S. Kurata, Y. Mizukami, T. Ohta, S. Kasahara, M. Yamashita, T. Saito, H. Fukazawa, Y. Kohori, S. Ishida, K. Kihou, C. H. Lee, A. Iyo, H. Eisaki, A. B. Vorontsov, T. Shibauchi, and Y. Matsuda. Doping evolution of the quasiparticle excitations in heavily hole-doped $Ba_{1-x}K_xFe_2As_2$: A possible superconducting gap with sign-reversal between hole pockets. *Physical Review B*, 89(11):115112, March 2014.

[27] K. Okazaki, Y. Ota, Y. Kotani, W. Malaeb, Y. Ishida, T. Shimojima, T. Kiss, S. Watanabe, C.-T. Chen, K. Kihou, C. H. Lee, A. Iyo, H. Eisaki, T. Saito, H. Fukazawa, Y. Kohori, K. Hashimoto, T. Shibauchi, Y. Matsuda, H. Ikeda, H. Miyahara, R. Arita, A. Chainani, and S. Shin. Octet-Line Node Structure of Superconducting Order Parameter in KFe_2As_2. *Science*, 337(6100):1314–1317, September 2012.

[28] Frédéric Hardy, Robert Eder, Martin Jackson, Dai Aoki, Carley Paulsen, Thomas Wolf, Philipp Burger, Anna Böhmer, Peter Schweiss, Peter Adelmann, Robert A. Fisher, and Christoph Meingast. Multiband Superconductivity in KFe_2As_2: Evidence for One Isotropic and Several Lilliputian Energy Gaps. *Journal of the Physical Society of Japan*, 83(1):014711, December 2013.

[29] Jiasheng Chen, Konstantin Semeniuk, Zhuo Feng, Pascal Reiss, Philip Brown, Yang Zou, Peter W. Logg, Giulio I. Lampronti, and F. Malte Grosche. Unconventional Superconductivity in the Layered Iron Germanide YFe_2Ge_2. *Physical Review Letters*, 116(12):127001, March 2016.

[30] Gilbert G. Lonzarich. The Magnetic Electron. In *Electron: A Centenary Volume*, pages 109–147. Cambridge University Press, March 1997.

[31] Hilbert v. Löhneysen, Achim Rosch, Matthias Vojta, and Peter Wölfle. Fermi-liquid instabilities at magnetic quantum phase transitions. *Reviews of Modern Physics*, 79(3):1015–1075, August 2007.

[32] John A. Hertz. Quantum critical phenomena. *Physical Review B*, 14(3):1165–1184, August 1976.

[33] A. J. Millis. Effect of a nonzero temperature on quantum critical points in itinerant fermion systems. *Physical Review B*, 48(10):7183–7196, September 1993.

[34] A. von Hippel. US National Defense Research Committee Report 300. *NDRC, Boston, MA*, 1944.

[35] Gerald Burns and B. A. Scott. Raman Studies of Underdamped Soft Modes in $PbTiO_3$. *Physical Review Letters*, 25(3):167–170, July 1970.

[36] Hiromi Unoki and Tunetaro Sakudo. Electron Spin Resonance of Fe^{3+} in $SrTiO_3$ with Special Reference to the 110°K Phase Transition. *Journal of the Physical Society of Japan*, 23(3):546–552, September 1967.

[37] T. Riste, E. J. Samuelsen, K. Otnes, and J. Feder. Critical behaviour of $SrTiO_3$ near the 105°K phase transition. *Solid State Communications*, 9(17):1455–1458, September 1971.

[38] E. Salje. Phase transitions in ferroelastic and co-elastic crystals. *Ferroelectrics*, 104(1):111–120, April 1990.

[39] E. Salje and G. Hoppmann. Direct observation of ferroelasticity in $Pb_3(PO_4)_2$ - $Pb_3(VO_4)_2$. *Materials Research Bulletin*, 11(12):1545–1549, December 1976.

[40] S. A. T. Redfern and E. Salje. Spontaneous strain and the ferroelastic phase transition in As_2O_5. *Journal of Physics C: Solid State Physics*, 21(2):277, 1988.

[41] M. E. Lines and A. M. Glass. *Principles and Applications of Ferroelectrics and Related Materials*. OUP Oxford, 1977.

[42] P. A. Fleury, J. F. Scott, and J. M. Worlock. Soft Phonon Modes and the 110 K Phase Transition in $SrTiO_3$. *Physical Review Letters*, 21(1):16–19, July 1968.

[43] G. Shirane and Y. Yamada. Lattice-Dynamical Study of the 110 K Phase Transition in $SrTiO_3$. *Physical Review*, 177(2):858–863, January 1969.

[44] P. W. Anderson. Proceedings of the All-Union Conference on the Physics of Dielectrics. In *Academy of Science USSR*, volume 290, 1958.

[45] W. Cochran. Crystal stability and the theory of ferroelectricity. *Advances in Physics*, 9(36):387–423, October 1960.

[46] Max Born and Kun Huang. *Dynamical Theory of Crystal Lattices*. Clarendon Press, 1998.

[47] R. A. Cowley, W. J. L. Buyers, and G. Dolling. Relationship of normal modes of vibration of strontium titanate and its antiferroelectric phase transition at 110°K. *Solid State Communications*, 7(1):181–184, January 1969.

[48] P. Hohenberg and W. Kohn. Inhomogeneous Electron Gas. *Physical Review*, 136(3B):B864–B871, November 1964.

[49] W. Kohn and L. J. Sham. Self-Consistent Equations Including Exchange and Correlation Effects. *Physical Review*, 140(4A):A1133–A1138, November 1965.

[50] W. Kohn. Nobel Lecture: Electronic structure of matter—wave functions and density functionals. *Reviews of Modern Physics*, 71(5):1253–1266, October 1999.

[51] Reiner M. Dreizler and Eberhard K.U. Gross. *Density Functional Theory*. Springer-Verlag, April 1990.

[52] Richard M. Martin. *Electronic Structure: Basic Theory and Practical Methods*. Cambridge University Press, April 2004.

[53] Carlos Fiolhais, Fernando Nogueira, and Miguel A. L. Marques, editors. *A Primer in Density Functional Theory*. Springer, Berlin ; New York, 2003 edition, August 2003.

[54] M. Born and R. Oppenheimer. Zur Quantentheorie der Molekeln. *Annalen der Physik*, 389(20):457–484, January 1927.

[55] D. J. Chadi and R. M. Martin. Calculation of lattice dynamical properties from electronic energies: Application to C, Si and Ge. *Solid State Communications*, 19(7):643–646, July 1976.

[56] K. Kunc and Richard M. Martin. Ab Initio Force Constants of GaAs: A New Approach to Calculation of Phonons and Dielectric Properties. *Physical Review Letters*, 48(6):406–409, February 1982.

[57] Paolo Giannozzi, Stefano Baroni, Nicola Bonini, Matteo Calandra, Roberto Car, Carlo Cavazzoni, Davide Ceresoli, Guido L. Chiarotti, Matteo Cococcioni, Ismaila Dabo, Andrea Dal Corso, Stefano de Gironcoli, Stefano Fabris, Guido Fratesi, Ralph Gebauer, Uwe Gerstmann, Christos Gougoussis, Anton Kokalj, Michele Lazzeri, Layla Martin-Samos, Nicola Marzari, Francesco Mauri, Riccardo Mazzarello, Stefano Paolini, Alfredo Pasquarello, Lorenzo Paulatto, Carlo Sbraccia, Sandro Scandolo, Gabriele Sclauzero, Ari P. Seitsonen, Alexander Smogunov, Paolo Umari, and Renata M. Wentzcovitch. QUANTUM ESPRESSO: a modular and open-source software project for quantum simulations of materials. *Journal of Physics: Condensed Matter*, 21(39):395502, 2009.

[58] Stefano Baroni, Stefano de Gironcoli, Andrea Dal Corso, and Paolo Giannozzi. Phonons and related crystal properties from density-functional perturbation theory. *Reviews of Modern Physics*, 73(2):515–562, July 2001.

[59] David Shoenberg. *Magnetic Oscillations in Metals*. Cambridge University Press, January 1984.

[60] L. Onsager. Interpretation of the de Haas-van Alphen effect. *Philosophical Magazine Series 7*, 43(344):1006–1008, 1952.

[61] John Singleton. *Band Theory and Electronic Properties of Solids*. OUP Oxford, August 2001.

[62] J. M. Ziman. *Electrons and Phonons: The Theory of Transport Phenomena in Solids*. OUP Oxford, 1960.

[63] E. N. Adams and T. D. Holstein. Quantum theory of transverse galvano-magnetic phenomena. *Journal of Physics and Chemistry of Solids*, 10(4):254–276, August 1959.

[64] Christoph Bergemann. *Magnetic effects in unconventional superconductors*. PhD thesis, University of Cambridge, 1999.

[65] R. B. Dingle. Some Magnetic Properties of Metals. II. The Influence of Collisions on the Magnetic Behaviour of Large Systems. *Proceedings of the Royal Society of London. Series A. Mathematical and Physical Sciences*, 211(1107):517–525, March 1952.

[66] Philip B. Allen. The electron-phonon coupling constant λ. In Charles K. Poole, editor, *Handbook of Superconductivity*. Academic Press, October 1999.

[67] J. P. Carbotte. Properties of boson-exchange superconductors. *Reviews of Modern Physics*, 62(4):1027–1157, October 1990.

[68] C. D. Motchenbacher. *Low-noise Electronic System Design*. Wiley-Blackwell, New York, 1 edition edition, August 1993.

[69] H. Nyquist. Thermal Agitation of Electric Charge in Conductors. *Physical Review*, 32(1):110–113, July 1928.

[70] J. B. Johnson. Thermal Agitation of Electricity in Conductors. *Physical Review*, 32(1):97–109, July 1928.

[71] CMR. Medium Frequency Cryogenic Transformer - in SC shield with connectors, 2014. Technical brochure.

[72] Brookdeal. 5004 Ultra Low Noise Preamplifier, 1976. Instruction manual.

[73] SRS. Lock In Amplifier - SR830 and SR810, 2014. Instruction manual.

[74] P. G. Klemens. Thermal Conductivity of Solids at Low Temperatures. *Handbuch der Physik*, 3:198–281, 1956.

[75] Louis Taillefer, Benoit Lussier, Robert Gagnon, Kamran Behnia, and Hervé Aubin. Universal Heat Conduction in $YBa_2Cu_3O_{6.9}$. *Physical Review Letters*, 79(3):483–486, July 1997.

[76] H. Shakeripour, C. Petrovic, and Louis Taillefer. Heat transport as a probe of superconducting gap structure. *New Journal of Physics*, 11(5):055065, 2009.

[77] J.-Ph Reid, A. Juneau-Fecteau, R. T. Gordon, S. René de Cotret, N. Doiron-Leyraud, X. G. Luo, H. Shakeripour, J Chang, M. A. Tanatar, H. Kim, R. Prozorov, T. Saito, H. Fukazawa, Y. Kohori, K. Kihou, C. H. Lee, A. Iyo, H. Eisaki, B Shen, H.-H. Wen, and Louis Taillefer. From d-wave to s-wave pairing in the iron-pnictide superconductor (Ba,K)Fe_2As_2. *Superconductor Science and Technology*, 25(8):084013, 2012.

[78] Etienne Boaknin, M. A. Tanatar, Johnpierre Paglione, D. Hawthorn, F. Ronning, R. W. Hill, M. Sutherland, Louis Taillefer, Jeff Sonier, S. M. Hayden, and J. W. Brill. Heat Conduction in the Vortex State of $NbSe_2$: Evidence for Multiband Superconductivity. *Physical Review Letters*, 90(11):117003, March 2003.

[79] A. Connolly and K. Mendelssohn. Thermal Conductivity of Tantalum and Niobium Below 1°K. *Proceedings of the Royal Society of London A: Mathematical, Physical and Engineering Sciences*, 266(1327):429–439, March 1962.

[80] J. Bardeen, G. Rickayzen, and L. Tewordt. Theory of the Thermal Conductivity of Superconductors. *Physical Review*, 113(4):982–994, February 1959.

[81] M. J. Graf, S-K. Yip, J. A. Sauls, and D. Rainer. Electronic thermal conductivity and the Wiedemann-Franz law for unconventional superconductors. *Physical Review B*, 53(22):15147–15161, June 1996.

[82] Patrick A. Lee. Localized states in a *d*-wave superconductor. *Physical Review Letters*, 71(12):1887–1890, September 1993.

[83] Cyril Proust, Etienne Boaknin, R. W. Hill, Louis Taillefer, and A. P. Mackenzie. Heat Transport in a Strongly Overdoped Cuprate: Fermi Liquid and a Pure *d*-Wave BCS Superconductor. *Physical Review Letters*, 89(14):147003, September 2002.

[84] C. C. Tsuei and J. R. Kirtley. Phase-Sensitive Evidence for *d*-Wave Pairing Symmetry in Electron-Doped Cuprate Superconductors. *Physical Review Letters*, 85(1):182–185, July 2000.

[85] V. Mishra, A. Vorontsov, P. J. Hirschfeld, and I. Vekhter. Theory of thermal conductivity in extended-*s* state superconductors: Application to ferropnictides. *Physical Review B*, 80(22):224525, December 2009.

[86] R. W. Hill, Christian Lupien, M. Sutherland, Etienne Boaknin, D. G. Hawthorn, Cyril Proust, F. Ronning, Louis Taillefer, Ruixing Liang, D. A. Bonn, and W. N. Hardy. Transport in Ultraclean $YBa_2Cu_3O_7$: Neither Unitary nor Born Impurity Scattering. *Physical Review Letters*, 92(2):027001, January 2004.

[87] Mike Sutherland, J. Dunn, W. H. Toews, Eoin O'Farrell, James Analytis, Ian Fisher, and R. W. Hill. Low-energy quasiparticles probed by heat transport in the iron-based superconductor LaFePO. *Physical Review B*, 85(1):014517, January 2012.

[88] J. Lowell and J. B. Sousa. Mixed-state thermal conductivity of type II superconductors. *Journal of Low Temperature Physics*, 3(1):65–87, July 1970.

[89] G. E. Volovik. Superoconductivity with lines of gap nodes: density of states in the vortex. *Pis'ma v Zhurnal Ehksperimental'noj i Teoreticheskoj Fiziki*, 58(5-6):457–461, 1993.

[90] Kun Yang and S. L. Sondhi. Response of a $d_{x^2-y^2}$ superconductor to a Zeeman magnetic field. *Physical Review B*, 57(14):8566–8570, April 1998.

[91] Mike Sutherland, R. P. Smith, N. Marcano, Y. Zou, S. E. Rowley, F. M. Grosche, N. Kimura, S. M. Hayden, S. Takashima, M. Nohara, and H. Takagi. Transport and thermodynamic evidence for a marginal Fermi-liquid state in $ZrZn_2$. *Physical Review B*, 85(3):035118, January 2012.

[92] Mike Sutherland, D. G. Hawthorn, R. W. Hill, F. Ronning, S. Wakimoto, H. Zhang, C. Proust, Etienne Boaknin, C. Lupien, Louis Taillefer, Ruixing Liang, D. A. Bonn, W. N. Hardy, Robert Gagnon, N. E. Hussey, T. Kimura, M. Nohara, and H. Takagi. Thermal conductivity across the phase diagram of cuprates: Low-energy quasiparticles and doping dependence of the superconducting gap. *Physical Review B*, 67(17):174520, May 2003.

[93] Lakeshore. Cryogenic Temperature Sensors Specifications, 2017. Technical brochure.

[94] D. J Benford, T. J Powers, and S. H Moseley. Thermal conductivity of Kapton tape. *Cryogenics*, 39(1):93–95, January 1999.

[95] Frank Pobell. *Matter and Methods at Low Temperatures*. Springer, Berlin ; New York, 3rd edition, February 2007.

[96] M. Sera, S. Kobayashi, M. Hiroi, N. Kobayashi, and S. Kunii. Thermal conductivity of RB_6 (R=Ce,Pr,Nd,Sm,Gd) single crystals. *Physical Review B*, 54(8):R5207–R5210, August 1996.

[97] National Instruments. LabVIEW Object-Oriented Programming: The Decisions Behind the Design - National Instruments, May 2014. Technical brochure.

[98] J. L. Hodeau, M. Marezio, J. P. Remeika, and C. H. Chen. Structural distortion in the primitive cubic phase of the superconducting/magnetic ternary rare-earth rhodium stannides. *Solid State Communications*, 42(2):97–102, April 1982.

[99] J. P. Remeika, G. P. Espinosa, A. S. Cooper, H. Barz, J. M. Rowell, D. B. McWhan, J. M. Vandenberg, D. E. Moncton, Z. Fisk, L. D. Woolf, H. C. Hamaker, M. B. Maple, G. Shirane, and W. Thomlinson. A new family of ternary intermetallic superconducting/magnetic stannides. *Solid State Communications*, 34(12):923–926, June 1980.

[100] G. P. Espinosa. Crystal growth and crystal-chemical investigation of systems containing new superconducting and/or magnetic ternary stannides. *Materials Research Bulletin*, 15(6):791–798, June 1980.

[101] A. S. Cooper. X-ray powder diffraction data for new superconducting/magnetic ternary intermetallic stannides. *Materials Research Bulletin*, 15(6):799–805, June 1980.

[102] Jinhu Yang, Bin Chen, Chishiro Michioka, and Kazuyoshi Yoshimura. Coexistence of Superconductivity and Ferromagnetic Spin-Fluctuation in $Ca_3Ir_4Sn_{13}$ Single Crystal. *Journal of the Physical Society of Japan*, 79(11):113705, November 2010.

[103] D. A. Tompsett. Electronic structure and phonon instabilities in the vicinity of the quantum phase transition and superconductivity of $(Sr,Ca)_3Ir_4Sn_{13}$. *Physical Review B*, 89(7):075117, February 2014.

[104] Wahyu Setyawan and Stefano Curtarolo. High-throughput electronic band structure calculations: challenges and tools. *Computational Materials Science*, 49(2):299–312, August 2010.

[105] S. Miraglia, J. L. Hodeau, M. Marezio, C. Laviron, M. Ghedira, and G. P. Espinosa. Nature of the structural distortion and of the chemical bonding in $SnM_3Rh_4Sn_{12}$ (M = La, Gd, Yb, Ca, Sr, and Th). *Journal of Solid State Chemistry*, 63(3):358–368, July 1986.

[106] P. Bordet, D. E. Cox, G. P. Espinosa, J. L. Hodeau, and M. Marezio. Synchrotron X-ray powder diffraction study of the phase I' compound: $SnLa_3Rh_4Sn_{12}$. *Solid State Communications*, 78(5):359–366, May 1991.

[107] Kefeng Wang and C. Petrovic. $Ca_3Ir_4Sn_{13}$: A weakly correlated nodeless superconductor. *Physical Review B*, 86(2):024522, July 2012.

[108] A. Ślebarski, J. Goraus, M. M. Maśka, P. Witas, M. Fijałkowski, C. T. Wolowiec, Y. Fang, and M. B. Maple. Effect of atomic disorder and Ce doping on superconductivity of $Ca_3Rh_4Sn_{13}$: Electric transport properties under high pressure. *Physical Review B*, 93(24):245126, June 2016.

[109] R. Sarkar, F. Brückner, M. Günther, Kefeng Wang, C. Petrovic, P. K. Biswas, H. Luetkens, E. Morenzoni, A. Amato, and H-H. Klauss. ^{119}Sn-NMR investigations on superconducting $Ca_3Ir_4Sn_{13}$: Evidence for multigap superconductivity. *Physica B: Condensed Matter*, 479:51–53, December 2015.

[110] A. R. Denton and N. W. Ashcroft. Vegard's law. *Physical Review A*, 43(6):3161–3164, March 1991.

[111] W. L. McMillan. Transition Temperature of Strong-Coupled Superconductors. *Physical Review*, 167(2):331–344, March 1968.

[112] P. K. Biswas, A. Amato, R. Khasanov, H. Luetkens, Kefeng Wang, C. Petrovic, R. M. Cook, M. R. Lees, and E. Morenzoni. Superconducting and magnetic properties of $Sr_3Ir_4Sn_{13}$. *Physical Review B*, 90(14):144505, October 2014.

[113] Y. W. Cheung, J. Z. Zhang, J. Y. Zhu, W. C. Yu, Y. J. Hu, D. G. Wang, Yuka Otomo, Kazuaki Iwasa, Koji Kaneko, Masaki Imai, Hibiki Kanagawa, Kazuyoshi Yoshimura, and Swee K. Goh. Second-order structural transition in the superconductor $La_3Co_4Sn_{13}$. *Physical Review B*, 93(24):241112, June 2016.

[114] L. M. Wang, Chih-Yi Wang, Guan-Min Chen, C. N. Kuo, and C. S. Lue. Weakly-correlated nodeless superconductivity in single crystals of $Ca_3Ir_4Sn_{13}$ and $Sr_3Ir_4Sn_{13}$ revealed by critical fields, Hall effect, and magnetoresistance measurements. *New Journal of Physics*, 17(3):033005, 2015.

[115] P. K. Biswas, Z. Guguchia, R. Khasanov, M. Chinotti, L. Li, Kefeng Wang, C. Petrovic, and E. Morenzoni. Strong enhancement of *s*-wave superconductivity near a quantum critical point of $Ca_3Ir_4Sn_{13}$. *Physical Review B*, 92(19):195122, November 2015.

[116] W. J. Ban, H. P. Wang, C. W. Tseng, C. N. Kuo, C. S. Lue, and N. L. Wang. Optical spectroscopy study of charge density wave order in $Sr_3Rh_4Sn_{13}$ and $(Sr_{0.5}Ca_{0.5})_3Rh_4Sn_{13}$. *Science China Physics, Mechanics and Astronomy*, 60(4):047011, April 2017.

[117] M. D. Johannes and I. I. Mazin. Fermi surface nesting and the origin of charge density waves in metals. *Physical Review B*, 77(16):165135, April 2008.

[118] X. Chen, S. K. Goh, D. A. Tompsett, W. C. Yu, L. Klintberg, S. Friedemann, H. E. Tan, J. Yang, B. Chen, M. Imai, K. Yoshimura, M. B. Gamza, F. M. Grosche, and M. L. Sutherland. Experimental determination of the Fermi surface of $Sr_3Ir_4Sn_{13}$. *Physical Review B*, 93(23):235121, June 2016.

[119] Karlheinz Schwarz and Peter Blaha. Solid state calculations using WIEN2k. *Computational Materials Science*, 28(2):259–273, October 2003.

[120] P. M. C. Rourke and S. R. Julian. Numerical extraction of de Haas-van Alphen frequencies from calculated band energies. *Computer Physics Communications*, 183(2):324–332, February 2012.

[121] C. N. Kuo, H. F. Liu, C. S. Lue, L. M. Wang, C. C. Chen, and Y. K. Kuo. Characteristics of the phase transition near 147 K in $Sr_3Ir_4Sn_{13}$. *Physical Review B*, 89(9):094520, March 2014.

[122] Neil W. Ashcroft and N. David Mermin. *Solid State Physics*. Holt, Rinehart and Winston, 1976.

[123] P. N. Trofimenkoff, J. P. Carbotte, and R. C. Dynes. Electron phonon mass renormalization. *Physics Letters A*, 27(6):394–395, August 1968.

[124] N. Kase, H. Hayamizu, and J. Akimitsu. Superconducting state in the ternary stannide superconductors $R_3T_4Sn_{13}$(R = La, Sr; T = Rh, Ir) with a quasiskutterudite structure. *Physical Review B*, 83(18):184509, May 2011.

[125] S. Tsuda, T. Yokoya, T. Kiss, Y. Takano, K. Togano, H. Kito, H. Ihara, and S. Shin. Evidence for a Multiple Superconducting Gap in MgB_2 from High-Resolution Photoemission Spectroscopy. *Physical Review Letters*, 87(17):177006, October 2001.

[126] G. S. Nolas, D. T. Morelli, and Terry M. Tritt. SKUTTERUDITES: A Phonon-Glass-Electron Crystal Approach to Advanced Thermoelectric Energy Conversion Applications. *Annual Review of Materials Science*, 29(1):89–116, 1999.

[127] D. M. Rowe. *Thermoelectrics Handbook: Macro to Nano*. CRC Press, December 2005.

[128] A. M. Strydom. Thermal and transport properties of the cubic semimetal $Y_3Ir_4Ge_{13}$: on the metallic border of thermoelectric merit. *Journal of Physics: Condensed Matter*, 19(38):386205, September 2007.

[129] Harold T. Stokes, Branton J. Campbell, and Dorian M. Hatch. ISODISTORT, June 2017.

[130] B. J. Campbell, H. T. Stokes, D. E. Tanner, and D. M. Hatch. ISODISPLACE: a web-based tool for exploring structural distortions. *Journal of Applied Crystallography*, 39(4):607–614, August 2006.

[131] R. A. Cowley. Structural phase transitions I. Landau theory. *Advances in Physics*, 29(1):1–110, February 1980.

[132] R. A. Cowley. Soft Modes and Structural Phase Transitions. *Integrated Ferroelectrics*, 133(1):109–117, January 2012.

[133] R. A. Cowley. Lattice Dynamics and Phase Transitions of Strontium Titanate. *Physical Review*, 134(4A):A981–A997, May 1964.

[134] $SrTiO_3$ crystal structure, lattice parameters. In O. Madelung, U. Rössler, and M. Schulz, editors, *Ternary Compounds, Organic Semiconductors*, pages 1–3. Springer Berlin Heidelberg, Berlin, Heidelberg, 2000.

[135] H. M. Rosenberg. *Low temperature solid state physics; some selected topics*. Clarendon Press, 1965.

[136] I. R. Walker and C. J. Moss. Spot welder for making small electrical contacts. *Review of Scientific Instruments*, 69(7):2747–2756, July 1998.

[137] K. Mendelssohn. Thermal conductivity of superconductors. *Physica*, 19(1):775–787, January 1953.

[138] Philip D. Thacher. Effect of Boundaries and Isotopes on the Thermal Conductivity of LiF. *Physical Review*, 156(3):975–988, April 1967.

[139] J. M. Ziman. *Principles of the Theory of Solids*. Cambridge University Press, Cambridge, 2nd edition, 1972.

[140] Hiroki Hayamizu, Naoki Kase, and Jun Akimitsu. Superconducting Properties of $Ca_3T_4Sn_{13}$(T = Co, Rh, and Ir). *Journal of the Physical Society of Japan*, 80(Suppl.A):SA114, January 2011.

[141] R. Berman, E. L. Foster, and J. M. Ziman. Thermal Conduction in Artificial Sapphire Crystals at Low Temperatures. I. Nearly Perfect Crystals. *Proceedings of the Royal Society of London A: Mathematical, Physical and Engineering Sciences*, 231(1184):130–144, July 1955.

[142] R. Berman, E. L. Foster, and J. M. Ziman. The Thermal Conductivity of Dielectric Crystals: The Effect of Isotopes. *Proceedings of the Royal Society of London A: Mathematical, Physical and Engineering Sciences*, 237(1210):344–354, November 1956.

[143] Jenifer N. Lomer and H. M. Rosenberg. The detection of dislocations by low temperature heat conductivity measurements. *Philosophical Magazine*, 4(40):467–483, April 1959.

[144] H. B. G. Casimir. Note on the conduction of heat in crystals. *Physica*, 5(6):495–500, June 1938.

[145] R. O. Pohl and B. Stritzker. Phonon scattering at crystal surfaces. *Physical Review B*, 25(6):3608–3614, March 1982.

[146] S. Y. Li, J.-B. Bonnemaison, A. Payeur, P. Fournier, C. H. Wang, X. H. Chen, and Louis Taillefer. Low-temperature phonon thermal conductivity of single-crystalline Nd_2CuO_4: Effects of sample size and surface roughness. *Physical Review B*, 77(13):134501, April 2008.

[147] P. C. Hohenberg and B. I. Halperin. Theory of dynamic critical phenomena. *Reviews of Modern Physics*, 49(3):435–479, July 1977.

[148] P. G. Klemens. The Thermal Conductivity of Dielectric Solids at Low Temperatures (Theoretical). *Proceedings of the Royal Society of London A: Mathematical, Physical and Engineering Sciences*, 208(1092):108–133, August 1951.

[149] J. Munevar, D. R. Sánchez, M. Alzamora, E. Baggio-Saitovitch, J. P. Carlo, T. Goko, A. A. Aczel, T. J. Williams, G. M. Luke, Hai-Hu Wen, Xiyu Zhu, Fei Han, and Y. J. Uemura. Static magnetic order of $Sr_4A_2O_6Fe_2As_2$ (A = Sc and V) revealed by Mössbauer and muon spin relaxation spectroscopies. *Physical Review B*, 84(2):024527, July 2011.

[150] Marianne Rotter, Michael Pangerl, Marcus Tegel, and Dirk Johrendt. Superconductivity and Crystal Structures of $(Ba_{1-x}K_x)Fe_2As_2$ (x=0-1). *Angewandte Chemie International Edition*, 47(41):7949–7952, September 2008.

[151] I. I. Mazin and J. Schmalian. Pairing symmetry and pairing state in ferropnictides: Theoretical overview. *Physica C: Superconductivity*, 469(9):614–627, May 2009.

[152] W. Z. Hu, J. Dong, G. Li, Z. Li, P. Zheng, G. F. Chen, J. L. Luo, and N. L. Wang. Origin of the Spin Density Wave Instability in AFe_2As_2 (A=Ba,Sr) as Revealed by Optical Spectroscopy. *Physical Review Letters*, 101(25):257005, December 2008.

[153] M. Yamashita, Y. Senshu, T. Shibauchi, S. Kasahara, K. Hashimoto, D. Watanabe, H. Ikeda, T. Terashima, I. Vekhter, A. B. Vorontsov, and Y. Matsuda. Nodal gap structure of superconducting $BaFe_2(As_{1-x}P_x)_2$ from angle-resolved thermal conductivity in a magnetic field. *Physical Review B*, 84(6):060507, August 2011.

[154] Fanlong Ning, Kanagasingham Ahilan, Takashi Imai, Athena S. Sefat, Ronying Jin, Michael A. McGuire, Brian C. Sales, and David Mandrus. ^{59}Co and ^{75}As NMR Investigation of Electron-Doped High T_c Superconductor $BaFe_{1.8}Co_{0.2}As_2$ (T_c=22 K). *Journal of the Physical Society of Japan*, 77(10):103705–103705, 2008.

[155] Clifford W. Hicks, Thomas M. Lippman, Martin E. Huber, Zhi-An Ren, Jie Yang, Zhong-Xian Zhao, and Kathryn A. Moler. Limits on the Superconducting Order Parameter in $NdFeAsO_{1-x}F_y$ from Scanning SQUID Microscopy. *Journal of the Physical Society of Japan*, 78(1):013708, December 2008.

[156] C.-T. Chen, C. C. Tsuei, M. B. Ketchen, Z.-A. Ren, and Z. X. Zhao. Integer and half-integer flux-quantum transitions in a niobium–iron pnictide loop. *Nature Physics*, 6(4):260–264, April 2010.

[157] Xiaohang Zhang, Yoon Seok Oh, Yong Liu, Liqin Yan, Kee Hoon Kim, Richard L. Greene, and Ichiro Takeuchi. Observation of the Josephson Effect in $Pb/Ba_{1-x}K_xFe_2As_2$ Single Crystal Junctions. *Physical Review Letters*, 102(14):147002, April 2009.

[158] M. A. Tanatar, J.-Ph. Reid, H. Shakeripour, X. G. Luo, N. Doiron-Leyraud, N. Ni, S. L. Bud'ko, P. C. Canfield, R. Prozorov, and Louis Taillefer. Doping Dependence of Heat Transport in the Iron-Arsenide Superconductor $Ba(Fe_{1-x}Co_x)_2As_2$: From Isotropic to a Strongly k-Dependent Gap Structure. *Physical Review Letters*, 104(6):067002, February 2010.

[159] J. K. Dong, S. Y. Zhou, T. Y. Guan, H. Zhang, Y. F. Dai, X. Qiu, X. F. Wang, Y. He, X. H. Chen, and S. Y. Li. Quantum Criticality and Nodal Superconductivity in the FeAs-Based Superconductor KFe_2As_2. *Physical Review Letters*, 104(8):087005, February 2010.

[160] K. Hashimoto, M. Yamashita, S. Kasahara, Y. Senshu, N. Nakata, S. Tonegawa, K. Ikada, A. Serafin, A. Carrington, T. Terashima, H. Ikeda, T. Shibauchi, and Y. Matsuda. Line nodes in the energy gap of superconducting $BaFe_2(As_{1-x}P_x)_2$ single crystals as seen via penetration depth and thermal conductivity. *Physical Review B*, 81(22):220501, June 2010.

[161] V. Mishra, G. R. Boyd, S. Graser, T. Maier, P. J. Hirschfeld, and D. J. Scalapino. Lifting of nodes by disorder in extended-s-state superconductors: Application to ferropnictides. *Physical Review B*, 79(9):094512, March 2009.

[162] Christian Platt, Gang Li, Mario Fink, Werner Hanke, and Ronny Thomale. Evolution of superconducting gap anisotropy in hole-doped 122 iron pnictides. *physica status solidi (b)*, 254(1), January 2017.

[163] F. F. Tafti, A. Juneau-Fecteau, M.-È Delage, S. René de Cotret, J.-Ph Reid, A. F. Wang, X.-G. Luo, X. H. Chen, N. Doiron-Leyraud, and Louis Taillefer. Sudden reversal in the pressure dependence of T_c in the iron-based superconductor KFe_2As_2. *Nature Physics*, 9(6):349–352, June 2013.

[164] F. F. Tafti, A. Ouellet, A. Juneau-Fecteau, S. Faucher, M. Lapointe-Major, N. Doiron-Leyraud, A. F. Wang, X.-G. Luo, X. H. Chen, and Louis Taillefer. Universal V-shaped temperature-pressure phase diagram in the iron-based superconductors KFe_2As_2, $RbFe_2As_2$, and $CsFe_2As_2$. *Physical Review B*, 91(5):054511, February 2015.

[165] Yasuyuki Nakajima, Renxiong Wang, Tristin Metz, Xiangfeng Wang, Limin Wang, Hyunchae Cynn, Samuel T. Weir, Jason R. Jeffries, and Johnpierre Paglione. High-temperature superconductivity stabilized by electron-hole interband coupling in collapsed tetragonal phase of KFe_2As_2 under high pressure. *Physical Review B*, 91(6):060508, February 2015.

[166] Bosen Wang, Kazuyuki Matsubayashi, Jinguang Cheng, Taichi Terashima, Kunihiro Kihou, Shigeyuki Ishida, Chul-Ho Lee, Akira Iyo, Hiroshi Eisaki, and Yoshiya Uwatoko. Absence of superconductivity in the collapsed tetragonal phase of KFe_2As_2 under hydrostatic pressure. *Physical Review B*, 94(2):020502, July 2016.

[167] Jian-Jun Ying, Ling-Yun Tang, Viktor V. Struzhkin, Ho-Kwang Mao, Alexander G. Gavriliuk, Ai-Feng Wang, Xian-Hui Chen, and Xiao-Jia Chen. Tripling the critical temperature of KFe_2As_2 by carrier switch. *arXiv:1501.00330 [cond-mat]*, January 2015.

[168] Valentin Taufour, Neda Foroozani, Makariy A. Tanatar, Jinhyuk Lim, Udhara Kaluarachchi, Stella K. Kim, Yong Liu, Thomas A. Lograsso, Vladimir G. Kogan, Ruslan Prozorov, Sergey L. Bud'ko, James S. Schilling, and Paul C. Canfield. Upper critical field of KFe_2As_2 under pressure: A test for the change in the superconducting gap structure. *Physical Review B*, 89(22):220509, June 2014.

[169] Daniel Guterding, Steffen Backes, Harald O. Jeschke, and Roser Valentí. Origin of the superconducting state in the collapsed tetragonal phase of KFe_2As_2. *Physical Review B*, 91(14):140503, April 2015.

[170] Roald Hoffmann and Chong Zheng. Making and breaking bonds in the solid state: the thorium chromium silicide ($ThCr_2Si_2$) structure. *The Journal of Physical Chemistry*, 89(20):4175–4181, September 1985.

[171] Alaska Subedi. Unconventional sign-changing superconductivity near quantum criticality in YFe_2Ge_2. *Physical Review B*, 89(2):024504, January 2014.

[172] David J. Singh. Superconductivity and magnetism in YFe_2Ge_2. *Physical Review B*, 89(2):024505, January 2014.

[173] Y. Zou, Z. Feng, P. W. Logg, J. Chen, G. Lampronti, and F. M. Grosche. Fermi liquid breakdown and evidence for superconductivity in YFe_2Ge_2. *physica status solidi (RRL) – Rapid Research Letters*, 8(11):928–930, November 2014.

[174] G. R. Stewart. Non-Fermi-liquid behavior in d- and f-electron metals. *Reviews of Modern Physics*, 73(4):797–855, October 2001.

[175] Sheng Ran, Sergey L. Bud'ko, and Paul C. Canfield. Effects of substitution on low-temperature physical properties of $LuFe_2Ge_2$. *Philosophical Magazine*, 91(34):4388–4400, December 2011.

[176] N. Sirica, F. Bondino, S. Nappini, I. Píš, L. Poudel, A. D. Christianson, D. Mandrus, D. J. Singh, and N. Mannella. Spectroscopic evidence for strong quantum spin fluctuations with itinerant character in YFe_2Ge_2. *Physical Review B*, 91(12):121102, March 2015.

[177] Paolo Vilmercati, Alexei Fedorov, Federica Bondino, Francesco Offi, Giancarlo Panaccione, Paolo Lacovig, Laura Simonelli, Michael A. McGuire, Athena S. M. Sefat, David Mandrus, Brian C. Sales, Takeshi Egami, Wei Ku, and Norman Mannella. Itinerant electrons, local moments, and magnetic correlations in the pnictide superconductors $CeFeAsO_{1-x}F_x$ and $Sr(Fe_{1-x}Co_x)_2As_2$. *Physical Review B*, 85(22):220503, June 2012.

[178] H. Gretarsson, A. Lupascu, Jungho Kim, D. Casa, T. Gog, W. Wu, S. R. Julian, Z. J. Xu, J. S. Wen, G. D. Gu, R. H. Yuan, Z. G. Chen, N.-L. Wang, S. Khim, K. H. Kim, M. Ishikado, I. Jarrige, S. Shamoto, J.-H. Chu, I. R. Fisher, and Young-June Kim. Revealing the dual nature of magnetism in iron pnictides and iron chalcogenides using x-ray emission spectroscopy. *Physical Review B*, 84(10):100509, September 2011.

[179] Daniel Guterding, Harald O. Jeschke, I. I. Mazin, J. K. Glasbrenner, E. Bascones, and Roser Valentí. Nontrivial Role of Interlayer Cation States in Iron-Based Superconductors. *Physical Review Letters*, 118(1):017204, January 2017.

[180] I. I. Mazin, M. D. Johannes, L. Boeri, K. Koepernik, and D. J. Singh. Problems with reconciling density functional theory calculations with experiment in ferropnictides. *Physical Review B*, 78(8):085104, August 2008.

[181] H. Kim, S. Ran, E. D. Mun, H. Hodovanets, M. A. Tanatar, R. Prozorov, S. L. Bud'ko, and P. C. Canfield. Crystal growth and annealing study of fragile, non-bulk superconductivity in YFe_2Ge_2. *Philosophical Magazine*, 95(7):804–818, March 2015.

[182] Michael Tinkham. *Introduction to Superconductivity: Second Edition*. Dover Publications, June 2004.

[183] M. A. Avila, S. L. Bud'ko, and P. C. Canfield. Anisotropic magnetization, specific heat and resistivity of RFe_2Ge_2 single crystals. *Journal of Magnetism and Magnetic Materials*, 270(1–2):51–76, March 2004.

[184] W. H. Toews and R. W. Hill. A robust and well shielded thermal conductivity device for low temperature measurements. *Review of Scientific Instruments*, 85(4):043905, April 2014.

[185] J. O. Willis and D. M. Ginsberg. Thermal conductivity of superconducting alloy films in a perpendicular magnetic field. *Physical Review B*, 14(5):1916–1926, September 1976.

[186] Bernhard Mühlschlegel. Die thermodynamischen Funktionen des Supraleiters. *Zeitschrift für Physik*, 155(3):313–327, June 1959.

[187] L.S. Borkowski, P.J. Hirschfeld, and W.O. Putikka. Transport properties of extended-*s*-state superconductors. *Physical Review B*, 52(6):R3856–R3859, August 1995.

[188] N. F. Mott. Rare-earth compounds with mixed valencies. *Philosophical Magazine*, 30(2):403–416, August 1974.

[189] A. Menth, E. Buehler, and T. H. Geballe. Magnetic and Semiconducting Properties of SmB_6. *Physical Review Letters*, 22(7):295–297, February 1969.

[190] J. W. Allen, B. Batlogg, and P. Wachter. Large low-temperature Hall effect and resistivity in mixed-valent SmB_6. *Physical Review B*, 20(12):4807–4813, December 1979.

[191] J. C. Cooley, M. C. Aronson, Z. Fisk, and P. C. Canfield. SmB_6: Kondo Insulator or Exotic Metal? *Physical Review Letters*, 74(9):1629–1632, February 1995.

[192] Maxim Dzero, Kai Sun, Victor Galitski, and Piers Coleman. Topological Kondo Insulators. *Physical Review Letters*, 104(10):106408, March 2010.

[193] Tetsuya Takimoto. SmB_6: A Promising Candidate for a Topological Insulator. *Journal of the Physical Society of Japan*, 80(12):123710, November 2011.

[194] Steven Wolgast, Çağlıyan Kurdak, Kai Sun, J. W. Allen, Dae-Jeong Kim, and Zachary Fisk. Low-temperature surface conduction in the Kondo insulator SmB_6. *Physical Review B*, 88(18):180405, November 2013.

[195] D. J. Kim, S. Thomas, T. Grant, J. Botimer, Z. Fisk, and Jing Xia. Surface Hall Effect and Nonlocal Transport in SmB_6: Evidence for Surface Conduction. *Scientific Reports*, 3, November 2013.

[196] B. S. Tan, Y.-T. Hsu, B. Zeng, M. Ciomaga Hatnean, N. Harrison, Z. Zhu, M. Hartstein, M. Kiourlappou, A. Srivastava, M. D. Johannes, T. P. Murphy, J.-H. Park, L. Balicas, G. G. Lonzarich, G. Balakrishnan, and Suchitra E. Sebastian. Unconventional Fermi surface in an insulating state. *Science*, 349(6245):287–290, July 2015.

[197] G. Li, Z. Xiang, F. Yu, T. Asaba, B. Lawson, P. Cai, C. Tinsman, A. Berkley, S. Wolgast, Y. S. Eo, Dae-Jeong Kim, C. Kurdak, J. W. Allen, K. Sun, X. H. Chen, Y. Y. Wang, Z. Fisk, and Lu Li. Two-dimensional Fermi surfaces in Kondo insulator SmB_6. *Science*, 346(6214):1208–1212, December 2014.

[198] Johannes Knolle and Nigel R. Cooper. Quantum Oscillations without a Fermi Surface and the Anomalous de Haas-van Alphen Effect. *Physical Review Letters*, 115(14):146401, September 2015.

[199] Onur Erten, Po-Yao Chang, Piers Coleman, and Alexei M. Tsvelik. Skyrme Insulators: Insulators at the Brink of Superconductivity. *Physical Review Letters*, 119(5):057603, August 2017.

[200] Mate Hartstein, William Toews, Yu Te Hsu, Bin Zeng, Xiaoye Chen, Monica Ciomaga Hatnean, Qiu Run Zhang, Shota Nakamura, Andrew Padgett, Gilles Rodway-Gant, Joel Berk, Matthew Kingston, Grace Zhang, Mun Chan, Satoshi Yamashita, Toshiro Sakakibara, Yasumasa Takano, Ju-Hyun Park, Luis Balicas, Neil Harrison, Natalya Shitsevalova, Geetha Balakrishnan, Gilbert G. Lonzarich, Robert Hill, Michael L Sutherland, and Suchitra Sebastian. New route to a Fermi surface in the absence of a Fermi liquid: a Kondo insulator near the insulator-metal transition. *Nature Physics (accepted for publication)*, 2017.